

Epitaxial Ge-Te-Sb Thin Films by Pulsed Laser Deposition

Von der Fakultät für Physik und Geowissenschaften
der Universität Leipzig

genehmigte

DISSERTATION

zur Erlangung des akademischen Grades

Doctor Rerum Naturalium

Dr. rer. nat.

vorgelegt

von M. Sc. Erik Thelander

geboren am 17.06.1983 in Österhaninge/Schweden

Gutachter: Prof. Dr. Dr. h.c. Bernd Rauschenbach (Leipzig)

Prof. Dr. Hans-Ulrich Krebs (Göttingen)

Tag der Verleihung: 31.03.2015

Bibliographische Beschreibung

Thelander, Erik

Epitaxial Ge-Te-Sb Thin Films by Pulsed Laser Deposition

Universität Leipzig, Dissertation

113 S., 127 Lit., 76 Abb., 8 Tab.

Referat:

This thesis deals with the synthesis and characterization of Ge-Te-Sb (GST) thin films. The films were deposited using a Pulsed Laser Deposition (PLD) method and mainly characterized with XRD, SEM, AFM and TEM.

For amorphous and polycrystalline films, un-etched Si(100) was used. The amorphous films showed a similar crystallization behavior as films deposited with sputtering and evaporation techniques.

When depositing GST on un-etched Si(100) substrates at elevated substrate temperatures (130-240°C), polycrystalline but highly textured films were obtained. The preferred growth orientation was either GST(111) or GST(0001) depending on if the films were cubic or hexagonal.

Epitaxial films were prepared on crystalline substrates. On KCl(100), a mixed growth of hexagonal GST(0001) and cubic GST(100) was observed. The hexagonal phase dominates at low temperatures whereas the cubic phase dominates at high temperatures. The cubic phase is accompanied with a presumed GST(221) orientation when the film thickness exceeds ~70 nm. Epitaxial films were obtained with deposition rates as high as 250 nm/min.

On BaF₂(111), only (0001) oriented epitaxial hexagonal GST films are found, independent of substrate temperature, frequency or deposition background pressure. At high substrate temperatures there is a loss of Ge and Te which shifts the crystalline phase from Ge₂Sb₂Te₅ towards GeSb₂Te₄. GST films deposited at room temperature on BaF₂(111) were in an amorphous state, but after exposure to an annealing treatment they crystallize in an epitaxial cubic structure.

Film deposition on pre-cleaned and buffered ammonium fluoride etched Si(111) show growth of epitaxial hexagonal GST, similar to that of the deposition on BaF₂(111). When the Si-substrates were heated directly to the deposition temperature films of high crystalline quality were obtained. An additional heat treatment of the Si-substrates prior to deposition deteriorated the crystal quality severely.

The gained results show that PLD can be used as a method in order to obtain high quality epitaxial Ge-Sb-Te films from a compound target and using high deposition rates.

— If you want to understand function, study structure —

Francis Crick

Table of Contents

Chapter 1	Introduction	1
Chapter 2	Basics	3
2.1.	Phase change materials	3
2.1.1.	Amorphous-crystalline transition	3
2.2.	The ternary Ge-Sb-Te system and crystal structures thereof	5
2.2.1.	Crystal structures of GeTe and Sb ₂ Te ₃	6
2.2.2.	Crystal structures of Ge ₂ Sb ₂ Te ₅	8
2.2.3.	Crystal structures of Ge ₁ Sb ₂ Te ₄	10
2.2.4.	Crystallographic data from Ge-Sb-Te compounds	11
Chapter 3	Experimental methods & materials	15
3.1.	Pulsed laser deposition	15
3.1.1.	Working principle and setup	15
3.2.	Sample preparation and treatment	17
3.2.1.	Substrate materials and preparation	17
3.2.2.	Substrate heat treatment prior to deposition	18
3.2.3.	Substrate temperature calibration	18
3.2.4.	Heat treatment of as-deposited films	19
3.3.	Characterization methods	19
3.3.1.	X-ray based methods	19
	<i>X-ray diffraction</i>	19
	<i>In-plane x-ray diffraction</i>	21
	<i>Texture goniometry (in-plane pole figure measurements)</i>	23
	<i>X-ray reflectivity</i>	24
3.3.2.	Imaging techniques including spectroscopy	25
	<i>Scanning electron microscopy</i>	25
	<i>Transmission electron microscopy</i>	25
	<i>Energy dispersive x-ray spectroscopy</i>	26
	<i>Atomic force microscopy</i>	28
Chapter 4	Results & discussion	29
4.1.	Growth of polycrystalline GST films	29
4.1.1.	Initial growth investigations of pulsed laser deposited GST	29
4.1.2.	Polycrystalline film growth of GST at elevated substrate temperatures	37
4.1.3.	Summary of the results on the deposition of polycrystalline and amorphous GST	40
4.2.	Epitaxial growth of GST on KCl(100)	43
4.2.1.	The effect of substrate temperature on the growth of GST on KCl(100)	43
4.2.2.	The effect of deposition rate on the growth of GST on KCl(100)	50
4.2.3.	The effect of film thickness on the crystallite orientation	54
4.2.4.	Summary of the results on the deposition of GST on KCl(100)	59
4.3.	Epitaxial growth of GST on BaF₂(111)	61
4.3.1.	The effect of substrate temperature on the growth of GST on BaF ₂ (111)	61
4.3.2.	The effects of deposition rate and pressure on the growth of GST on BaF ₂ (111)	70

4.3.3.	Hints of cubic GST	73
4.3.4.	Summary of the results on the deposition of GST on BaF ₂ (111)	78
4.4.	Epitaxial growth of GST on Si(111)	79
4.4.1.	The growth of GST on non-thermally pre-treated Si(111)	79
4.4.2.	The growth of GST on thermally pre-treated Si(111)	87
4.4.3.	Summary of the results on the deposition of GST films on Si(111)	90
Chapter 5	Summary and outlook	93
Bibliography		97
Acknowledgements		105
Curriculum Vitae		107
List of publications		109
Selbstständigkeitserklärung		113

Chapter 1

Introduction

Chalcogenide materials containing Te reveal a unique set of properties that cannot be matched by other chalcogenide compounds, i.e. selenides, sulfides and oxides. For instance the tellurides can be superconducting^[1,2], ferromagnetic^[3], ferroelectric^[4], thermoelectric^[5,6] or they can possess topological insulator characteristics^[7], properties that are all related to the electronic structure of these compound materials^[8,9]. Additionally, several Te alloy compositions belong to the group of phase change materials. This special group of materials can show distinct and drastic differences in optical and electronic properties just by changing the actual structural state they are in, i.e. amorphous or crystalline. This is quite remarkable and not at all common for most substances. Consider for instance SiO₂, which is fully transparent and a good insulator both in the amorphous and the crystalline state or a metal which is highly conducting and reflects light independent of the actual structural state it is in. This unique behavior of phase change materials has led to extensive investigations over the last decades in the quest for new technologies. In fact, these materials are present everywhere in the form of re-writable optical media, but nowadays they are also being considered as candidates for electronic memory devices^[10]. Very recently, also optoelectronic devices^[11] based on phase-change material were developed, which show that this field is in constant progress.

The research field of phase change materials was originally discovered by Stanford R. Ovshinsky in 1968^[12], when he noticed that these materials could be rapidly switched between a highly resistive and a more conductive state by applying an electric field. He recognized the potential in this technology for constructing semiconductor switching devices based on a physical phase change, but at the time also the complementary metal-oxide-semiconductor technology was developing rapidly and they offered switching devices with lower power consumption and higher speed. Therefore, phase change technology for electronic memory devices did not take on for some more decades. In the 1990s, re-writable optical media were introduced on the market by Matsushita (Panasonic Corporation) and this was the first commercial phase change technology products. Since then the number of re-writeable products has virtually exploded and nowadays storage capacities of 100 Gb are achieved on a single disc^[13]. The underlying technology behind the rewritable optical storage is based on the large optical contrast between the amorphous and crystalline state.

Currently, the possibility to use phase change materials as electronic memory devices, i.e. a phase change memory (PCM), is once more being investigated^[14-18] and it is believed that the PCMs can be a competitive replacement for current non-volatile memory technologies, i.e. Flash memories. The materials being used are often alloys based on Ge-Sb-Te (GST) and one of the most investigated materials is the Ge₂Sb₂Te₅ phase. Nowadays,

PCMs have entered the market^[19], but it is still somewhat of a niche product due to the still too high power consumption. In 2011, however, it was shown that an ordered fiber-textured crystalline state could drastically improve the performance and stability of a PCM-cell^[20]. This led to the development of even higher ordered Ge-Sb-Te-films in the form of epitaxial layers^[21-24] and, furthermore, it has been shown that an epitaxial recrystallization of a laser beam-amorphized epitaxial Ge₂Sb₂Te₃ film is possible^[25]. This proves that epitaxial layers could also be promising from a technological point of view while at the same time giving insight to structural properties. Until now, all epitaxial growth of phase change materials has been performed with Molecular Beam Epitaxy (MBE) using elemental fluxes on lattice matched semiconductor substrates. While MBE is capable of producing films with high structural quality, it poses some severe limitations in terms of process complexity (multiple evaporation sources) and low deposition rate (~0.3 nm/min) that effectively hamper any potential industrial application. Another deposition method, often used for epitaxial growth is Pulsed Laser Deposition (PLD). PLD compared to MBE employs a compound target and much higher deposition rates (1-250 nm/min for PLD compared with ~0.3 nm/min for MBE), but before this work was initiated it had only been applied for the production of amorphous or polycrystalline GST films^[26-29].

Therefore, the overall aim of this thesis was to investigate the epitaxial growth of thin films of GST using PLD. However, this investigation was not only limited to epitaxial films and more specifically, the aims can be formulated as follows:

- To establish a deposition process for amorphous, polycrystalline and epitaxial GST films by PLD.
- To identify the typical crystallization temperature range of PLD-deposited amorphous GST films as by thermal annealing.
- To investigate the growth of GST at elevated substrate temperature using non-crystalline substrate surface in order to determine any texturing effects.
- To investigate the growth of GST at elevated substrate temperature using crystalline substrate surfaces in order to obtain epitaxial films.
- Structural characterization of the produced films with mainly x-ray diffraction and transmission electron microscopy.

Scope

Throughout the thesis, different deposition parameters were varied and the results are presented and discussed in **Chapter 4**. In **section 4.1** the results on the deposition of amorphous and polycrystalline GST films are presented. **Section 4.2** deals with the deposition of GST on freshly cleaved KCl(100) substrates. In **section 4.3** the deposition of GST on freshly cleaved BaF₂(111) substrates is described. Finally, **section 4.4** is devoted to the deposition of GST on Si(111) substrates.

Chapter 2

Basics

2.1. Phase change materials

The whole field of phase change materials research started in the late nineteen sixties, when Stanford R. Ovshinsky published an article about a peculiar I-V behavior in amorphous chalcogenide glasses^[12]. Below a certain threshold voltage U_H the film was in a highly resistive state with ohmic behavior. Above U_H , the resistivity dropped orders of magnitude and the I-V response in the film was not ohmic anymore. In this state the current could be varied largely without affecting the voltage drop across the device. By reducing the current below a certain value the material switched back to the high resistance state once more. Also, by varying the composition in his films he could see a permanent switching effect, i.e. the films remained in the highly conductive state even at zero voltage across the device. Ovshinsky recognized the potential with the switching behavior to be used as a semiconducting switching device and patented the technology^[30]. However, at this time the complementary metal oxide semiconductor technology was in rapid development and they could produce far more efficient switching/selecting devices. Therefore, phase change based devices never pushed through as a major technology. Nevertheless, the same research group continued to investigate these Te-containing films and a few years later they could show that thin films of these materials can undergo a rapid crystallization when illuminated with a short laser pulse^[30]. The rapid crystallization was accompanied by a distinct reflectivity increase for the laser irradiated spots. In spite of this interesting finding it would take another ~ 20 years before Yamada could show that Ge-Sb-Te alloys could be used effectively in re-writable optical data storage media^[31]. Since then the number of re-writable (RW) storage media is ever increasing (CD-RW, DVD-RW, Blu-Ray-RW) and the development still goes on. Nowadays, phase change materials are once more considered as potential Phase Change Memories (PCM) and that is where much of the research focus lies today^[10].

2.1.1. Amorphous-crystalline transition

Phase change technology (optical RW or PCM) is based upon large differences in physical properties (optical or electronic) between a crystalline and an amorphous state of the material. Independent of the memory technology (optical or electronic) the phase change material needs to be repeatedly switched between the amorphous and crystalline phase. The switching is accomplished by a short (10-50 ns) energy input, in form of either a laser or a current pulse. This idea is exemplified in Figure 2-1. Starting from a crystalline material, a high intensity pulse is applied in a localized region of the material (Figure 2-1a). This pulse can be of either electronic or optical origin, as already mentioned. The high applied

intensity rapidly increases the temperature in the material and brings it above the melting point T_m . Due to the short pulse duration and the localized heat input, the melted material is subsequently quenched into the amorphous phase after the pulse is over. The amorphous state is characterized by a low optical reflectivity and a high electrical resistance. These properties can be read out by an appropriate pulse of low intensity and thus, information can be coded in form of bits in the material. In Figure 2-1b, the disorder in the material is plotted as a function of temperature for different heat treatment pathways. The amorphization pathway is indicated by the red curve. Below the glass transition temperature T_g the viscosity η in the material is so high (a practical used limit as suggested by Kittel^[32]: $\eta > 10^{12}$ Pa·s) that the atoms basically freeze in. Upon an applied pulse of intermediate intensity and longer duration (Figure 2-1c) the temperature in the localized spot is raised above the crystallization temperature T_c , which in general resides somewhere between T_g and T_m . The film material then crystallizes and a high reflectivity or low resistance is obtained. This pathway is indicated with the blue curve in Figure 2-1b. The atomic ordering in the material in each respective phase (state) is depicted within each gray circle in Figure 2-1a-c. The crystalline state is characterized by a regular arrangement of the atoms as expected, and the liquid state is in general characterized by complete disorder (exception GeTe, see Ref. 33). In the amorphous state phase change materials exhibit a lack of long range order, but local ordering is still present. This is mainly seen in the Ge-Te and Sb-Te bond length distribution for Ge-Sb-Te compounds which gets shorter in the amorphous phase as evidenced by Kolobov et al.^[34]. According to the authors this implies a (at least partial) tetrahedral arrangement of the Ge atoms in the amorphous phase. However, the actual atomic environment in the amorphous phase is still a matter of debate, since Huang and Robertson argues that the Ge atoms in the amorphous state are still octahedral coordinated^[35]. A plausible idea is that the answer lies somewhere in between as suggested by Lencer et al^[36]. Independent of the actual atomic environment in the amorphous phase, all models agree upon that the bonding character is of covalent nature, with Ge, Sb and Te almost fulfilling the 8-N rule, where N is the number of valence electrons. The crystalline state (metastable) is better understood though, and all Ge-

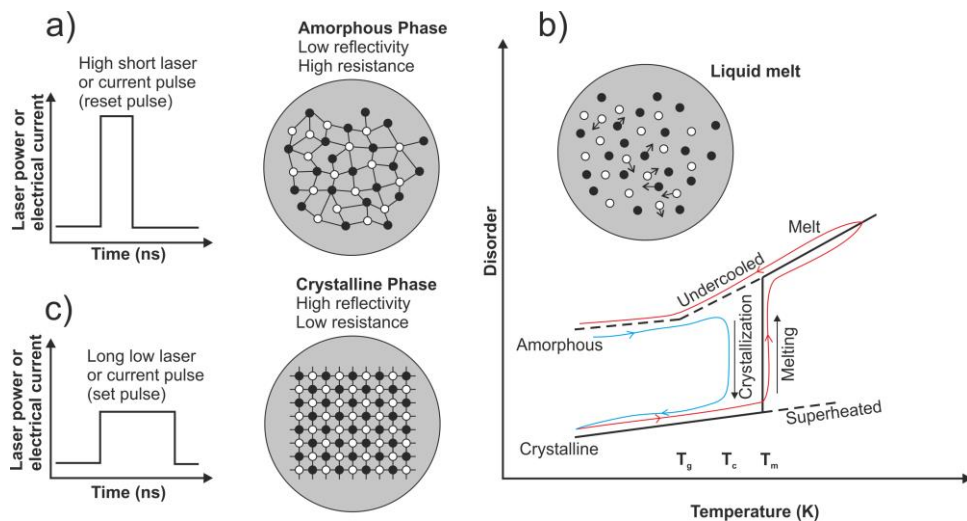


Figure 2-1. Function of phase change memory technology. Image idea adapted from Ref. 37

Sb-Te compounds crystallize within an octahedral environment (more details on crystal structures in section 2.2). This six fold-coordination leads to a so-called resonance bonding, since the number of valence electrons is not enough to fulfil a covalent bond. Instead, the electrons are delocalized over the participating bonds. This concept is nowadays well established with phase change materials^[8,38,39] and can explain why the optical and electrical properties can differ so much between the amorphous and the crystalline state. This is due to the fact that the resonance bonds are highly polarizable and hence, react strongly to an external electromagnetic wave.

Although the crystalline-amorphous transition was described above as involving melting, there are some indications of non-thermally induced amorphization of Te-based alloys^[34,40], i.e. an electric field induced amorphization. This is especially obvious in the paper from Simpson et al^[20], who designed a so-called interfacial phase change memory. This multilayer memory structure was built up of layers of GeTe and Sb₂Te₃ in a way highly resembling the hexagonal equilibrium structure of GST compounds (see section 2.2.2 and 2.2.3). The authors could show a dramatic improvement in switching characteristics, i.e. lower power consumption and longer life time for this type of films compared to classical homogenous GST films. They inferred the improved performance to the local environment of the Ge atoms which could move from an octahedral environment (resonance bonding) to a less coordinated site (covalent bonding) in the film structure. This showed in a remarkable way that ordered phase change films could be of great future research interest.

2.2. The ternary Ge-Sb-Te system and crystal structures thereof

The materials involved in the above mentioned technology are in general based upon combinations of Ge-Sb-Te^[13]. In most cases the phase change material contains Te, giving the impression that the material needs to contain a chalcogenide. However, alloys based upon sulfides and selenides do not show the sought-after phase change effect. Additionally, also chalcogenide free films show a phase change behavior, for instance Ge₁₅Sb₈₅^[41] or GaSb^[42]. Nevertheless, the ternary Ge-Sb-Te material system has been the most investigated one in the field of phase change material and will probably continue to fascinate and challenge researchers for a long time. This is due to a good balance of the important phase change properties like fast crystallization speed, high crystallization temperature and high optical and electrical contrast. All the above mentioned properties can seldom be fulfilled with one composition, but good enough properties can often be found with a certain composition. Since this material system seems to be of such importance, it is worth inspecting it in more detail. In Figure 2-2, a ternary phase diagram of Ge, Sb and Te is depicted. The black solid line is the tie line between GeTe and Sb₂Te₃, and the black squares indicate some more common intermetallic phases in the system. It should be noted that, supposedly[†], already in the nineteen sixties, Abrikosov et al.^[43] and Petrov et

Phase change materials

[†] Due to difficulties in obtaining translated as well as original versions, the author has not read the actual articles. However, as first investigators they still deserve to be mentioned.

al.^[44] investigated this material system. However, it was only with the discovery by Yamada et al.^[31], that the material system got investigated systematically with respect to technological function^[45]. A very detailed structural investigation of the ternary system was furthermore conducted by Kosyakov et al.^[46]. The intermetallic compounds on the tie line are formed by combining stoichiometric amounts of GeTe and Sb₂Te₃, i.e. (GeTe)_m(Sb₂Te₃)_n forms a compound Ge_mSb_nTe_{m+n}. In that way, the ratio between the two binary compounds can be varied to obtain different properties^[31]. For instance, the crystallization temperature increases towards GeTe (important for data retention), but the crystallization time decreases towards Sb₂Te₃ (important for high speed operation). In this way the phase change properties can be tuned. Interestingly, all material compositions on the tie line show an average p-electron number per lattice site N_p of 3 according to the following relationship^[36]:

$$N_p = \frac{2n_{Ge} + 3n_{Sb} + 4n_{Te}}{n_{Ge} + n_{Sb} + n_{Te} + n_V} \quad (1)$$

Where n_i is the atomic concentration of species i , and $n_V = n_{Te} - (n_{Ge} + n_{Sb})$. Assuming an octahedral coordination for the involved atoms (see section 2.2.1), a value of $N_p=6$ would be expected for a covalent bond type. This strengthens the idea of resonance bonding (see section 2.1.1) being an important pre-requisite for phase change materials.

2.2.1. Crystal structures of GeTe and Sb₂Te₃

The binary compound GeTe crystallizes in a rhombohedral structure (space group: R3m) with a lattice parameter $a=0.4281$ nm and a rhombohedral angle of 58.358° (rhombohedral setting) with atomic positions at Ge(0,0,0) and Te(0.521,0.521,0.521)^[47]. Alternatively,

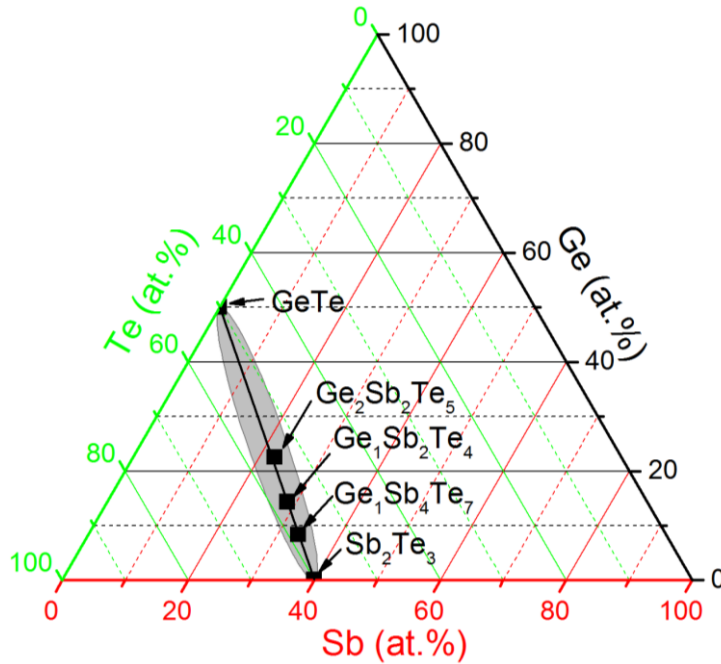


Figure 2-2. Ternary phase diagram of the Ge-Sb-Te system. Different GeSbTe compositions lying on the GeTe-Sb₂Te₃ tie line are presented.

the unit cell can be displayed using a hexagonal lattice, i.e. $a=0.417$ nm and $c=1.061$ nm. This structure can be interpreted as a distorted cubic rock salt structure^[48] with an angle of $\sim 88.3^\circ$ deviating from the perfect 90° as depicted in Figure 2-3a, where the purple box outlines a distorted rock salt structure. The distortion angle gradually becomes weakened by increasing the temperature, and above $\sim 420^\circ\text{C}$ the structure is that of perfect cubic rock salt^[49]. The distortion of GeTe is known as a Peierls distortion along the (pseudo-)cubic $[111]$ direction, and is known for elements and compounds with distinct p-type bond character^[50]. The aligned p-orbitals are unstable against a periodic oscillation leading to alternating long and short bonds in the crystal^[36,51]. Also in Figure 2-3a, the hexagonal unit cell is outlined in red and the hexagonal basal plane projection is depicted next to it.

The second binary compound Sb_2Te_3 crystallizes in a hexagonal unit cell with lattice parameters ranging from 0.426-0.427 nm and 2.988-3.045 nm for a and c , respectively^[52,53]. In Figure 2-3b, the crystal structure is presented. By a closer inspection, the hexagonal unit cell is strongly related to a distorted cubic structure. This is indicated by the octahedrons which show the local coordination of Sb (red) and Te (blue). However, since there is a 50% excess of Te in the structure, the octahedrons cannot form a continuous network, but are interrupted by Te-Te layers (black horizontal arrows). These Te-Te layers are held together by Van der Waals interactions. The Van der Waals gap show a separation which can be explained by a repulsive Te-Te contribution and can be thought of as intrinsic vacancy layers (VL). The spacing S of each VL is increased when the Te atomic concentration is reduced according to $S = 2m + 3$, in a compound of composition $\text{Sb}_{2m}\text{Te}_3$. By viewing the hexagonal projections in Figure 2-3a,b, it is clear to see why there exist so

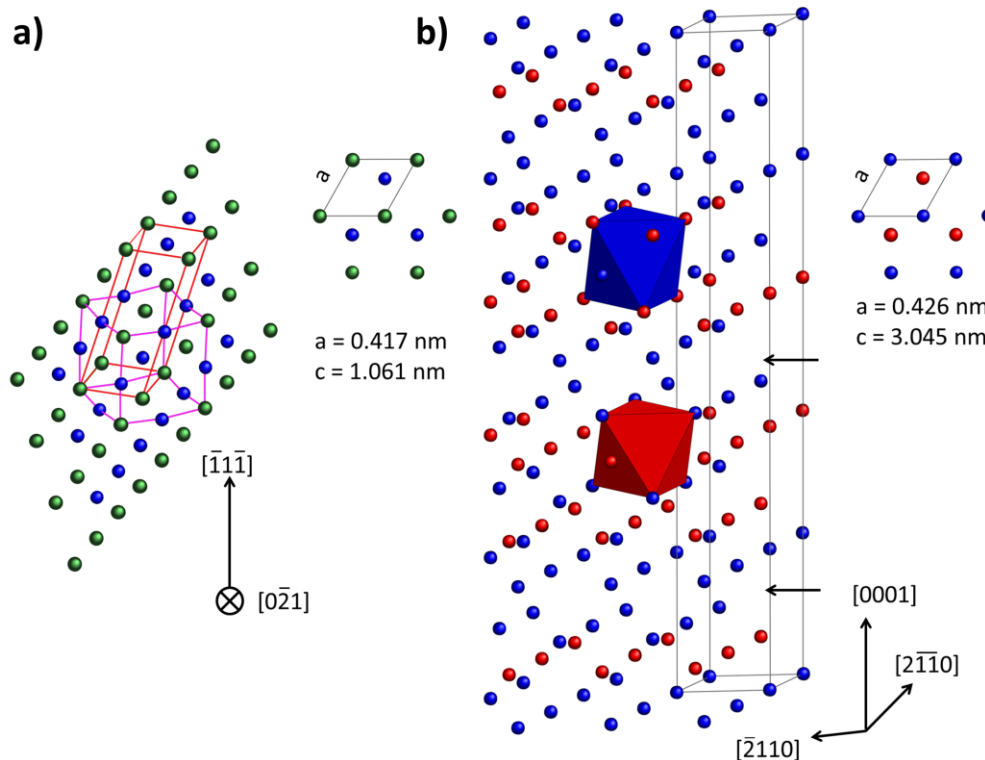


Figure 2-3. Crystal structure of GeTe (a) and Sb_2Te_3 (b) and the corresponding hexagonal basal plane projection. The green, red and blue spheres symbolize Ge, Sb and Te atoms, respectively.

many intermetallic stoichiometric compounds in this material system. The hexagonal basal plane lattice parameter does not differ much between the two crystals explaining the good miscibility throughout the whole GeTe-Sb₂Te₃ system.

2.2.2. Crystal structures of Ge₂Sb₂Te₅

Ge₂Sb₂Te₅ is the equivalence of (GeTe)₂(Sb₂Te₃) and resides in the middle of the tie line in Figure 2-2. From here on, this composition will be referred to as GST225 for simplicity. The structural ordering of this compound has been studied quite extensively for the amorphous and crystalline states, but this section will deal solely with the crystalline structures. For more information about ordering in the amorphous state, the reader is referred to Refs. 54 and 55. The crystalline structures of GST225 comprise the metastable cubic phase and the thermodynamically stable hexagonal phase. The metastable cubic phase is generally thought to exhibit the sought-after phase change properties, but it has been shown that switching between the amorphous and hexagonal phase with optical pulses works just as well^[56]. The metastable cubic phase normally forms at annealing temperatures above 150°C^[57] or by means of short pulse laser irradiation. In Figure 2-4, the metastable cubic phase is depicted. The cubic rock salt unit cell is highlighted by purple lines. At this point it should be mentioned that the cubic rock salt type is actually a rhombohedral structure with the same type of Peierls distortions as for GeTe, but the distortions are so small that they are not detectable with conventional XRD techniques (due to the averaging nature of the measurements). Only by using anomalous scattering at the element edges (extended x-ray absorption fine structure analysis and x-ray absorption near edge structure), these observations have been observed^[34]. However, it is not surprising since both GeTe and Sb-Te compounds exhibit the same type of distortions (see section 2.2.1). For all practical purposes though, it suffices to say that the metastable GST225 phase is of rock salt type. The lattice parameter is reported to be 0.603±0.003^[57-61] nm by different investigators. In this thesis a lattice parameter of 0.603 is used throughout for comparison^[62]. The rock salt structure can be described by two FCC sublattices, shifted half a unit cell from each other. One is occupied solely by Te atoms whereas the other contains Ge, Sb and ~20% vacancies in a random way. Alternatively, the distorted rock salt structure can also be described by a hexagonal lattice. This is indicated by the red outline in Figure 2-4a. The hexagonal representation consists of a six layer period where anion (Te) and cation (Ge, Sb, vacancy) layers are alternating. Viewed along the [110] (or [-2110] using hexagonal indices), the structure is visualized as in Figure 2-4b. The red solid line indicates one set of (111) planes, which is inclined at an angle of 70.56° with the horizontal (111) planes (blue Te layers). The grey box indicates the size of the corresponding hexagonal unit cell.

The GST225 also possess a high temperature hexagonal equilibrium phase. The phase transition temperature is typically around 300°C^[57] and normally this phase is not obtained by short pulse laser irradiation^[63]. The hexagonal structure (space group *P-3m1*) consists of a nine layer period in the form of *Te-A-Te-B-Te-VL-Te-B-Te-A*. The actual site occupancy of *A* and *B* varies from model to model expressed as *A*:*B*: Ge₅₆Sb₄₄:Ge₄₄Sb₅₆ (Matsunaga et al.^[62]), Ge:Sb (Kooi and De Hosson^[64]) or ~Ge₆₅Sb₃₅:Ge₃₅Sb₆₅ (Urban et al.^[65]). The intrinsic vacancies in the compound are now located in the vacancy layers (VL) in contrast

to being randomly distributed in the lattice as in the rock salt structure. The VL should appear between every fifth Te layer, but the actual stacking sequence is very sensitive to the local chemical composition^[64]. In between each VL the stacking sequence is that of cubic, i.e. ...*ABCABC*... but each block is shifted between each VL so that the overall stacking sequence is hexagonal. In Figure 2-4c, the crystal structure of hexagonal GST225 according to Matsunaga et al.^[62] is presented. It is viewed along the $[-2110]$. The grey box displays the hexagonal unit cell in this projection. According to the different structure models mention above, the lattice parameters ranges from $a = 0.4224\text{-}0.4250$ nm and $c = 1.724\text{-}1.728$ nm. In the figure lattice planes that are analogous to cubic (111) planes, i.e. hexagonal (20-23), are indicated. These planes do not form continues lines but are offset between each VL. This is unique for the hexagonal phases in the $\text{GeTe-Sb}_2\text{Te}_3$ system and can in some cases be used to distinguish between a cubic or hexagonal phase (see Figure 4-32).

Density functional theory calculations have shown that there might be a parameter space where the metastable distorted rock salt structure might exist as a hexagonal layered cubic phase^[66-68]. The differences between the calculations only lie in the exact stacking sequence or site occupancy of Ge and Sb. In all cases the layered cubic phase only differs with a few meV/atom from the stable hexagonal phase, i.e. they are very close in energy. One such structure model is presented in Figure 2-4d (Da Silva et al^[66]). Clearly the structure is built up of blocks separated by vacancy layers with identical spacing and intra-block stacking as

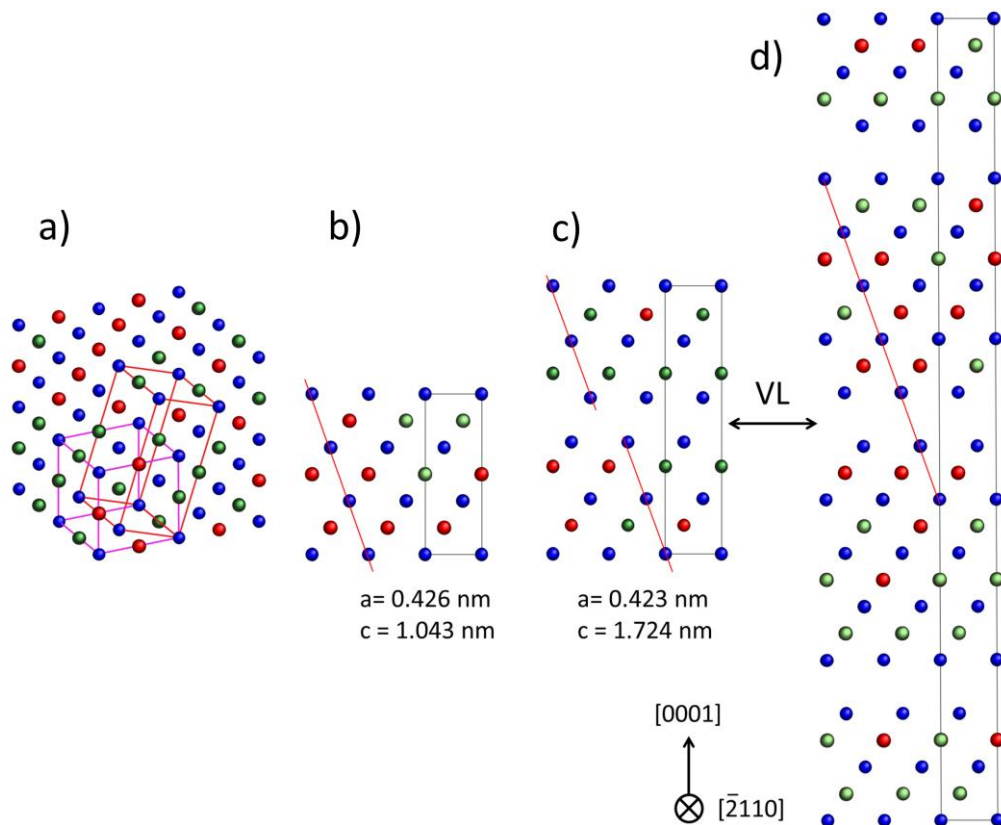


Figure 2-4. Crystal structure of cubic (a,b), hexagonal (c) and layered cubic (d) GST225. The green, red and blue spheres symbolize Ge, Sb and Te, respectively. Vacancies in (a,b) are not shown for clarity. The red lines in (b) mark (111) planes and the hexagonal corresponding ones in (c,d).

in the stable hexagonal phase, i.e. 5 Te layers in between each VL and ...*ABCABC*... stacking. The only difference between the stable hexagonal phase and the layered cubic phase is a shift of the blocks in between each VL. This is evidenced from the solid red line in Figure 2-4, which marks the lattice planes analogue to the cubic (111) planes. No offset across the VL is seen. Another way to describe this structure is to stack 4 unit cells of metastable GST225, as in Figure 2-4b, and then subsequently concentrate the randomly distributed vacancies into a vacancy layer, i.e. removing every fifth Ge/Sb layer. By doing so the unit cell becomes 4 times larger in the c-direction as indicated by the grey box in Figure 2-4d. The whole structure is then relaxed to obtain the correct bond lengths and angles. Such a structure has not yet been fully experimentally validated, but there are some indications that this structure might exist (see section 4.2.1 and Ref. 69).

2.2.3. Crystal structures of $\text{Ge}_1\text{Sb}_2\text{Te}_4$

GeSb_2Te_4 is the equivalence of $(\text{GeTe})_1(\text{Sb}_2\text{Te}_3)_1$ and belong to the intermetallic compounds that are more enriched with Sb_2Te_3 , compared to GST225 (see Figure 2-2). From here on this composition will be referred to as GST124 for simplicity. The higher percentage of Sb_2Te_3 leads to a slightly higher vacancy concentrations of about 25%, compared to 20% for GST225. The crystal structure of metastable GeSb_2Te_4 is completely analogue with the corresponding GST225 phase, i.e. a slightly distorted rhombohedral unit cell^[70] which for all practical purposes can be described as a cubic rock salt structure. In fact these distortions have been shown to persist throughout the whole GeTe-Sb₂Te₃ system^[71]. In the rock salt structure, the Te atoms occupy one sub-lattice, whereas Ge, Sb and vacancies share the other one and it is outlined in purple in Figure 2-5a. This phase forms at annealing temperatures above 130°C^[31] or by means of short pulse laser irradiation. Also shown in Figure 2-5 is the hexagonal representation of the cubic phase (red lines) and a view of this structure is shown in Figure 2-5b. The hexagonal representation consists of a six layer period where anion (Te) and cation (Ge, Sb, vacancy) layers are alternating. Viewed along the [110] (or [-2110] using hexagonal indices). The red solid line indicates one set of (111) planes, which is inclined at an angle of 70.56° with the horizontal (111) planes (blue Te layers). The grey box indicates the size of the corresponding hexagonal unit cell.

The GST124 also possess a high temperature hexagonal equilibrium phase. The phase transition temperature is typically around 210°C^[31]. The hexagonal structure (space group *R-3m*) consists of a 21 layer period with alternating close-packed Te layers and Ge/Sb layers and VLs in between every fourth Te atomic layer^[72,73]. The denser VL spacing compared to GST225 just reflects the higher concentration of vacancies. In between each VL the stacking sequence is that of cubic, i.e. ...*ABCABC*... but each block is shifted between each VL so that the overall stacking sequence is hexagonal. In Figure 2-5c, the crystal structure of hexagonal GST225 according to Matsunaga et al.^[73] is presented. It is viewed along the [-2110]. The grey box displays the hexagonal unit cell in this projection. According to the different structure models mention above, the lattice parameters ranges from $a = 0.424\text{--}0.4270$ nm and $c = 4.112\text{--}4.169$ nm. In the figure lattice planes that are analogous to cubic (111) planes are indicated as already explained in Figure 2-4. These planes do not form continuous lines but are offset between each VL.

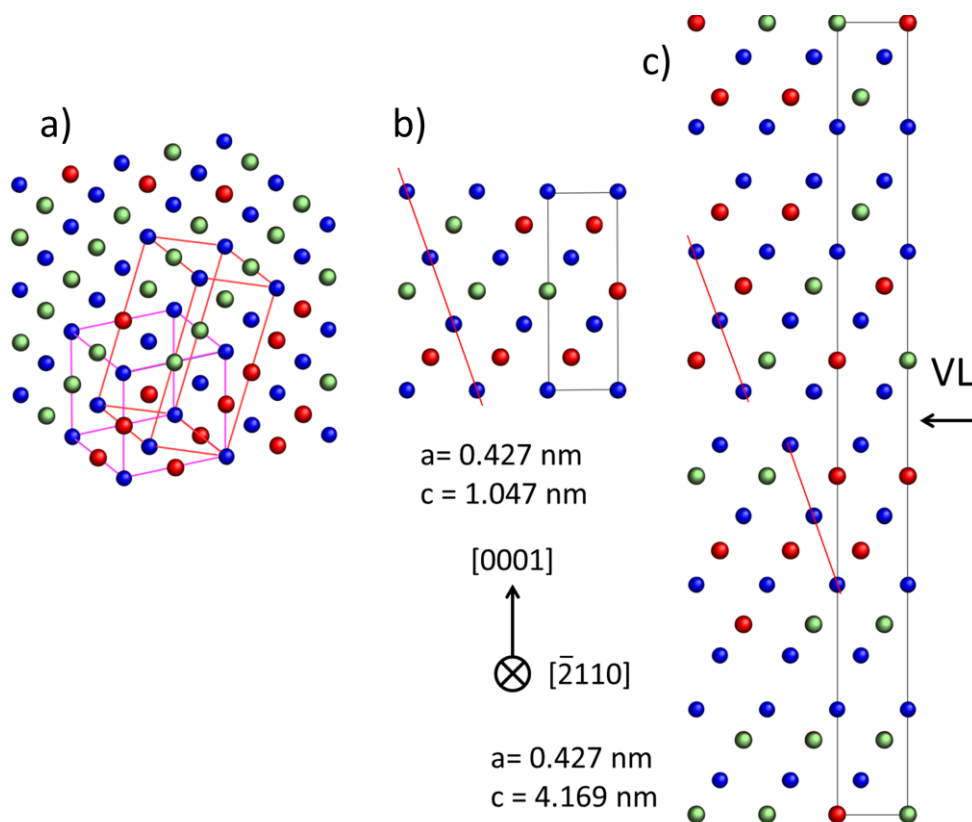


Figure 2-5. Crystal structure of cubic (a,b) and hexagonal (c) GST124. The green, red and blue spheres symbolize Ge, Sb and Te, respectively. Vacancies in (a,b) are not shown for clarity. The red lines in (b) mark (111) planes and the hexagonal corresponding ones in (c).

There are more stoichiometric compounds in the homologous $\text{GeTe-Sb}_2\text{Te}_3$ series, but they are not relevant for this thesis. The interested reader can find more information in Refs. 54,55,71,74

2.2.4. Crystallographic data from Ge-Sb-Te compounds

As described in the previous sections, the GST225 and GST124 possess very similar crystal structures. In the metastable state they are completely analogue with the exception that GST124 have a slightly larger unit cell. This can be explained by the increased concentration of Sb in GST124 which leads to an expansion of the unit cell. This is true also for the hexagonal phase of GST124 where the basal hexagonal lattice parameter is slightly larger than for GST225 and the c-direction is also slightly larger than the length of two GST225 hexagonal unit cells, i.e. 12 Te layers. The hexagonal phases of the two compounds are further differentiated by the different stacking order of the VLs. These crystal structure differences produce subtle but clear differences in the corresponding x-ray diffractograms and since much of the results in this thesis are based upon x-ray data and the comparison between different phases it is worth having a closer look upon.

In Figure 2-6, calculated x-ray profiles for GST225 and GST124 are presented. The two topmost diffractogram represents the cubic phases and clearly they look very alike. Both show the typical appearance of a face centered cubic lattice, i.e. only all odd or all even (hkl) reflections are visible. Furthermore, the peaks are shifted to lower diffraction angles

for the GST124, visualizing the slightly larger unit cell of GST124. The (200) reflection is the strongest one, whereas the (111) show $\sim 10\%$ of the maximum intensity. It should be noted here that the intensity calculations have been done with a fixed temperature factor and does not necessarily reflect the true relative intensities. However, the same temperature factor was used for all calculations and the relative intensities do not change much when the temperature factor is varied. Therefore it can be used as an estimate of which relative intensities one can expect. The small differences between the two cubic phases show that care must be taken when determining the exact crystal structure and x-ray measurements should always be accompanied with other characterization methods. It should also be noted that all cubic reflections have a corresponding hexagonal peak in the near vicinity, which reflects the close relation between the two phases.

The hexagonal crystal structures are displayed in the two bottommost diffractogram. The hexagonal phase, being a more low symmetry phase show a higher amount of Bragg peaks. Also the differences between GST225 and GST124 are larger when comparing the two. The indices differ of course quite much since the hexagonal unit cells possess largely different c-axis. This is especially noticeable when regarding the reflections below 25° . These reflections all belong to $(000l)$ planes and are directly related to the vacancy ordering in the structures. All of the $(000l)$ reflections are weakly scattering ones, of around 1% of the most intense peak. The most intense peak resides between 28.40° and 28.93° for GST124 and GST225, respectively. This is the crystallographic equivalent planes to the (200) planes in the cubic structures. The second most intense peak is the (2-1-10) reflection at $42.3-42.8^\circ$ and this is the crystallographic equivalent to the (220) planes positioned at 90° angle with the (111) planes in the cubic phase. A third intense peak ((10-1-6) or (10-1-14)) is positioned around 39° and this is a unique peak for the hexagonal phase and can be used for determining if the crystal structure is indeed hexagonal or not.

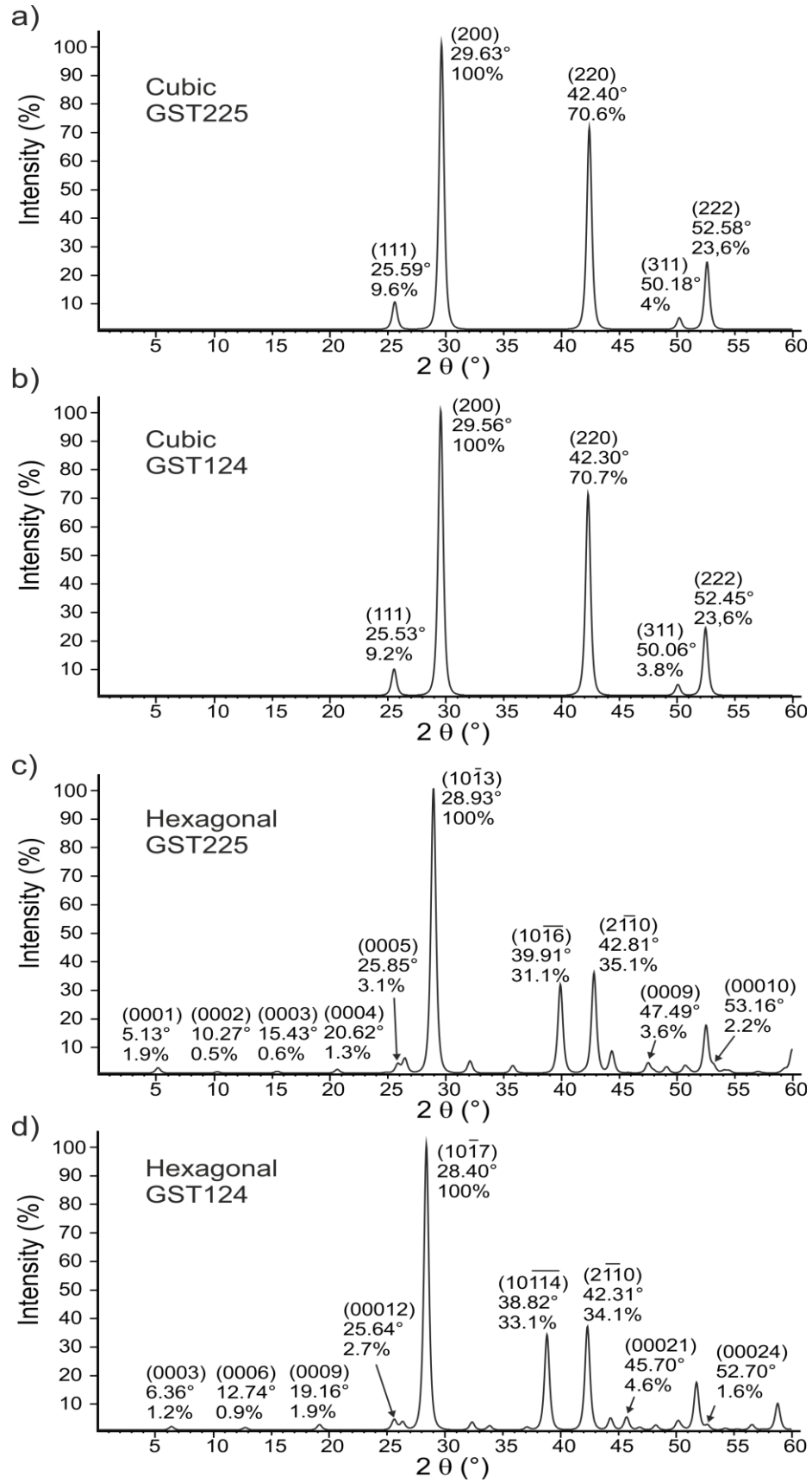


Figure 2-6. Calculated x-ray diffraction profiles for different GST phases^[75]. Each annotation shows Miller indices, Bragg angle and relative intensity.

Chapter 3

Experimental methods & materials

3.1. Pulsed laser deposition

In this study, Pulsed Laser Deposition (PLD) was used to deposit thin films of Ge-Sb-Te. PLD as a deposition method dates back to the invention of the ruby laser in the nineteen sixties^[76], when Smith and Turner ablated powder materials in a vacuum bell jar^[77]. Interestingly, among the materials being ablated was GeTe, one of the binary compounds in GST which is used in this study. I took more than 20 years, though, before PLD as a thin film deposition method had its first breakthrough with the discovery of high temperature superconductors^[78]. These superconductor materials are oxide ceramics with a perovskite-like crystal structure and PLD was the first method that could transfer the complex composition from the bulk target material to the resulting thin film. After this major finding, PLD as a method gained a lot of interest, especially in the field of oxide thin films. Nowadays, PLD is an established research method for the deposition of thin films of complex stoichiometry and it is in this context, the method was used in this study.

3.1.1. Working principle and setup

The use of a pulsed laser source with short pulse duration ($\sim 10\text{-}30$ ns) is of utmost importance in laser ablation. The short pulses make sure that the instant light intensity is high enough to overcome the ablation threshold and thereby obtaining the sought-after characteristic, i.e. accurate stoichiometric transfer. Longer pulses or even continuous wave laser irradiation leads to conditions close to thermal equilibrium and therefore classical evaporation and melting takes place. For an effective ablation, the absorption coefficient of the target material should be as high as possible at the used laser wavelength, or alternatively formulated, a laser wavelength should be chosen where maximum absorption takes place. This reduces the surface layer thickness which is heated in the target by the laser pulse, the so called skin depth. A low skin depth constricts the energy in the laser pulse to a very shallow surface region and therefore makes it possible to reach the high temperatures and heating rates needed for congruent ablation. The material being ablated is then expelled from the surface with a highly forward directed species distribution, the so called plasma plume. Often the plasma plume can be described with a $\cos^n \alpha$ distribution, with $4 < n > 20$, see Ref. 79. The plasma plume contains a number of different species, involving electrons, ions, neutrals, clusters and larger particulates. The kinetic energies of the ions and neutrals in the plasma plume spans the range from one to several hundred eV, which is significantly higher than normal evaporation processes with thermal energies (MBE ~ 0.2 eV). Such high kinetic energies could influence the growth process, since the kinetic

energy of the condensing species is (among other processes) transformed into surface diffusional energy.

The laser used in this thesis was a KrF excimer laser (LPXro 240, Coherent), which emits light at a wavelength of 248 nm with 20 ns pulse duration. The pulse energy was typically set to 160 mJ and the fluence on the target was controlled with the focal position of the lens. The fluence used in this study normally ranged between 0.5-1 J/cm². The pulse repetition rate was varied between 1 and 100 Hz. The target material used was an arc melted Ge₂Sb₂Te₅ target (ACI ALLOYS Inc.). Ge₂Sb₂Te₅ has a high absorption coefficient in the UV-range ($\sim 10^6$ cm⁻¹)^[80] and is therefore suitable for the PLD process. In Figure 3-1, a schematic view of the deposition system is shown. Insertion and removal of samples and targets is handled by the load-lock attached to the chamber. The laser beam enters the deposition chamber through a quartz window at a 60° normal incidence with the target. Behind the window, a gate valve has been placed, which makes it possible to separate the laser entry window and the deposition chamber. This enables the removal and cleaning of the laser entry window without breaking the vacuum in the main chamber. With this setup a regular base pressure of $4 \cdot 10^{-8}$ mbar is maintained. The laser beam is projected on the target surface with a plano-convex lens ($f \approx 800$ mm) which resides on a slide. In that way the laser fluence on the target can be adjusted. Inside the chamber a target carousel is used which can hold three different targets, simultaneously. The substrate holder is mounted perpendicularly to the target manipulator with a spacing of roughly 6.5 cm. Moreover, it is possible to move the substrate manipulator laterally to find the best deposition position. Inside the substrate holder a resistive heater is placed which enables heater temperatures up to 1100°C. For more information about PLD the reader is referred to Refs. 79 and 81.

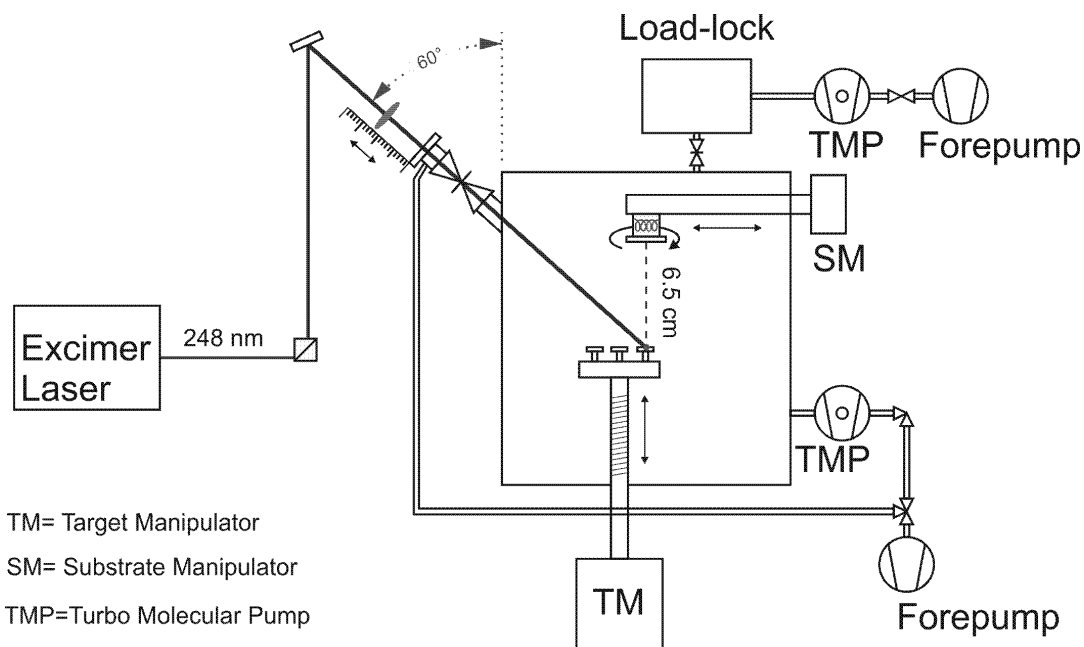


Figure 3-1. Schematic of PLD system

3.2. Sample preparation and treatment

3.2.1. Substrate materials and preparation

In this study three different substrate materials have been used: KCl, BaF₂ and Si. All crystals are cubic with a rock salt, fluorite and diamond structure and the crystal structure is displayed in the upper part of Figure 3-2a-c, for KCl, BaF₂ and Si, respectively. The corresponding lattice planes used for growth are depicted in the bottom part of the figure. The typical substrate size was $\sim 10 \times 10$ mm². KCl and BaF₂ were purchased as rectangular shaped bulk crystals (Plano GmbH, Korth Kristalle GmbH) with size of $10 \times 10 \times l$ mm³, with $10 < l > 50$ mm. The crystals were then cleaved parallel to the cleavage planes with a sharp single-sided razorblade and a small hammer. Typical thicknesses of the cleaved substrate pieces were 1.0-1.5 mm. The freshly cleaved substrates were then mounted and directly inserted into the load lock chamber. The Si substrates were purchased as wafers and divided into smaller pieces. The Si(100) pieces were degreased ultrasonically in ethanol followed by acetone and then stored under ambient conditions in boxes. The Si(111) substrate pieces underwent a RCA treatment^[82] and were then stored in the clean room. Directly prior to deposition a Si(111) piece was dipped in buffered ammonium fluoride (BAF, 7:1 volume ratio of 40% NH₄F in water and 49% HF in water) for 30 seconds, rinsed with deionized water, dried and transferred to the load-lock. The substrate preparation details are summarized in Table 1.

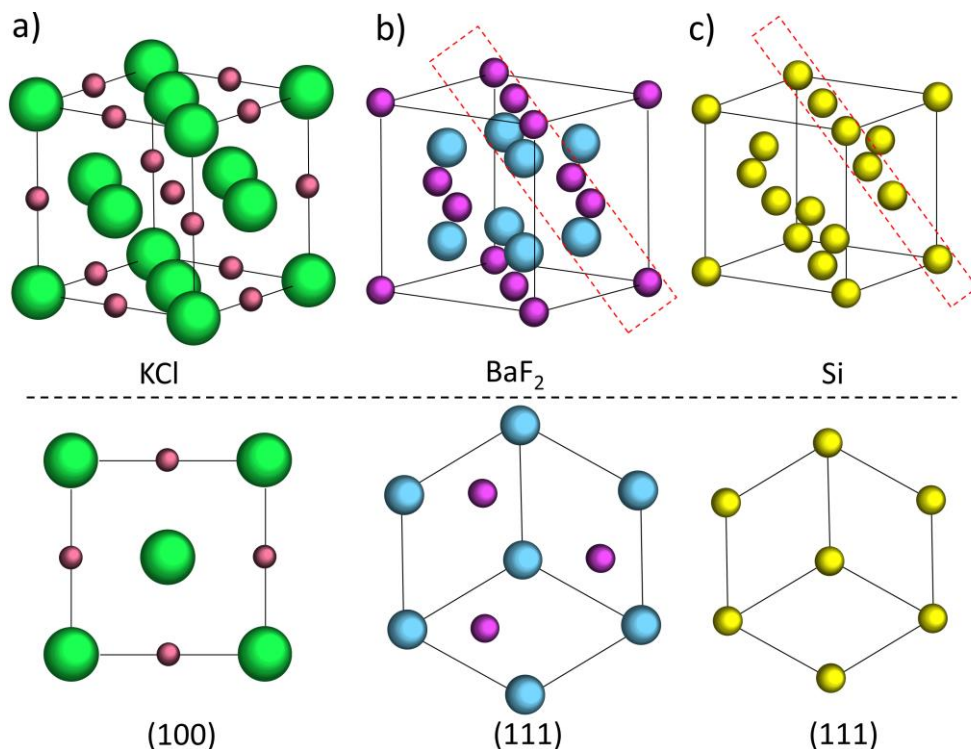


Figure 3-2. Crystal structures of used substrate materials (upper half) and the corresponding substrate crystallographic lattice plane projection used for epitaxial growth. The red dashed tilted boxes indicate the slice from where the projections stem from.

Table 1. Overview of the substrate materials used in this thesis.

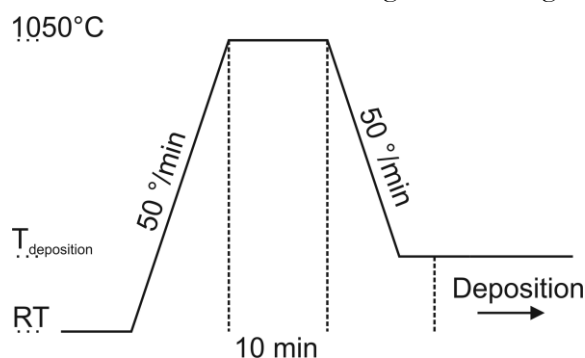
Substrate material	Crystal Orientation	Preparation	Time in air for bare substrates	Used for
Si	(100)	Pre-clean	-	Polycrystalline films (section 4.1)
KCl	(100)	Freshly cleaved	<5 min	Epitaxial films (section 4.2)
BaF ₂	(111)	Freshly cleaved	<5 min	Epitaxial films (section 4.3)
Si	(111)	RCA pre-clean and oxide etch with BAF	<5 min	Epitaxial films (section 4.4)

3.2.2. Substrate heat treatment prior to deposition

To investigate the influence of a thermal substrate treatment several Si(111) substrates were additionally subjected to a thermal pre-treatment in the deposition chamber prior to deposition (see section 4.4.2 for results). This treatment was carried out with the aim to obtain a 7×7 surface reconstruction^[83]. The heating ramp profile is presented in Figure 3-3.

3.2.3. Substrate temperature calibration

The heater temperature was normally set to temperatures in the range between 100-500°C. This is a temperature interval which is hard to measure with optical pyrometers. Therefore, a different approach was developed. On a substrate a thin (0.25 mm) type C thermocouple wire was attached. The measurement point was pinned to the substrate surface using ceramic cement (Omegabond CC High Temp). Care was taken to use as little as possible of the cement. The substrate (with thermocouple) was then placed on the substrate manipulator by hand and the chamber was then evacuated to a pressure below 10^{-5} mbar. After this the substrate heater was heated to a set point temperature and hold for 30 minutes. Only thereafter was the temperature read out from the thermocouple. This procedure was repeated for each different substrate materials, but was only done once per substrate material, due to the time consuming preparation. The uncertainty in the measurements is estimated to be $\pm 30^\circ$. Nevertheless, it gives a feeling of the discrepancy be-


Figure 3-3. Temperature profile for Si substrate thermal treatment

$$\frac{1}{d_{hkl}^2} = \frac{4}{3} \left(\frac{h^2 + hk + k^2}{a^2} \right) + \frac{l^2}{c^2} \quad (3)$$

Almost all films in this thesis were investigated with a Rigaku Ultima IV Type 3 diffractometer using parallel beam geometry and Cu K_α radiation (λ=0.15418 nm). No additional x-ray optics, like monochromator and analyzer crystals, were used in order to maximize the diffracted intensity. However, selected films were additionally investigated on a Seifert XRD 3003 PTS, which utilizes a parallel beam with monochromatic Cu K_{α1} radiation (λ = 0.15406 nm (2-bounce Ge(220) crystal primary monochromator). A schematic goniometer geometry can be seen in Figure 3-5 which applies for both diffractometers. The axes can be moved independently (only partly for the Rigaku Ultima IV Type 3), allowing the following measurement modes:

- 2θ-ω-scans are used for determining crystal structure and lattice plane spacing. The angular resolution in 2θ was varied between 0.05-0.11° using slits and a parallel slit analyzer. In this mode the ω and 2θ axis are coupled so that the 2θ axis moves with twice the speed compared to the ω axis.
- ω-scans (rocking curves) can be used for determining the crystallite tilt distribution of the films and therefore a measure of how well oriented a textured/epitaxial film is. In this mode the 2θ axis is fixed at a certain angle corresponding to a selected Bragg reflection and the ω axis is scanned (rocked).
- φ-scans of a certain {hkl} family give information about epitaxial relationships and can in some cases be used for differentiating between different polytypes (cubic or hexagonal). The Rigaku diffractometer utilizes an in-plane arm for measuring φ-scans. This means that the sample always stays horizontal and the goniometer axes are positioned in such a way that all angles are satisfied (tilt angle and Bragg angle). Therefore the tilt axis is called α in Figure 3-5 and not χ as normal.

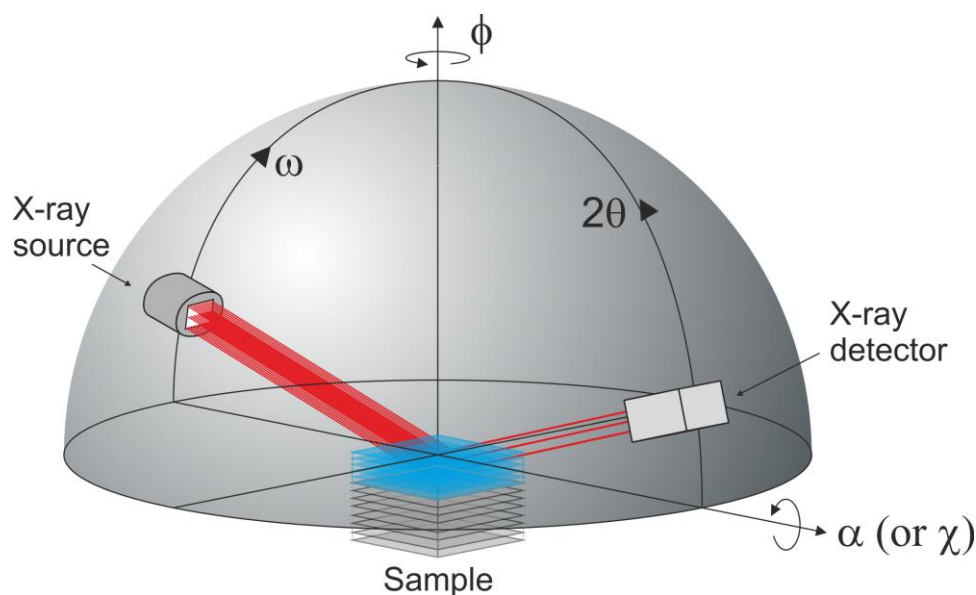


Figure 3-5. Schematic of the goniometer geometry

For a more detailed description of each measurement technique the reader is referred to a standard textbook, for instance see Ref. 84

The in-plane arm in the diffractometer (2θ -axis) actually makes it possible to measure in-plane diffraction profiles, rocking curves and pole figures which are advised when trying to understand complicated crystal structures. These measurements will be presented in their own sections following this one.

In-plane x-ray diffraction

A large part of the XRD measurements in this study has been conducted in an in-plane mode. Since this method is not as common yet in laboratory diffractometers, it deserves a more detailed description. Compared to normal out-of-plane XRD, in-plane XRD (ipXRD) is a relatively new method. It was practically realized as a measurement technique as late as 1979 by Marra et al.^[85]. By adding an additional goniometer axis (in-plane arm) to a normal laboratory diffractometer it becomes possible to perform these measurements routinely. In ipXRD, irradiation of the sample proceeds in the vicinity of the angle of total external reflection. About this angle, a refracted x-ray wave propagates more or less parallel to the surface. This wave is evanescent in nature and is damped in the z-direction with an exponential dependence on the incidence angle^[86]. However, within the surface plane the wave can propagate undisturbed and can therefore be used for diffraction studies of lattice planes that lie perpendicular to the surface plane. The critical angle θ_c of total external reflection is dependent on the irradiation wavelength λ and the density of the film material ρ according to:

$$\theta_c = \sqrt{2\delta} = \lambda \sqrt{\frac{r_0 N_a f_1}{\pi A}} \cdot \rho \quad (4)$$

Where δ is the decrement from 1 of the real part of the refractive index, i.e. $n = 1 - \delta$. N_a is Avogadro's number, r_0 is the Bohr radius, A the atomic weight and f_1 the real part of the atomic form factor. This yields a critical angle of below 0.6° for most materials. Such a low (grazing) incident angle of course requires that the beam divergence is small, and for that purpose a parallel beam is required. In Figure 3-6, a detailed schematic of the in-plane geometry in the Rigaku Ultima IV Type 3 is illustrated. In the top part of the figure the geometry is viewed from the side. The graded parabolic multilayer mirror parallelizes the beam ($\sim 0.05^\circ$ divergence) in the vertical direction and the vertical Soller slits on the primary and secondary side make the beam less divergent in the horizontal plane. The incident slit width W_{slit} together with the incident angle ω determines the projected beam spot length W on the sample according to $W = W_{slit} / \sin \omega$, and a balance needs to be found between maximum diffracted intensity and background noise level. The angular position of the 2θ (detector) arm is not that critical, since the slits on the receiving side are open during measurement and could normally be placed between 0 and 2° without any difference in intensity. In the bottom part of the figure, a top view of the geometry is depicted. In this view, the function of the vertical Soller slits is easier to visualize.

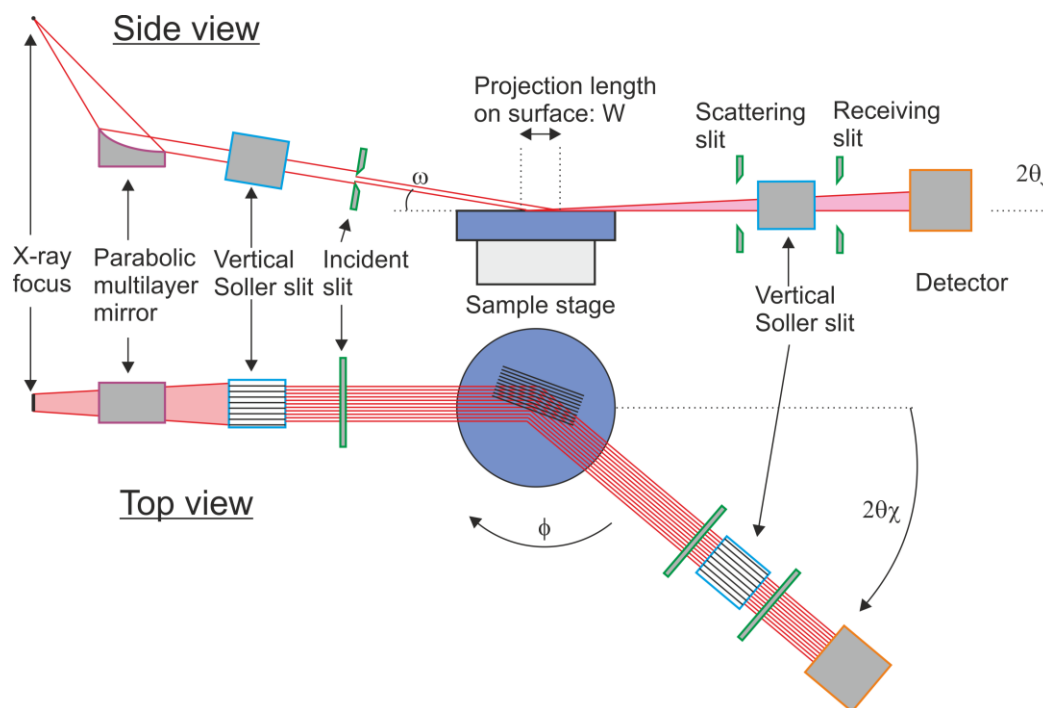


Figure 3-6. Side and top view of the in-plane geometry in the Rigaku Ultima IV Type 3. Image idea adapted from Ref. 87.

For an ipXRD measurement the $2\theta\chi$ -axis is moved with twice the speed of the φ -axis, i.e. a coupled $2\theta\chi$ - φ scan analogue to a common 2θ - ω out-of-plane scan. This measurement mode gives information about the vertical lattice planes in the film as can be seen in Figure 3-7a for an epitaxial GST films on a $\text{BaF}_2(111)$ substrate. This scan was measured with a 0.5° vertical Soller slit and the substrate peak and GST peak are clearly resolved. By changing to a 2.5° vertical Soller slit the angular resolution is lowered, but almost a factor of 10 in intensity is gained (Figure 3-7b). The two peaks are no longer individually resolved and the substrate peak is only visible as a shoulder on the left flank. However, the intensity gain is that large that measurement can be carried out at higher diffraction orders as displayed in Figure 3-7c, where the two peaks are once more individually resolved. Therefore, as always, a balance between angular resolution and diffracted intensity needs to be found. In general, the FWHM of the diffraction peaks is in good agreement with the stated angular divergence on the Soller slit. In this study, the 0.5° vertical Soller slits have been used almost exclusively. Deviations from this measurement setup are stated when called for. Although it is possible to measure polycrystalline samples, the method is more efficient for textured/epitaxial films.

If the sample is rotated around its own surface normal (φ -axis), an in-plane φ -scan is obtained. In this case the $2\theta\chi$ -axis is placed at the Bragg position of the reflection of interest and the sample is rocked about the $\theta\chi$ angle. In fact this is analogue to an out-of-plane ω -scan and can also be referred to as an in-plane rocking curve. The only difference is that the φ -axis can be rotated by 360° so that all planes belonging to that particular set of planes can be brought into diffraction conditions. The FWHM of the peaks are then a measure of the pure crystallite twist component in the films and the appearance of

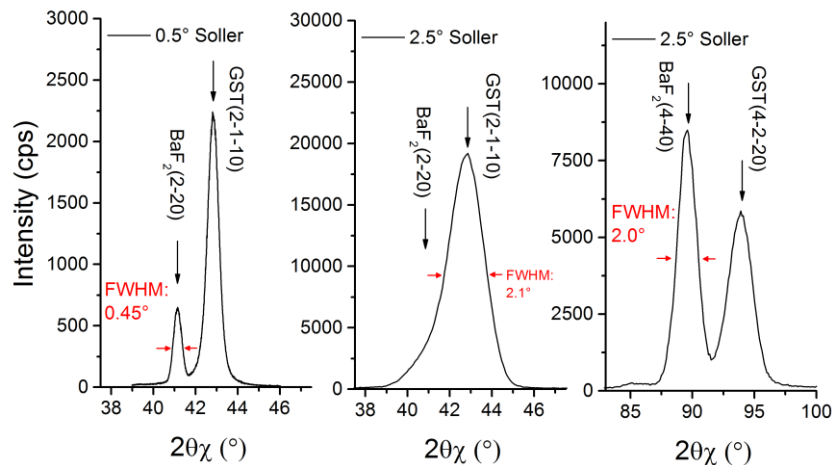


Figure 3-7. In-plane 2θ - ϕ scans of an epitaxial GST films on $\text{BaF}_2(111)$ measured with different vertical Soller slits, i.e. angular resolution

the scan, i.e. number of peaks and spacing gives clues about the crystal symmetry in the films. This is exemplified in Figure 3-8 where two ϕ -scans are shown for a hexagonal and cubic epitaxial GST film. The FWHM of each peak can be measured and in the general case they do not differ much. Also, from the azimuthal peak separation the respective in-plane symmetry is found. When an in-plane ϕ -scan of the substrate peak is additionally recorded, the epitaxial in-plane relationship between film and substrate can be determined. An in-plane ϕ -scan can in general, however, not differ between a (0001) oriented hexagonal phase and a (111) oriented cubic phase, since both crystal structures possess a six-fold in-plane symmetry.

Texture goniometry (in-plane pole figure measurements)

To determine the epitaxial relationship between films and substrate, in-plane pole figure measurements were carried out. An in-plane pole figure offers some advantages compared to classical pole figure measurements with the parallel beam reflection method. First of all, the sample can lie horizontally during the whole measurement. Secondly and more important is that a whole pole figure between $0^\circ < \alpha < 90^\circ$ can be recorded, since the in-plane arm is used and therefore vertical lattice planes are also registered. The disadvantage is that

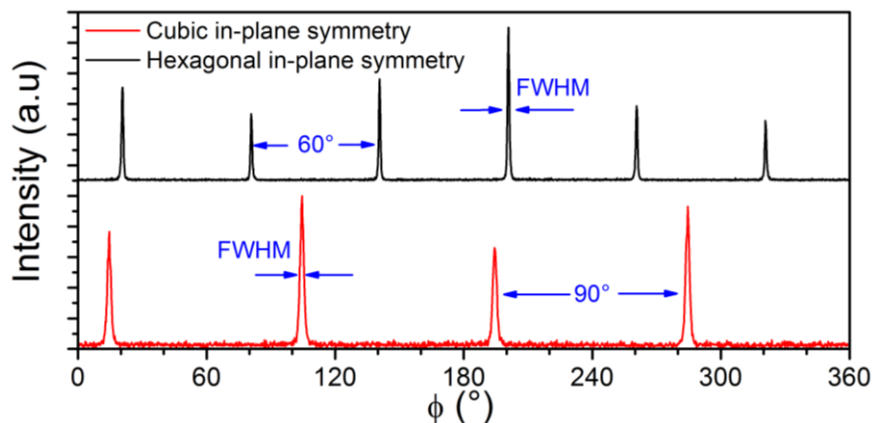


Figure 3-8. In-plane ϕ -scans of two epitaxial GST films on $\text{KCl}(100)$ (red) and $\text{BaF}_2(111)$ (black).

the tilt angle and Bragg angle of the sample do not correspond to individual goniometer axes anymore. Instead, the Bragg and the tilt angle position are calculated by the diffractometer software from the position of the ω , 2θ and $2\theta\chi$ axis. A simplified sketch of the geometry can be seen in Figure 3-9a. At $\alpha=0^\circ$ the x-ray source and the detector lie in the plane fulfilling the Bragg angle ($2\theta_B$). For each new subsequent measurement step, the goniometer axes (ω , 2θ , $2\theta\chi$) are moved in such a way that α and $2\theta_B$ positions are fulfilled. The movement sequences are roughly along the paths indicated in the figure. This is the reason why the tilt angle is called α and not χ as usual. At each α step, the sample is rotated 360° about its own axis (φ). At certain tilt and rotation angles, depending on the actual crystal structure, diffracted intensity is registered in the upper half of the pole sphere in Figure 3-9a. The intensity can then be plotted as a stereographic projection onto the equator plane of the sphere as indicated in the figure. Mathematically this is done by $r=90\cdot\tan(\alpha/2)$, where r is the new angular position and α the measured tilt angle. The stereographic projection represents then what is normally referred to as a pole figure. Such a projection is visible in Figure 3-9b where a $\{220\}$ pole figure of a Si(111) substrate has been measured. Two sets of pole density maxima can be seen, one at $\alpha\approx 90^\circ$ (outer rim) and one at $\alpha\approx 35^\circ$ which is to be expected for a (111) oriented sample. The pole density maxima are exceedingly narrow, due to the high crystalline quality of the Si material. Nevertheless, they are detectable. The outer set of pole density maxima could not have been detected with the classical reflection methods, but the in-plane geometry makes it possible to resolve these pole density maxima, too.

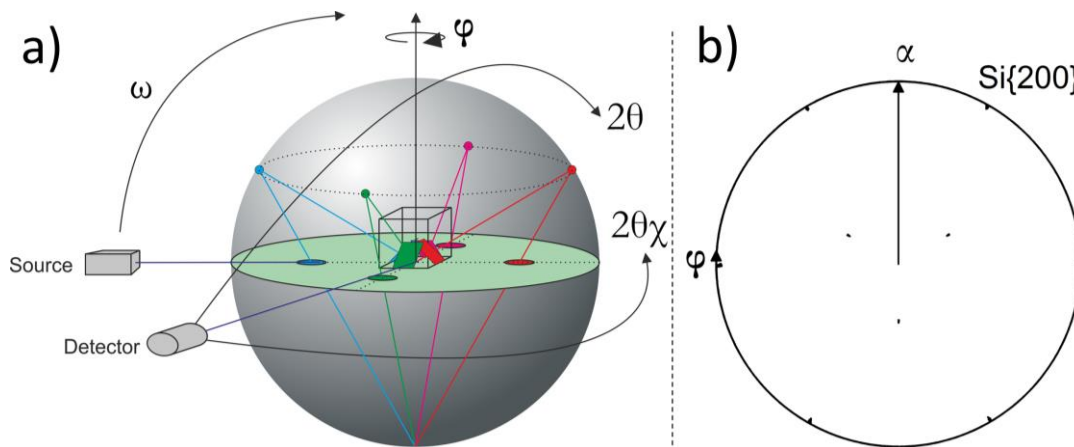


Figure 3-9. In-plane pole figure. Schematic view of the goniometer geometry used for texture measurements (a) and a measured pole figure of the Si{220} reflection(b).

X-ray reflectivity

An x-ray reflectivity (XRR) scan is in principle a 2θ - ω scan at small angles. However, completely different information is obtained with this measurement compared to a normal diffraction profile. At grazing incidence ($\omega < 0.5^\circ$) total external reflection takes place according to Eq. (4). In this angular region information about the density ρ of the film is obtained since θ_c is proportional to the square root of ρ . When the incident angle increases, the x-rays scatter at the substrate-film interface due to the difference in electron density and at certain angular positions constructive/destructive interference takes place. The

oscillating interference pattern is related to the thickness of the film and the amplitude of the oscillating signal is related to the difference in electron density between substrate and film (at low angles) and to interfacial roughness (at higher angles). The surface roughness determines the overall decay rate of the measured signal. Whereas an estimate of the thickness of the film can be obtained quite easily by a Fourier transform of the measured signal, a non-linear least squares fit routine is needed in order to simulate the full range of parameters, i.e. density, thickness and roughness (interface and surface). In this work the fit of the measured signal was carried out by the Analyze software within the RayfleX^[88] studio environment.

3.3.2. Imaging techniques including spectroscopy

Scanning electron microscopy

In a Scanning Electron Microscope (SEM) a focused electron beam with acceleration voltage between 0.1 and 50 keV is scanned over the surface of the sample. The electron beam interacts with the sample in many ways, producing mainly emission of secondary electrons, backscattered electrons and x-rays. In this study, the secondary electrons were exclusively used for imaging. Most of these electrons have a comparable low energy (5 to 100 eV) and therefore a very limited escape depth. The shallow surface region where the electrons stem from is limited to a few tens of nanometers (dependent on the acceleration voltage) and provides information about the surface topography. The emitted secondary electrons are then collected by either a biased Everhart-Thornley detector (positioned at a large angle with respect to the electron beam axis) or on an annular in-lens detector, and the generated signal is then amplified and finally presented on a display device which is linked to the scan coils of the scanning beam.

The used SEM was a Carl Zeiss Ultra 55 with a GEMINI[®] electron gun column. With this SEM a lateral resolution of ~30 nm was routinely obtained for GST films. Cross-section and plane-view images were recorded. For selected GST films on BaF₂(111) and KCl(100), a thin Al-coating was used, which improved the image acquisition due to suppression of charging effects. More information about the working principle of a SEM can be found in any material analysis textbook, for instance see Ref. 89.

Transmission electron microscopy

In a Transmission Electron Microscope (TEM), a thin sample (<200 nm) is illuminated by an electron beam of high acceleration voltage (typically a few 100 keV). Due to finite thickness of the TEM specimen, the electron beam is transmitted through the sample. The electron beam interacts with the atoms within the TEM specimen and the transmitted beam contains information about these interactions, for instance the crystal structure (or the lack thereof). In TEM mode (parallel illumination), different information can be obtained by choosing appropriate apertures and settings of the electronic lenses in the TEM column, i.e. real space images or diffraction patterns. If the electron beam is focused on and scanned across the specimen, the microscope is operated in Scanning Transmission Electron Microscopy (STEM) mode. Analytic measurement techniques (electron energy loss spectroscopy or energy dispersive x-ray spectroscopy) can be used to gain chemical information about the sample both in TEM and STEM mode. In STEM mode it is possi-

ble to perform analytics with a high spatial resolution since the electron beam is focused into a very fine probe. Hence the analytic signal only stem from a small interaction volume and a map can be obtained. For atomic resolution images (both in TEM and STEM mode), it is advantageous to have a spherical aberration corrected (C_s -corrected) microscope, which reduces the errors that occur when manipulating an electron beam with electromagnetic lenses. The invention and realization of C_s -corrected microscopes is fairly new^[90,91], but nowadays they are available for purchase both as image or probe corrected versions. For a more detailed description of TEM operation the reader is referred to Ref. 92.

In this study a probe C_s -corrected FEI Titan³ G2 60-300 was used for both TEM and STEM. The microscope uses a high-brightness Schottky type field-emission emitter for the generation of an electron beam with a narrow wavelength distribution and excellent temporal stability. The preparation of the TEM-lamellae was carried out by Focused (Gallium) Ion Beam (FIB) milling and subsequent low-kV Argon ion thinning (Nanomill). Typical thicknesses of the TEM-lamellae were between 20-50 nm. For details of the FIB-preparation, the reader is referred to Ref. 93. Diffraction patterns were obtained with either Selected Area Diffraction (SAD) or Nano Beam Diffraction (NBD)^[94]. In STEM mode the atomic resolution images were obtained with a High Angle Annular Dark Field (HAADF) detector, typically covering a collection semiangle range from 80 to 200 mrad. Energy dispersive x-ray spectra were obtained in TEM and STEM mode using a Super-X fourfold EDX detector array.

Energy dispersive x-ray spectroscopy

Energy Dispersive X-ray spectroscopy (EDX) in an electron microscope utilizes the inelastic interactions of energetic electrons with matter. When an electron enters a material it can scatter inelastically with the nucleus or the surrounding electrons. The former produces a continuous x-ray spectrum known as Bremsstrahlung and the latter produces characteristic x-rays. The characteristic x-rays (and Auger electrons) are produced when the incoming electrons knock out an inner shell electron from the atom. The excited state quickly relaxes by filling the hole with an outer shell electron. The energy difference between the inner and outer shell is equal to the wavelength of the emitted x-rays. The x-rays are then detected by an energy dispersive detector (XFlash[®] silicon drift detector) which generates an electronic impulse which amplitude is related to the energy of the incoming x-ray photon. In that way a histogram is built up and from this histogram the elements contained in the sample can be identified. For the quantitative analysis, the EDX spectrum is then subjected to a standardless evaluation routine (ZAF correction) and the Bremsstrahlung is subtracted. This yields atomic concentrations for thick films or bulk samples with an accuracy of about 2% on the average. However, for thin films where the incident electron beam excites a vast part of the substrate, the substrate signal dominates the spectrum and it is not possible anymore to obtain absolute atomic concentrations only for the film. The ratio, though, between the elements are still the same and can be used for estimating the stoichiometry. This is exemplified in Figure 3-10, where two EDX measurements obtained from the SEM are presented. The red curve symbolizes a GST film on Si and the black curve the GST target. Clearly, the Si peak dominates the images. Otherwise the spectra are very similar in appearance. They only matter in intensity, due to the fact

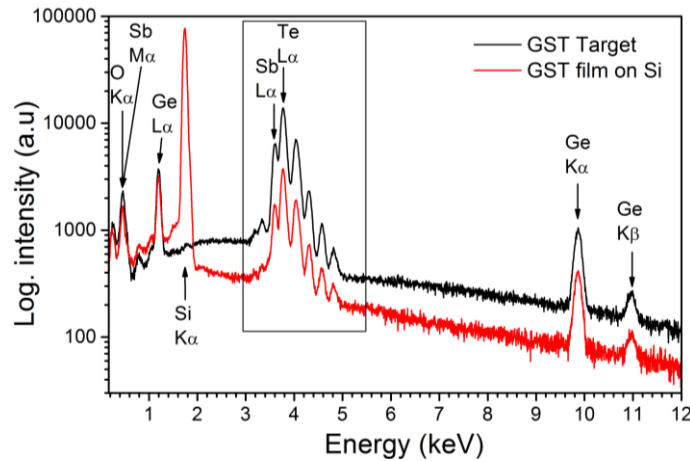


Figure 3-10. EDX measurements of GST samples. Peaks inside the box all belong to the Sb and Te L spectral lines.

that no background subtraction has been carried out and that the GST volume differs from sample to sample.

The absolute atomic concentrations extracted from the above measurements^[95] are presented in the first row in Table 2 for the GST target.. The suggested concentrations are fairly close to the expected GST225 composition considering the 2% error and the values seem plausible. The GST film on Si on the other hand, gives absolute concentrations as presented on the third row in Table 2. Clearly, this does not reflect the absolute concentration of Ge, Sb and Te in the film, but also includes Si to a depth of roughly 2 μm . All in all, the concentrations are not to be trusted as absolute. However, the ratio between the Ge:Sb:Te concentrations can be formed and taken as an indicator of the stoichiometry. The Te concentration was normalized to a fractional concentration of 5 (as in $\text{Ge}_2\text{Sb}_2\text{Te}_5$) and the Ge and Sb were multiplied with the same factor. The result can be seen on the second and fourth row in Table 2. The ratios for the two samples are now quite similar even though one sample is a bulk material and the other a thin film. Although this method does not provide the absolute atomic concentration it reveals effectively compositional trends in the films and this was used throughout this study. The uncertainty in these measurements was estimated to be significantly higher than for pure bulk samples, due to the low absolute atomic concentrations. Therefore each GST film was measured on at least four different places on the film to obtain better statistic. Selected films were also measured with EDX in the TEM, where it is also possible to obtain correct absolute atomic concentrations without any substrate signal disturbing the measurements. These measurements always agreed well with the EDX measurements obtained from the SEM.

Table 2. Absolute atomic concentration of GST samples measured with EDX

Sample	Ge	Sb	Te	Si
GST target (at.%)	23.1	24.4	52.5	-
GST target (atomic ratio)	2.2	2.3	5	Not applicable
GST on Si (at.%)	2.9	3.0	6.0	88.1
GST on Si (atomic ratio)	2.4	2.5	5	Not applicable

Atomic force microscopy

In this thesis Atomic Force Microscopy (AFM) was used to gain insights on the microscopic topography in intermittent contact mode (Tapping Mode[®]). Thereby, a small cantilever with a sharply etched Si tip is driven at a certain resonance frequency. In free air, the resonance oscillation has a certain amplitude of known value. When the tip is in contact with the surface (intermittent or tapping), the amplitude reduces due to loss of energy to the surface. The amplitude of the cantilever oscillations is recorded with the help of a laser beam and position sensitive photo diodes, which with the help of a feedback controller regulates the height of the scanning head. In this way, the software tries to maintain a certain amplitude of the oscillations and the z-value at each (x,y) position is recorded and forms the microscopy image. It is possible to obtain quantified data from the acquired image by applying statistical analysis. In this study the root mean square roughness (*rms*) has been used for quantitative comparison of the different films. It is defined as^[96]:

$$R_{rms} = \sqrt{\frac{1}{n} \sum_{i=1}^n Z_i^2} \quad (5)$$

for n measurement points with value Z_i . Here, Z_i refers to the measured height value in nm. For more detailed information about AFM, the reader is referred to Ref. 96.

Chapter 4

Results & discussion

The investigations on the growth of GST films can be classified according to two main topics: Growth of polycrystalline GST and growth of epitaxial GST films. The investigations on polycrystalline growth will be described in the next section, whereas the epitaxial growth will be discussed subsequently. The investigations of the epitaxial growth of GST are furthermore divided into three sections, each dealing with a different substrate.

4.1. Growth of polycrystalline GST films

In this section the results of the polycrystalline growth of GST films deposited with PLD will be discussed. Typically, $1 \times 1 \text{ cm}^2$ Si(100) with the native oxide layer still present was used as substrate. Other typical deposition conditions used are presented in the table below. It should be noted that, although many different parameters were tried, the aim of this investigation was not to probe all parameters in a systematic way in order to derive physical models of the ablation process, but more to explore how the GST material behaves under different deposition conditions. In other words, it acted as an initial investigation prior to the investigations of the epitaxial growth.

Table 3. Typical deposition conditions for polycrystalline film growth of GST

Film thickness (nm)	Frequency (Hz)	Fluence (J/cm^2)	Ar-pressure (mbar)	Substrate temperature ($^{\circ}\text{C}$)
20-2000	1-10	0.5-1	$4 \cdot 10^{-5}$	~ 23

4.1.1. Initial growth investigations of pulsed laser deposited GST

In Figure 4-1, four different films are presented. The films were all deposited in the deposition chamber at room temperature and were confirmed to be amorphous in the as-deposited state. In Figure 4-1a, a 22 nm thick GST films deposited with a laser fluence of about $0.8 \text{ J}/\text{cm}^2$ is depicted. As can be seen, the surface is decorated with droplets of spherical appearance. The round shape stems from the fact that it is ejected molten material from the target surface that has propagated towards and collided with the surface. This is an inherent property of the laser ablation process and depends mainly on the laser energy deposited and the optical absorption in the target^[79]. Other investigations on PLD deposited GST films also mention the presence of particulates and droplets on the surface within an investigated fluence range between $1\text{-}3 \text{ J}/\text{cm}^2$, see Refs. 26,27,97,98. Unfortunately no SEM images are presented for easy comparison. The particulate density presented in this work lies around $10^4/\text{cm}^2$ for typical film thicknesses of 20-200 nm. This is

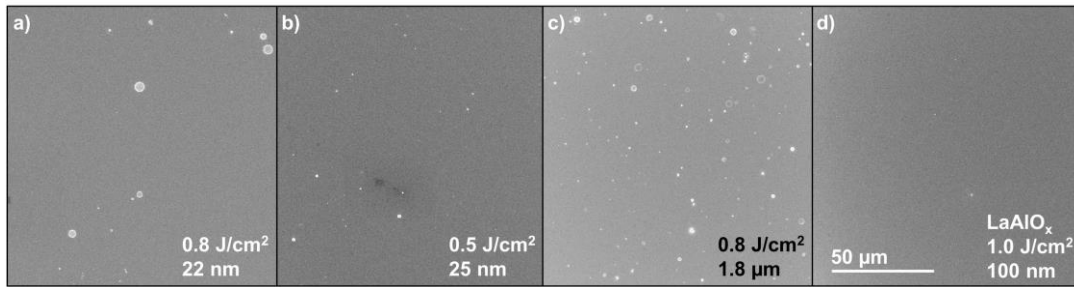


Figure 4-1. SEM images of as-deposited amorphous films. In (a)-(c), GST films are presented deposited under different conditions. In (d) a LaAlO_x film used as capping layer is presented.

independent of the laser fluence in the investigated range $0.5\text{--}1\text{ J/cm}^2$ and is evidenced in Figure 4-1b where a film deposited at 0.5 J/cm^2 is presented. No large difference compared to Figure 4-1a can be identified except that the particulates are somewhat smaller. This is just coincidence though and does not reflect any physical phenomena. However, the fluence range spans only a factor of 2 and it might not be enough to see any drastic effects. For a thicker film ($1.8\text{ }\mu\text{m}$) displayed in Figure 4-1c, the number of particulates on the surface increases. This illustrates the fact that the particulate density scales with the number of pulses used for deposition, since roughly 10 times more pulses were used in the deposition process and the particulate density is estimated to be $\sim 10^5/\text{cm}^2$. In Figure 4-1d, an amorphous film of LaAlO_x is depicted. This material was used as protective capping layer for GST as described later in this section. Virtually no particulates can be found on the surface of this material, presenting itself as a good candidate for protecting the GST surfaces.

The stoichiometry of the used GST ablation target was measured with two methods: X-ray Photoelectron Spectroscopy (XPS) and EDX as displayed in Figure 4-2. On the right

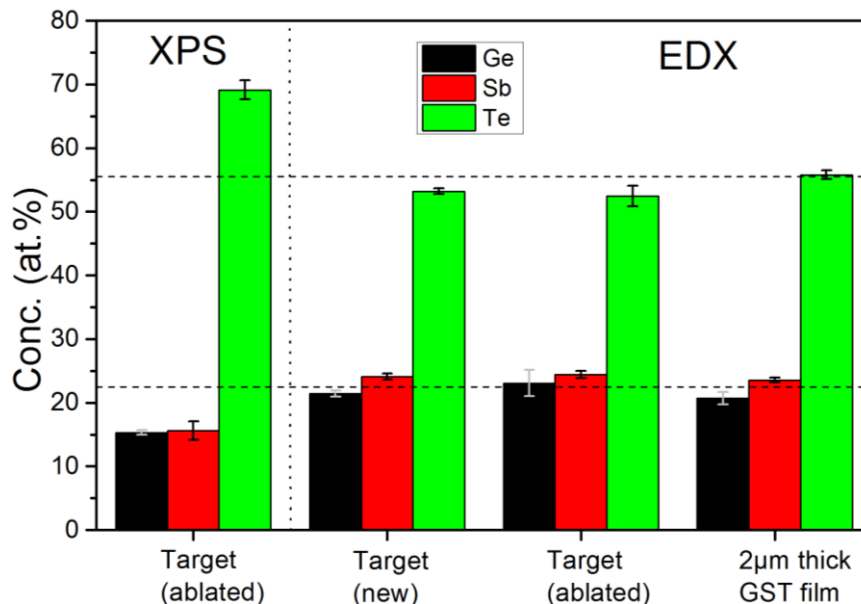


Figure 4-2. Comparison of the chemical composition obtained with XPS and EDX for the used GST target and a thick GST film. The dashed vertical line separated the XPS and EDX results, whereas the dashed horizontal lines mark the ideal GST225 composition.

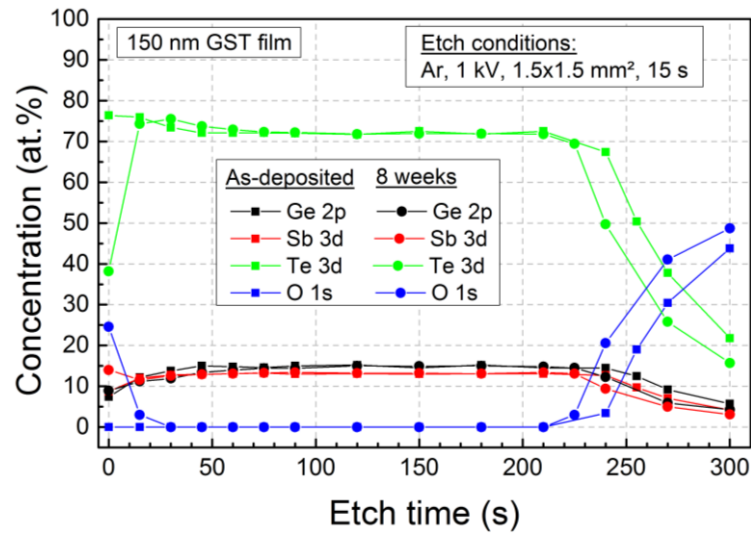


Figure 4-3. XPS sputter depth profiles of a 150 nm thick GST film in an as-deposited state as well as after 8 weeks storage under ambient conditions.

side of the vertical dotted line in Figure 4-2, the EDX data is presented. The target was measured both in the as-received state as well as after an initial ablation conditioning step (30000 pulses with 1 J/cm^2). Additionally, one deposited thick GST film is presented as comparison. A thick film was used, since this dramatically reduces the Si substrate signal and it is possible to measure the direct atomic concentrations. For all measured samples, no significant oxygen or carbon concentrations were found ($\sim 1\%$) and this contribution has been neglected in the diagram. Each investigated specimen was measured on at least four different spots, and the error bars symbolize the standard deviation from spot to spot. The target measures a small deficit in Te as compared to the ideal GST225 composition (dashed horizontal lines), both for the new and ablated state. Nevertheless, the composition is fairly close to GST225. For the thick GST film an almost matching stoichiometry is obtained. Only a small deficit (gain) in Ge (Sb) is seen. The result from a XPS measurement on the ablated target is presented on the left side of the dotted vertical line. A sputter depth profile was obtained and the presented values are the average values from >10 sputter steps with the error bars symbolizing the standard deviation. As can be seen, the relative atomic concentration of Ge and Sb matches the EDX measurements quite well. However, the absolute values are far off. This means that the sensitivity factors used for calculating the atomic concentrations are not valid for this material system without a re-calibration against a standard specimen of known exact stoichiometry. Hence, from here on chemical composition measurements were conducted with EDX.

Although the XPS measurements are not useful for composition determination of GST films, the method is highly reproducible and therefore it was used to obtain depth dependent composition information. Such a depth profile is displayed in Figure 4-3 for two measurement runs. An as-deposited GST film was directly transferred to the XPS chamber, with a total air exposure time less than 5 minutes and subsequently measured. The same film was then stored under ambient conditions and measured again after 1, 4 and 8 weeks. The result of the as-deposited and 8 week measurement is displayed in the diagram. As can be seen the samples only differ within the first 30 etch seconds (surface) and above

200 seconds (substrate interface), whereas in between they overlap well. The latter discrepancy can be explained by small differences in exact sputter removal between each step, while the former difference displays a surface oxidation. The picture looks the same for the measurement conducted after 1 and 4 weeks, i.e. after one sputter step the surface oxide is removed. This indicates a surface oxide thickness of less than 10 nm and that the oxidation eventually reaches a limit with a finite thickness.

The oxidation evolution was further confirmed by XRR measurements. In Figure 4-4 a GST films is displayed that was measured in the near as-deposited state (45 min after deposition) and at later times. The as-deposited film shows no direct indications of a surface oxide film, since the decay is monotonically exponential between 1 and 4° without any other wider oscillations visible. The extracted data however suggest a thin layer of 0.2 nm as presented in the inset table, but this value is definitely lower than the measurement uncertainty (± 1 nm). For the same film measured after 3 hours, a more pronounced surface oxide layer has formed. This can be seen as the wide oscillation with a maximum around 3.5°. This maximum is then shifted towards lower angles (around 2.2°) for the following two measurements, which indicates a slight increase of the surface layer thickness. However, no difference between the measurements after 8 hours and 24 hours can be discerned, confirming the saturation behavior as already observed from the sputter depth profiles in Figure 4-3. Simultaneously, a reduction in the oscillation amplitude is observed for the two films measured last, which indicates higher roughness in the films.

This oxidation evolution was one of the reasons why the films from this point on in general were coated with a thin LaAlO_x capping layer (10-15 nm). This deposition took place directly inside the PLD-chamber after GST growth so that the GST film surfaces never experienced any contact with ambient air. The second reason why a capping layer is beneficial is that it prevents desorption of GST film constituents at high annealing tempera-

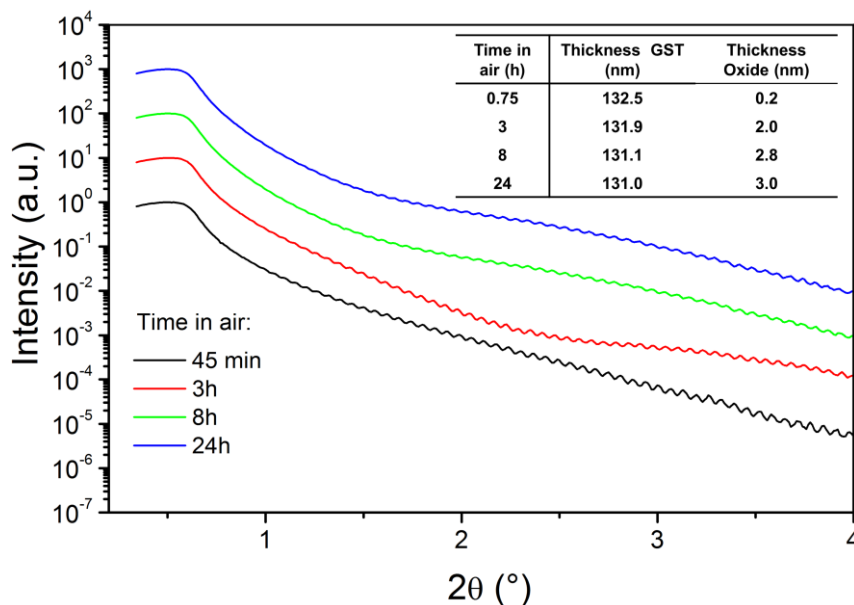


Figure 4-4. XRR measurements of a GST film measured in the as-deposited state (45 min) and after 3, 8 and 24 hours storage in air. The inset table show extracted data from the fit refinement. Each measurement has been offset with a factor of 10 in the y-direction for purposes of display clarity.

tures in the vacuum oven used for heat treatment, see section 3.2.1. However, to certify that no unwanted reactions take place between the GST films and the LaAlO_x capping layer a film structure was prepared with 86 nm thick GST and 15 nm thick LaAlO_x . Both layers were deposited at room temperature and the film was confirmed to be amorphous. A XRR measurement of the film prior to an annealing experiment was measured and is displayed in Figure 4-5 as the black curve. The film is smooth with low interfacial as well as surface roughness as evidenced from the inset table. The density is $5.6 \pm 0.1 \text{ g/cm}^3$ which is slightly lower than typical values for sputter deposited amorphous films ($5.8\text{-}6 \text{ g/cm}^3$)^[99,100]. After annealing the films at 200°C for 20 minutes ($10^\circ/\text{min}$ heating ramp) the density has increased to 6.2 g/cm^3 . This is better agreement with sputter deposited films for the metastable cubic phase^[100]. The density increase of about 8% is matched well by a thickness decrease of similar magnitude. Otherwise, no apparent changes of the film structure can be inferred from the XRR measurements, i.e. the capping layer has not reacted with the interface and can be thought of being inert. A further benefit from the capping layer is that the preparation of artifact free TEM specimens is facilitated, i.e. the films suffer less damage from the focused ion beam since the capping layer is on top.

To investigate the crystallization behavior of the GST films, annealing experiments in a vacuum oven were conducted (see section 3.2.1 for details). The GST films were protected with a capping layer that prevents desorption and loss of material in the films. Therefore a change in chemical composition is not expected and this was also confirmed by EDX (not shown here). The films were confirmed as-deposited amorphous as measured by XRD. After annealing 20- ω scans of the films were conducted and the results are presented in Figure 4-6. All films displayed in Figure 4-6 possess a film thickness between 50-200 nm and should therefore be comparable with each other. In order to obtain large crystallites (for HRTEM investigations), relatively long annealing times between 15-30 minutes at the desired temperature were chosen with a 10 K/min . heating ramp. This

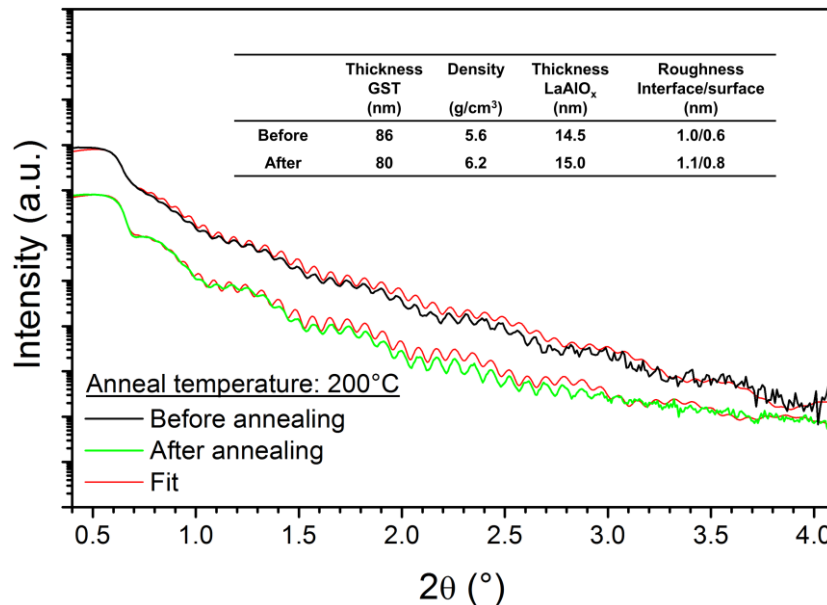


Figure 4-5. XRR measurements of a GST film measured before annealing at 200°C and after. The two measurements have been offset in the y-direction for display purposes.

resulted in quite sharp diffraction peaks with FWHMs of the Bragg peaks in the range between $0.2\text{-}0.4^\circ$. An estimate based on the Scherrer equation suggests corresponding crystallite sizes between 35-55 nm. The as-deposited film exhibits no diffraction peaks except those from the substrate. A broad intensity distribution is present between $2\theta \approx 25\text{-}30^\circ$, although it is not so easy to distinguish it in the waterfall plot. Nevertheless, it is a characteristic feature of the amorphous state of phase change films^[101,102]. The amorphous phase remains also at an annealing temperature of 150°C . However, a 15° degree temperature increase to 165°C produces intense Bragg peaks. This is a normal crystallization temperature for thin films of $\text{Ge}_2\text{Sb}_2\text{Te}_5$ ^[57]. The observed Bragg peaks coincide well with the phase reflection markers for the cubic GST phase^[62], annotated with black dashed lines in the figure. The patterns are qualitatively the same, i.e. a FCC structure, but a small peak shift to higher 2θ angles can be observed for the measured films. This is especially notable for high indexed diffraction peaks, i.e. (220), (311) and (222). The small shift indicates a slightly smaller unit cell than the model of Matsunaga^[62] (0.600 ± 0.001 nm instead of 0.603 nm), but it is in the range of other reported values^[47,58]. No qualitative difference can be found for the two films annealed at 180 and 200°C , i.e. they possess a FCC structure as well. At the next annealing temperature (250°C) a different appearance of the diffractogram can be discerned. Now, a peak appear at $2\theta \approx 20.5^\circ$ which is ascribed the GST225(0004) reflection. Moreover, only peaks that can be indexed with (000 l) reflections are found. This also includes the small peak at roughly 42° which can be ascribed the GST225(0008) reflection, but for clarity reason this particular annotation has been excluded in the figure. The peaks observed do not fit the pattern exactly, some peaks are shifted to lower diffraction angles and some to higher. This makes it hard to draw any conclusion on the exact hexagonal phase. Nevertheless, the film possesses a clear fiber texture along the [0001] direction. This means that the basal hexagonal plane is aligned with the substrate surface. This is surprising since an annealing procedure should promote random polycrystalline growth. A similar behavior has been found, though, on crystalline substrates with (111) orientation^[103]. In that work, the authors also noticed the same out-of-plane orientation as observed here with a defined additional in-plane orientation. It was proposed that the nucleation starts at the substrate-film interface instead of randomly oriented nuclei in the bulk film. Since hexagonal GST phases consist of stacked vacancy layers, the most energetic alternative is to align the vacancy layers parallel with the substrate surface. It should be noted, however, that only this one single film has shown such a pronounced texture for annealed films on amorphous substrates. This is obvious, when regarding the two films annealed at the highest temperatures. Here, a multitude of Bragg peaks are visible. The angular peak positions are in general in good agreement with the hexagonal phase reflection markers, confirming that the hexagonal GST225 phase was obtained. Interestingly, for these two films the same preferential crystal orientation is found, although not so pronounced. This can be seen from the fact that the (0005) reflection is the strongest one, but in a random polycrystalline film the (10-13) peak should scatter the most (see section 2.2.4).

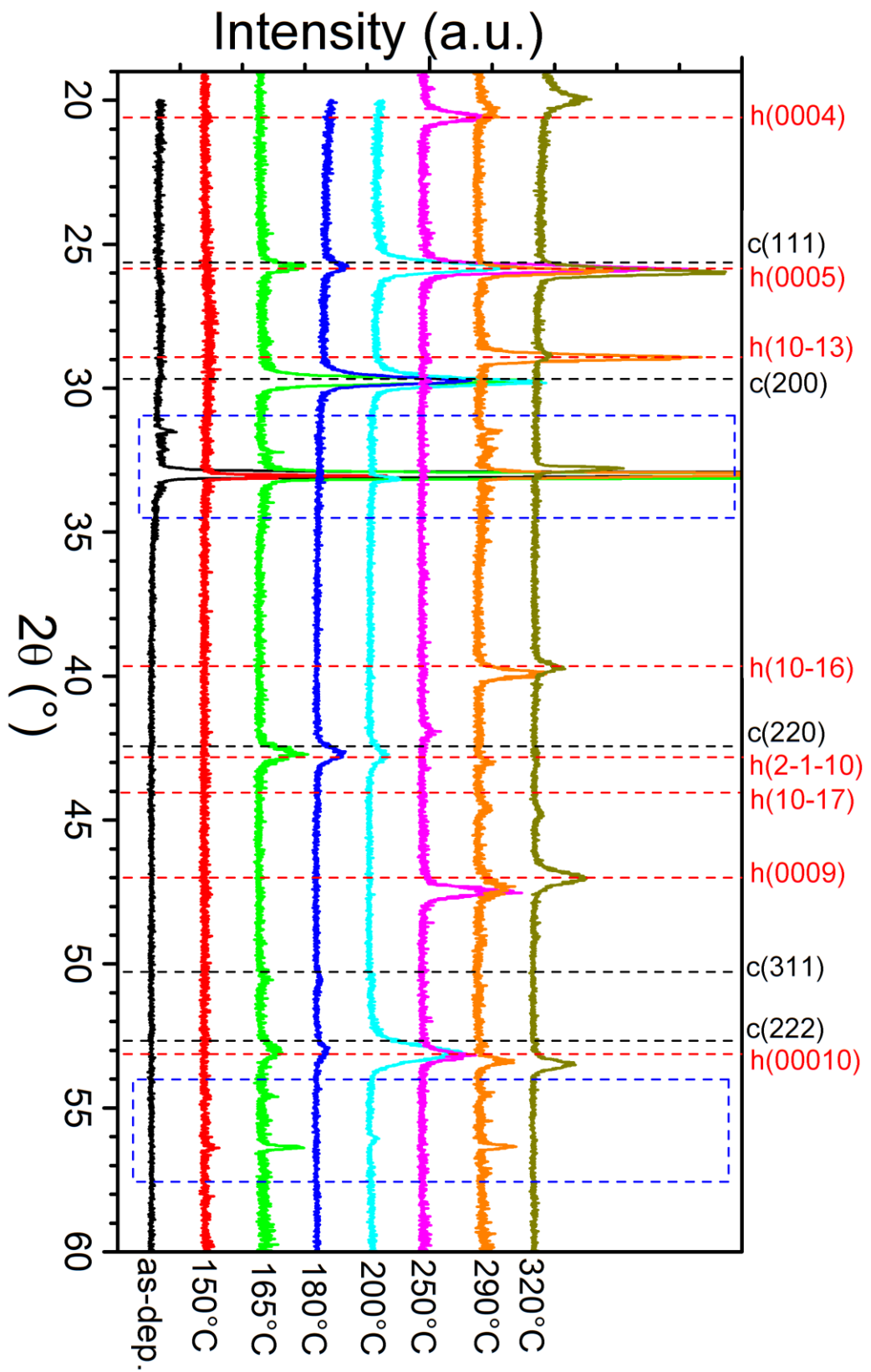


Figure 4-6. 2θ - ω scans of GST films annealed at different temperatures. Reflections of the GST1225 cubic phase are marked in black and hexagonal phase reflections in red. Diffraction peaks inside the two blue dashed boxes stem from the substrate. Reflection positions for the cubic and hexagonal phases are annotated with black and red dashed lines, respectively.

The fact that the films were annealed for a long time with resulting large crystallites opened up for the possibility to obtain direct images of the lattice using HRSTEM. The TEM specimens were prepared with extreme care in order to avoid introduction of artefacts and damage to the films^[93]. In Figure 4-7, HAADF-STEM images from two films that were annealed at 200 and 320°C are displayed in a) and b), respectively. Diffraction patterns ((NBD) and (SAD)) were obtained to confirm the crystalline structures as observed in Figure 4-6. The patterns were recorded in TEM mode, but the corresponding TEM images are not shown. The film annealed at 200°C was confirmed cubic from the NBD pattern shown on top of the image as viewed along the [110] direction. A HAADF-STEM image, viewed along the [110] direction, would reveal two sets of (111) planes for a cubic crystal. These planes are inclined towards each other with 70.56° in a perfect FCC crystal. This is the situation in Figure 4-7a, where a HAADF-STEM image of the cubic film is shown along the [110]. Two sets of (111) planes decorate the image in a regular way as indicated by the white dashed lines. Since the heaviest atoms in HAADF-STEM mode scatter most, it can be concluded that the (111) planes are occupied by Te atoms. This is in good agreement with theoretical crystal structures of GST225^[47,62]. The angle between the planes measures $70.3 \pm 0.1^\circ$, almost in agreement with the FCC structure. The fact that it does not match the theoretical angle exactly could be an indication that the films are subjected to a small rhombohedral distortion (see section 2.2.2 for details). Such a distur-

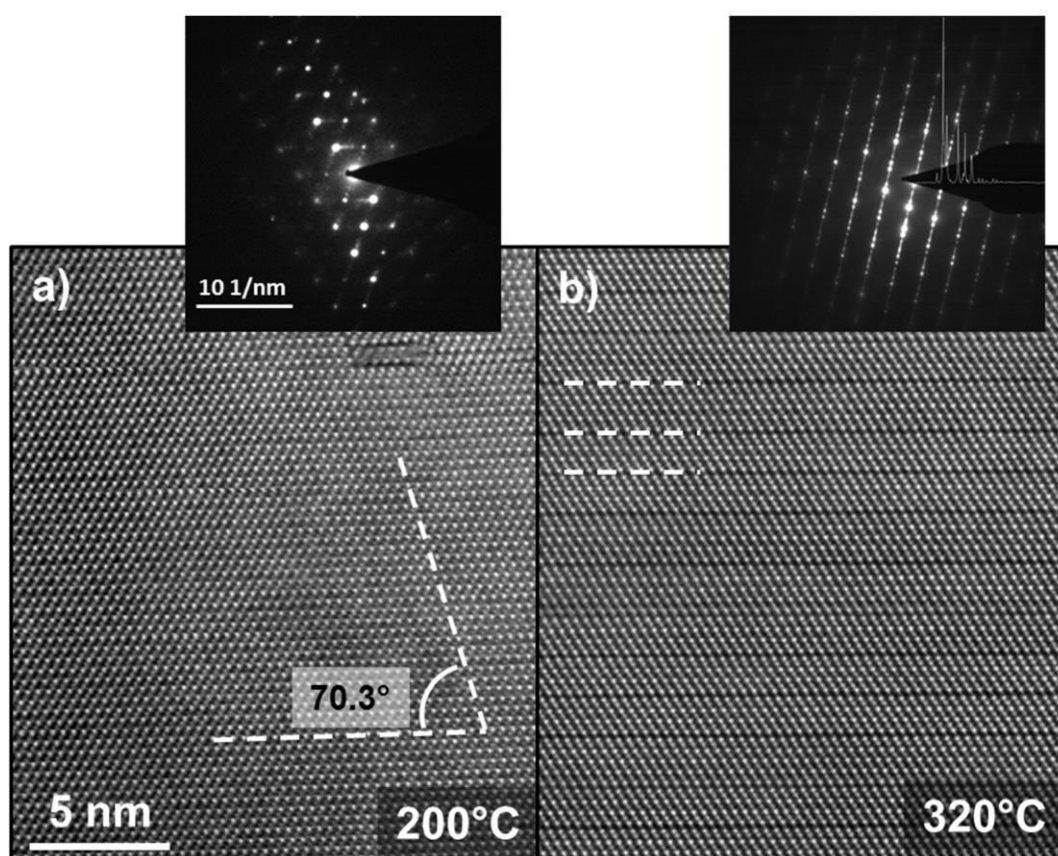


Figure 4-7. HAADF-STEM images of a cubic (a) and a hexagonal (b) GST film. The diffraction patterns attached to (a) and (b) were obtained with NBD and SAD, respectively (see text). The white dashed lines in (a) and (b) annotates (111) planes and vacancy layers, respectively. The scale bars in (a) also applies for (b).

tion has been proposed by Kolobov et al^[34,104]. The distortions are, however, so small that they are not observed in polycrystalline films measured by XRD. In the top part of the figure an even more distorted region is visible. However, it is believed that these distortions were induced by the focused ion beam process and are not to be considered as real defects in the crystal structure. In the SAD pattern on top of Figure 4-7b, a hexagonal pattern from a film annealed at 320°C is revealed as viewed along the [1-2-10] direction in hexagonal GST225. The diffraction spots coincide well with that of the theoretical model^[62]. Additionally, all spots lie centered on almost vertical lines running from the top right part down to the bottom left in the SAD image. This is the [0001] direction in the crystal. Since the spot pattern does not deviate from this orientation, a very small (not measurable) crystallite tilt distribution must be present in the film. This implies that just by chance only one large crystallite contributes to the SAD pattern, although the diffractogram in Figure 4-6 suggests that more-or-less randomly oriented crystallites with a size of about 40-50 nm are present in the film. This just reflects the spatial difference between the two diffraction measurement methods, i.e. XRD measures a macroscopic average over the whole film, whereas TEM provides extremely local microscopic information. In the HAADF-STEM image (Figure 4-7b), a completely different microstructure as compared with the cubic case is displayed. Clearly, dark horizontal lines extend over the whole image side. These are identified as vacancy layers (VL). For clarity, three of them are annotated with dashed white lines. Each VL is separated by rows of bright spots. These are identified as Te atoms and in general 4-5 rows are inserted in between each VL. In a perfect GST225 single crystal the VL spacing should amount to 5 Te rows^[62]. The slight deviation seen herein, could be attributed to differences in local chemical composition as already observed by Kooi and De Hosson^[64].

All in all, the annealing experiments show that PLD-deposited thin films behave in a similar way as those produced with sputtering^[57] with respect to crystallization temperature and crystal structure.

4.1.2. Polycrystalline film growth of GST at elevated substrate temperatures

Up to this point all GST films described in this study have been deposited at room temperature and were subsequently annealed in an oven to obtain crystalline materials. This is also the standard way to produce GST films (i.e. amorphous as-deposited), since much of the interest in these material lies in studying the crystallization behavior upon external stimuli. However, from a fundamental point of view the crystallization behavior at elevated deposition temperatures is also of interest, since the deposition for many PVD-methods often takes places under non-thermodynamic equilibrium conditions. Sb_2Te_3 , being one of the binary compounds in $\text{Ge}_2\text{Sb}_2\text{Te}_5$, is known to grow with a preferred c-axis orientation both on amorphous and crystalline substrates^[105,106]. The other binary compound (GeTe) is also known to grow preferably in the pseudo-cubic [111] direction when providing single crystalline substrates^[107,108], i.e. both binary compounds prefer to align the trigonal symmetry planes ((0001) and (111)) with the substrate surface. It is not surprising then, that superlattices of the two compounds also grow preferably with the trigonal symmetry planes parallel to the substrate surface^[20]. Not many studies have been conducted on the growth of GST at elevated temperatures though. In fact, no investiga-

tions at all on the GST growth at elevated temperatures on amorphous substrates have been found by the author. Shayduk and Braun^[21] and Perumal^[69] investigated the growth of GST on single crystal substrates with Molecular Beam Epitaxy (MBE). Both reported on an amorphous growth stage at low substrate temperatures (<100-120°C) whereas polycrystalline films with complete random orientation are found at higher substrate temperatures (<160-180°C). No evidences of a preferred orientation in the polycrystalline films have been presented. In Figure 4-8, 2 θ - ω scans of GST films deposited at different substrate temperatures are presented. For comparison, one film that was deposited at room temperature and subsequently annealed at 290°C is displayed. For the films deposited at room temperature (RT) up to 110°C, no diffraction peaks are discernable, i.e. the films are amorphous. Above, 110°C, a diffraction peak is starting to emerge at the position of the (111) and (0005) reflection marker. This temperature range is in good agreement with that of Shayduk and Braun^[21] and Perumal^[69]. The peak grows in intensity up to 175°C and thereafter it starts to decrease again and actually vanishes for the film deposited at 290°C (loss of film material during growth). Below 175°C the films are either cubic or hexagonal or possibly a mixture of both. The uncertainty in determining the crystalline phase lies in the absence of intensity at the (0004) reflection position at these temperatures. The absence of this peak could imply that the films are cubic, but it might as well just be buried in the background as a consequence of the low scattered total intensity. At 175°C or above, however, the films are hexagonal as seen from the weak intensity distribution at the (0004) reflection marker. The films do not display any temperature dependent peak shift, with the exception of the film deposited at 240°C. In this film the (0005) peak is shifted to slightly larger diffraction angles, an indication of a transition to the GST124 phase. That such transitions are possible will be elucidated further in section 4.4.1, Figure 4-52. In all crystalline films there is a clear preferred orientation since only

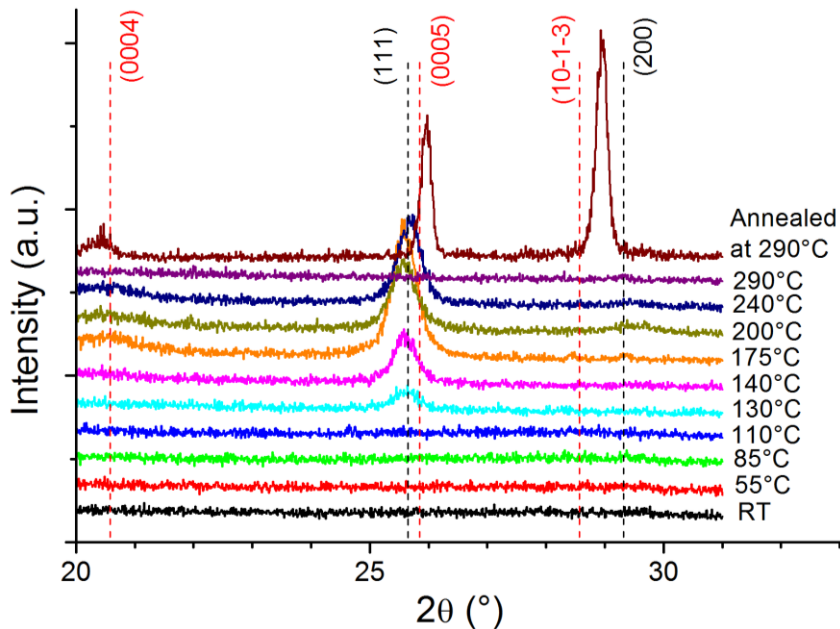


Figure 4-8. 2 θ - ω scans of GST films deposited on amorphous substrates at different temperatures. For comparison, also an *ex-situ* annealed film is displayed. Reflections of the GST225 cubic phase are marked in black and hexagonal phase reflections in red.

(111) or (000 λ) reflections can be seen. This is especially obvious when comparing with the annealed film in the top of the graph. Clearly, the (10-13) peak is the strongest one, whereas this peak is totally absent for the films deposited at elevated temperature. This shows that the degree of texturing is high with a [0001] fiber axis. Another striking difference is the FWHM of the diffraction peaks. In the annealed sample it is around 0.25-0.3°, whereas the films deposited at elevated temperatures show roughly the double value. This is a good indication that the crystallization of the films proceeds in a three-dimensional (3D)-growth mode. The position of the main diffraction peak at $\sim 25.6^\circ$ does not coincide exactly with any experimentally observed GST phase. This is not so surprising though, since also a discrepancy was seen for the polycrystalline annealed GST films, see section 4.1.1. Irrespective of the exact GST phase being present, all films grow with a hexagonal symmetry plane (either a (111) or a (0001) plane) parallel to the substrate surface with a clear fiber axis (either [111] or [0001]). This behavior has not been observed earlier on amorphous substrates for GST according to the authors' best knowledge.

In Figure 4-9, the film thickness dependence on substrate temperature of the same set of films as measured with XRR is visualized. The nominal film thickness for the amorphous films (deposition temperature $\leq 110^\circ\text{C}$) is 50 ± 3 nm. At 130°C , where the first diffraction peak was visible, the film thickness is reduced a bit. The reduction corresponds to a film thickness decrease of about 10% which is slightly more than the typical value of 6% when going from an amorphous to crystalline phase^[99]. The discrepancy could, however, be related to additional loss of material, since the deposition takes place in vacuum and at non-ambient temperature. Indeed, the film thickness continues to decrease with an increase in substrate temperature. This clear decrease cannot be explained just by a densification of the amorphous phase, but simultaneously also desorption of the film constituents must take place. Such a desorption behavior is known from epitaxial films of phase change materials deposited with MBE^[23,108], although the absolute substrate temperature range where desorption sets in, varies somewhat. The effect of desorption is clear for the

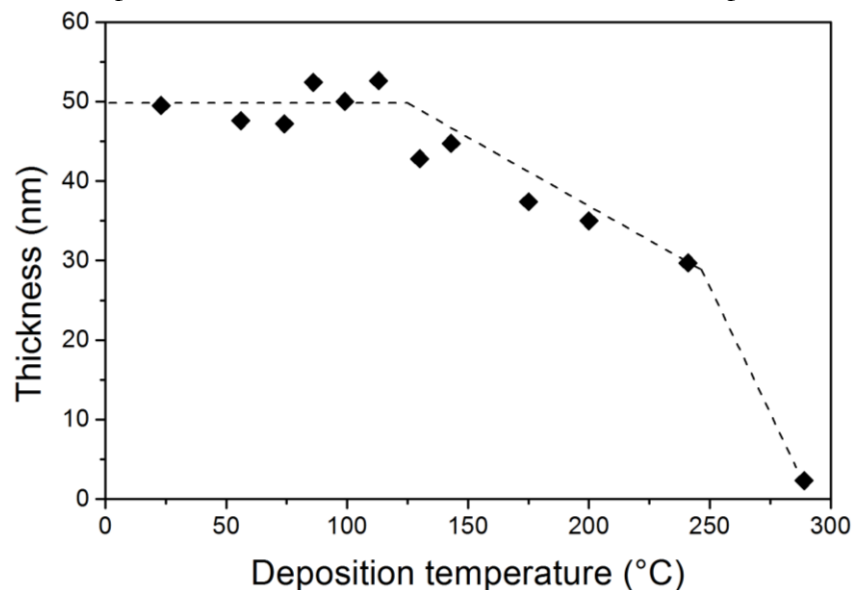


Figure 4-9. Substrate temperature dependence on film thickness as measured with XRR for GST films deposited on amorphous substrates.

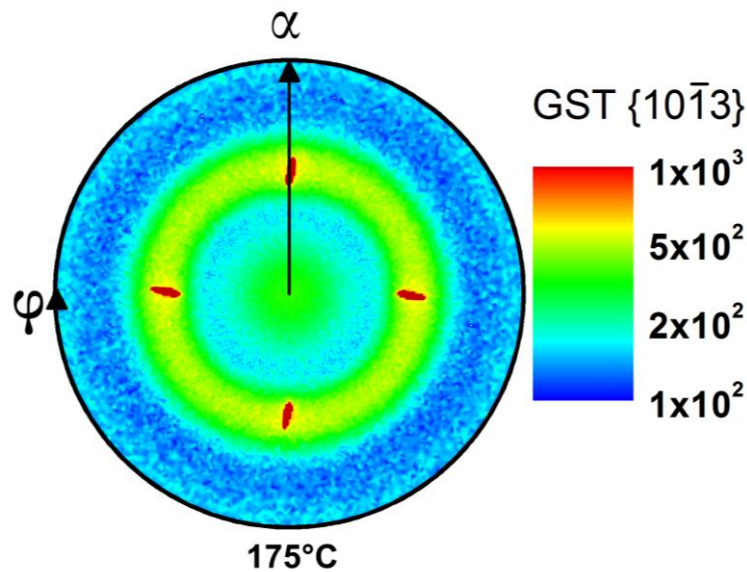


Figure 4-10. Measured pole figure of the GST{10-13} reflection for a film deposited at 175°C on a Si(100) substrate with native oxide still present. Intensity (cps) is presented on a logarithmic scale.

film deposited at 290°C where barely no material is left after deposition. This also explains in a convincing way why no diffracted intensity was seen in Figure 4-8 for this particular film.

To evidence the texture component in the films, pole figure measurements of the hexagonal GST{10-13} was carried out. In order to gain as much intensity as possible from the weakly scattering films, a slit combination was used that maximizes the intensity from the film. As a consequence, the substrate contribution cannot be displayed in a correct way anymore, i.e. a small distortion is present in the substrate pole density maxima. In Figure 4-10, a pole figure of a GST film deposited at 175°C is displayed. The pole figure is dominated by a ring shaped intensity distribution which has its intensity maximum at $\alpha \approx 57.5^\circ$. This is in good agreement with the hexagonal GST225 and GST124 phase which possess inclination angles of $\sim 58^\circ$ with the (0001) planes and indicates a clear [0001] fiber texture. However, a weaker pole density maximum is also observed in the center of the pole figure, which means that the film also contains a small portion of (10-13) planes oriented parallel to the substrate surface. Although the films almost exclusively align the hexagonal basal plane parallel with the substrate surface, the rocking curves of the (0005) peak in the films measures 10-20° in FWHM (not shown here). This is not especially narrow, even for polycrystalline textured films. However, just the fact that the films grow with a preferred orientation on amorphous substrates is a good indication that even higher ordered films can be obtained when using crystalline substrates. That will be the focus of the upcoming three main sections.

4.1.3. Summary of the results on the deposition of polycrystalline and amorphous GST

In this section initial investigations on the growth of GST with PLD were presented. The GST films are deposited in an amorphous state at room temperature and show expected

crystallization temperatures for the two crystalline phases ($\sim 150^\circ\text{C}$ and $\sim 250^\circ\text{C}$). The composition in the target is transferred well to the films with an almost ideal GST225 stoichiometry.

Depositing the films at elevated substrate temperatures ($> 130^\circ\text{C}$) produces textured crystalline films. The crystalline phase is either cubic or hexagonal at temperatures below 150°C , whereas the hexagonal phase forms at temperatures above 150°C . The preferred growth orientation is along the $[111]$ or $[0001]$ direction for cubic and hexagonal phases, respectively. In other words, the GST films prefer to align hexagonal close-packed planes parallel with the substrate surface.

4.2. Epitaxial growth of GST on KCl(100)

In this section the results of the GST deposition on freshly cleaved KCl(100) will be presented. Three experimental parameters, i.e. substrate temperature, deposition rate and film thickness were varied systematically. The experimental parameters in common for the films are presented in the following table. Deviations from these parameters will be stated when called for.

Table 4. General deposition conditions on the growth of GST on KCl(100)

No. of pulses	Frequency (Hz)	Fluence (J/cm^2)	Ar-pressure (mbar)	Pre-heating at substr. temperature (min)	Capping layer LaAlO_x (nm)
4000	2	0.8	$4 \cdot 10^{-5}$	>30	~10-15

4.2.1. The effect of substrate temperature on the growth of GST on KCl(100)

Thin films of GST were deposited on KCl(100) at several different temperatures with a deposition rate of ~ 5 nm/min. To investigate the compositional temperature dependence the samples were analyzed with EDX. In Figure 4-11 the results are presented as atomic ratios. In the very left part of the figure the ideal 2:2:5 composition is displayed as well as the target starting composition. The composition of the films remains largely constant in the temperature range up to 300°C with only a slight relative increase of Ge and Sb. Above 300°C a drastic change in the composition can be observed. Obviously a partial loss of Ge and Te has taken place. Such a desorption behavior is known from the deposition of epitaxial GST films by MBE, although at somewhat lower temperatures of around

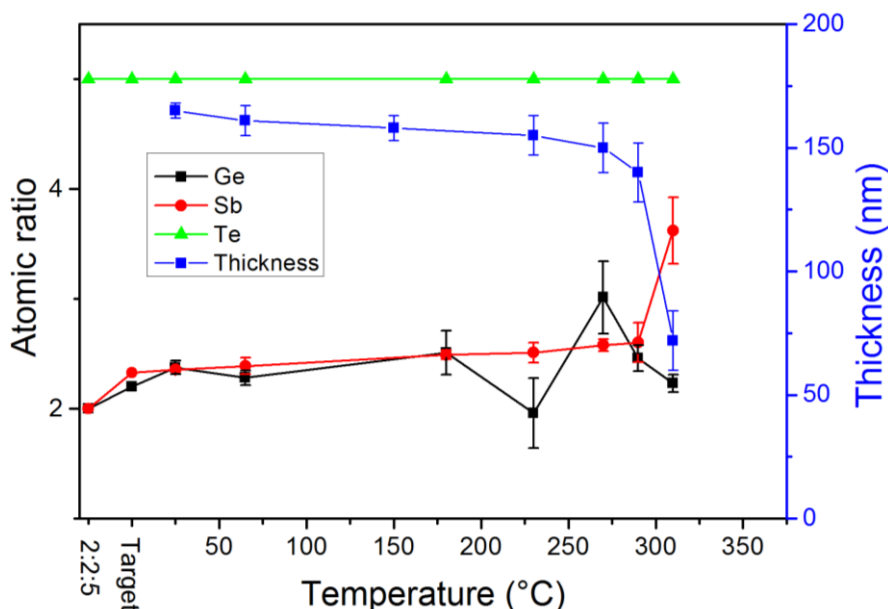


Figure 4-11. Chemical composition and thickness of deposited GST films as a function of substrate temperature as determined by EDX and SEM cross-sections. The Te concentration is in all cases set to 5 for comparable values. The ideal theoretical composition 2:2:5 as well as the composition of the PLD target are included on the left in the graph.

200-250°C^[23,109]. This is a first indication that the process temperature window is different for PLD-deposited films compared to those deposited with MBE and can be understood by regarding the actual growth process. In MBE, the constituent species arrive at the target in elemental form and competing processes may occur at the substrate surface, i.e., surface diffusion, nucleation, or desorption. In PLD, the same processes can occur at the surface. However, some significant differences exist: First, the particle flux does not only consist of elemental species, but molecular residues and clusters arising from the molecular structure of the target are also present which could have different vapor pressures compared to the raw elemental components^[97]. Second, the deposition takes place in a background gas environment instead of UHV which, additionally, reduces the vapor pressure of the constituents. These important differences show that PLD can significantly modify the process window for deposition. The blue curve in Figure 4-11 displays the film thickness dependence of substrate temperature as measured by cross-sectional SEM images and it agrees well with EDX measurements. A relatively constant thickness up to a temperature of 300°C can be seen where desorption sets in rapidly.

To evaluate the crystalline content in the films, 2θ - ω and rocking curve measurements were conducted and the results are presented in Figure 4-12. Films deposited below 140°C are characterized by an amorphous state, whereas films deposited in the temperature range between 140-200°C show a polycrystalline textured growth similar to the films shown in Figure 4-8 with intensities of a few hundred counts per second (cps) (not shown here). This further illustrates the observation that PLD-deposited GST-films prefer to grow in a hexagonal structure with a clear fiber axis along the [0001] direction as long as a flat substrate is provided. Between 200-270°C the growth mode changes drastically. Still, a hexagonal phase is formed, but suddenly intensities of up to two orders of magnitude larger are registered. This can be seen in Figure 4-12a where two peaks at $\sim 20.4^\circ$ and 25.6° appear. The peak at $\sim 20.4^\circ$ shows that these films are hexagonal since this peak would not occur for a FCC structure. However, the exact hexagonal phase cannot be determined from these measurements, as all hexagonal phases discussed previously in section 2.2 i.e.

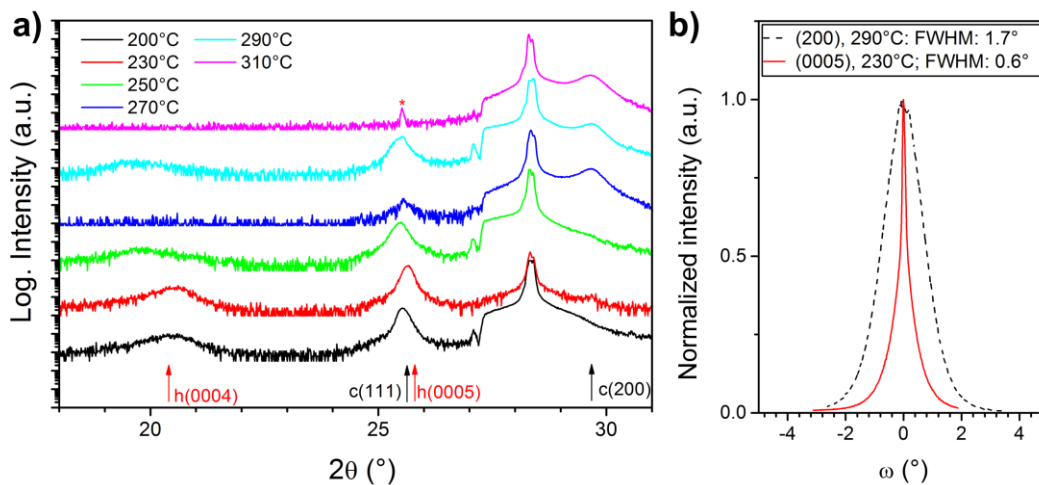


Figure 4-12. 2θ - ω scans for GST films deposited at different temperatures (a). Hexagonal positions are marked with red and cubic ones with black. In (b) the rocking curve for two samples deposited at 230°C and 290°C are presented.

GST124, GST225 or a layered cubic structure agree to a certain degree. This problem will be further discussed together with pole figure measurements illustrated on page 49. Irrespective of the exact hexagonal phase, all (000 l) planes are weakly scattering planes, and therefore the intensities obtained are indeed a strong indication that the films grow in an ordered way. As mentioned above, these planes are of hexagonal in-plane symmetry and no obvious epitaxial relationship exists between the cubic substrate and these planes. Although such an epitaxial orientation is unexpected, it has been observed in MBE-deposited epitaxial GST films on (100) oriented substrates^[24,110,111], where a cubic (111) orientation (also of hexagonal in-plane symmetry) coexists with a cube-on-cube orientation. The c-axis length is calculated from the peak at $\sim 25.6^\circ$ and assuming a GST225 phase it would correspond to values in the range of 1.74-1.76 nm, slightly larger than that suggested by Matsunaga^[62] and Urban et al.^[65]. Above 270°C diffraction peaks belonging to the cubic GST(200) planes can be discerned. This is a clear indication that only with enough deposited energy the GST films can conform to the cubic substrate symmetry. The hexagonal phase persists, however, also in this temperature range. Only for the sample deposited at 310°C no evidence of a hexagonal phase can be found. The FWHM of the dominating 2 θ peaks are broad, around 0.2° and 0.4° for (0001) oriented and (100) oriented films, respectively. This means that the films consist of a multitude of small crystallites which in turn indicates a 3-D growth mode. However, the crystallites are well aligned along the growth axis as the ω -scans presented in Figure 4-12b reveal. The FWHM values are typical for films with the corresponding dominating orientation. Clearly, the (0005) peak exhibits a much more narrow distribution than the (200) peak. This once more confirms that the films prefer to grow (0001) oriented and it is concluded that at lower temperature a hexagonal phase dominates the growth, whereas the cubic phase dominates at higher temperatures^[112].

To investigate the topography of the films, SEM images were acquired. In Figure 4-13a and b, two films with dominating hexagonal structure are displayed. The images were taken with a 50° tilt angle to enhance topography contrast. The films bulge out from the surface and local delamination has taken place. This reflects the difficulty in aligning a hexagonal symmetry plane with a cubic substrate and obviously the substrate adhesion is not large enough to compensate for this stress. However, in between the bulges the films are rather smooth with no distinct surface features. This is definitely not the case for the (100) oriented films deposited at higher temperatures. For these films no signs of delamination have been observed. Instead, a rectangular fishbone pattern of crystallites appears at slightly higher magnification. Such a pattern is displayed in Figure 4-13c for a film deposited at 290°C. Plate-like crystallites are aligned according to two main directions separated by 90° azimuthally. This is the case for all samples with a dominating (100) orientation and it will be further elucidated by AFM investigations presented on page 47. In Figure 4-13d and e, cross-sections of (0001) and (100) oriented films are shown, respectively. Once again, the delamination can be clearly discerned in d) with an otherwise featureless film cross-section. The film deposited at 290°C on the other hand displays several large crystallites, a general feature of the (100) oriented films. In order to minimize sample drift and charging effects the films were coated with 10-15 nm Al and this manifests itself

as small crystallites covering the whole sample and is not related to the film growth process. This is especially noticeable in Figure 4-13e.

To gain further insights on the topography, AFM investigations were carried out. All samples were positioned with the substrate edges parallel with the image sides, i.e. the (010) planes are parallel with the image side $\pm 2^\circ$. Therefore, any special lateral orientations of crystallites can be directly related to and compared with the cubic (100) planes. In Figure 4-14a-c are displayed, a pristine KCl(100) substrate, a film deposited at 230°C with dominating (0005) orientation and a film deposited at 290°C with dominating (100) orientation. The pristine substrate exhibits several hundreds of nanometers wide cleavage terraces separated by in general a monoatomic step, translating into a miscut angle of around 0.1° with the (100) plane. Additionally, the terraces do not run perfect along a straight line indicating a small miscut also with the (010) and (001) planes. On top of the terraces the surface is atomically smooth, acting as good initial surface for epitaxial growth. The sample deposited at 230°C (see Figure 4-14b) was measured on a non-delaminated area and it shows a smooth surface with no apparent surface features. The thin capping layer deposited as protection could obscure some very small and low surface features but it is not believed to be the case. The rms value amounts to 0.4 nm which is comparable to that of as-deposited amorphous films. The film deposited at 290°C (see Figure 4-14c) possesses a much higher rms value (1.8 nm). This is obvious upon closer inspection of the surface. The fishbone pattern already observed in the SEM images (see Figure 4-13) can also be discerned here. The crystallites are arranged according to two principal directions which are separated by 90° azimuthally, with one of the directions rotated 45° with respect to the substrate edge. This is illustrated by the two solid white lines in Figure 4-14c. Since the KCl(100) planes are aligned with the image side it is impossible that the crystallites observed in the AFM image belong to (100) oriented GST crystal-

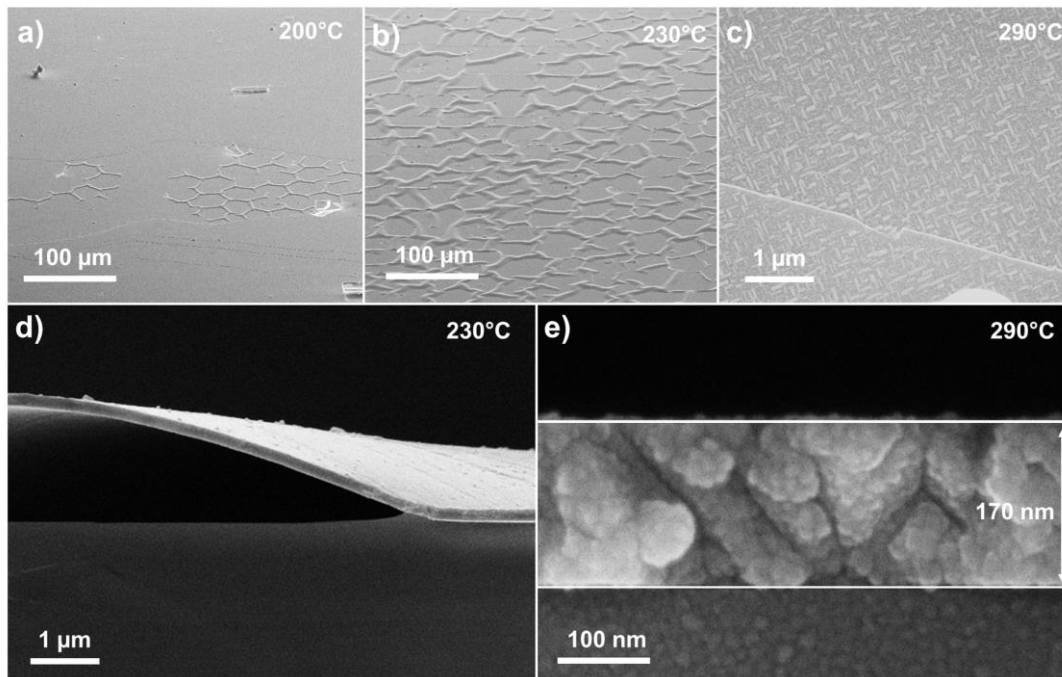


Figure 4-13. SEM images of GST films on KCl(100) deposited at a) 200°C , b) 230°C and c) 290°C . In d) and e) cross sections of films deposited at 230°C and 290°C are depicted, respectively.

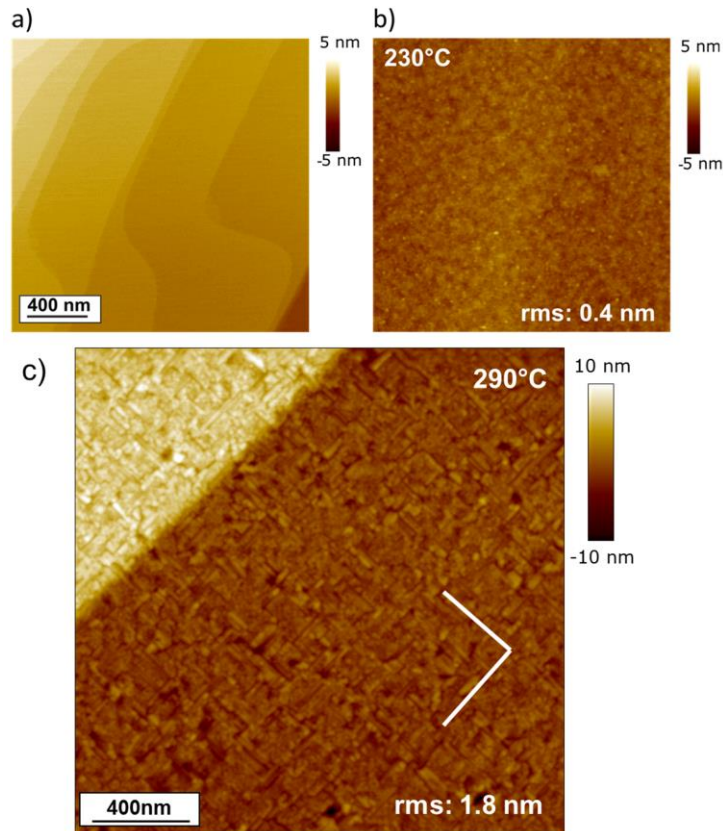


Figure 4-14. AFM images of the topography for (a) a pristine KCl (100) substrate, (b) an epitaxial (0001) oriented GST film deposited at 230 °C and (c) an epitaxial (100) oriented GST film deposited at 290°C. All films have a nominal thickness of 170 nm. The white lines in c) indicate the dominant crystallite orientations. The measured rms value is given in each figure. The scale bar in (a) is representative also for b).

lites as they would conform to a cube-on-cube orientation. This argument only holds, of course, for epitaxial films which at this point has not actually yet been proved.

To verify, if the films indeed grow with an epitaxial relationship, in-plane XRD measurements were carried out. An in-plane $2\theta\chi\text{-}\varphi$ gives evidence of the lateral lattice constant in the films, since it measures the vertically oriented crystal planes. In Figure 4-15, two films are presented, one of (0005) orientation (red) and one of (100) orientation (black). As displayed in Figure 4-15a, diffracted intensity can be observed at the angular position of the (004) planes of KCl and GST for the black curve which are perpendicular planes to the (100) plane. The arrows mark the theoretical positions of KCl and cubic GST^[62] and the peak positions coincide well with those. This gives evidence that the films are relaxed. For the (0001) dominated film (red curve), instead a peak at 42.48° is present which can be correlated to a GST(2-1-10) plane, being a perpendicular plane to (0001). The value coincides well with the theoretical position (42.40°) of the cubic layered structure, see section 2.2.4. In-plane φ -scans of the peaks are presented in Figure 4-15 and they resolve the underlying symmetry in the films clearly. The black curve shows 4 peaks azimuthally separated by 90° which corresponds to a cube-on-cube orientational relationship. The red curve shows 12 peaks azimuthally separated by 30° which suggests a $4*3$ -fold symmetry. This is the first evidence that the films grow epitaxial, but to completely deter-

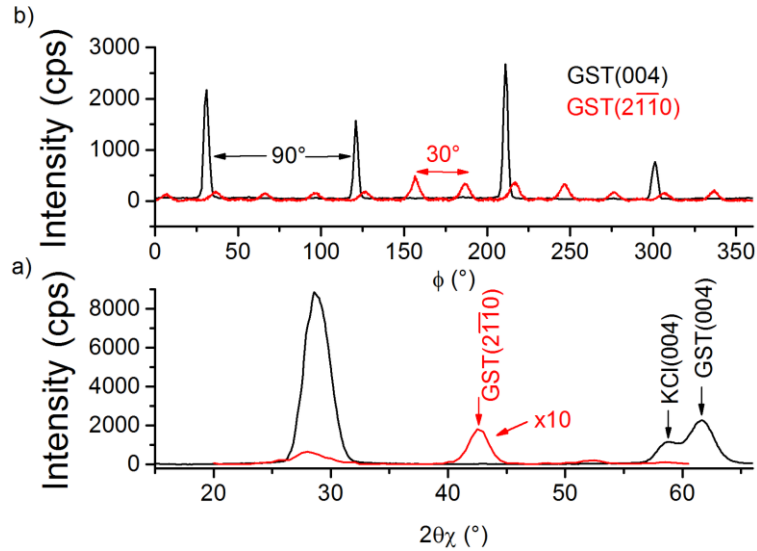


Figure 4-15. In-plane $2\theta\chi$ - ϕ measurements in a) for GST films deposited at 230°C and 290°C. In b) in-plane ϕ -scans of the GST(004) and GST(2-1-10) peaks are shown for the same samples.

mine the epitaxial relationship between the films and the substrate, it is needed also to measure the substrate orientation.

This can be obtained with pole figures measurements. Pole figure measurements can, additionally, reveal misalignments in the films and present unknown orientations of crystallites. For this purpose, pole figures of the cubic GST{200} planes were recorded. It should be noted that the GST225{10-13}, GST124{10-17} and cubic layered GST225{10-110} planes were simultaneously recorded, since the angular separation in 2θ is only 0.6° or less. Thus, all those planes contributed to the intensity distribution in the pole figure. The GST{200} planes (and the respective hexagonal planes) were chosen, because they are the strongest scattering planes for the respective crystal structure. That way, the chance of resolving weakly scattering features is highest. The results from a few selected films are presented in Figure 4-16. The films with a dominating (0001) orientation (Figure 4-16a and b) show a ring, which indicates a fiber texture. The ring intensity is in both cases modulated with 12 maxima, whereby this is especially clear for the sample deposited at 230°C. This is good evidence that the (0001) orientation adapts to the cubic substrate with a certain orientation. The tilt angle α is found to be $55 \pm 1^\circ$. To clarify this relationship, computer models of different hexagonal phases and orientations were calculated^[75] and the best match is displayed in Figure 4-16c. The model that describes the peaks best is the layered cubic model. In this structure the {10-110} planes are inclined towards the (0001) plane with 54.74° , in good agreement with the measured pole figures. The hexagonal 225 and 124 phases possess inclination angles of 57.8° and 58.2° between the (0001) and the corresponding (10-1 l) planes. It is further deduced that the (0001) oriented films consist of 4 rotational domains, each separated by 90° azimuthally, with one of the domains having the GST[1-210] direction rotated 15° with respect to KCl[010]. One of these rotational domains is marked in red in the figure. Group theory predictions on epitaxial layers of hexagonal symmetry on top of rock salt (100) substrates agree well with this observation^[113]. This suggests that a layered cubic phase forms at low temperatures as proposed by da Silva et al.^[66]. In Figure 4-16d and e, films are presented that were

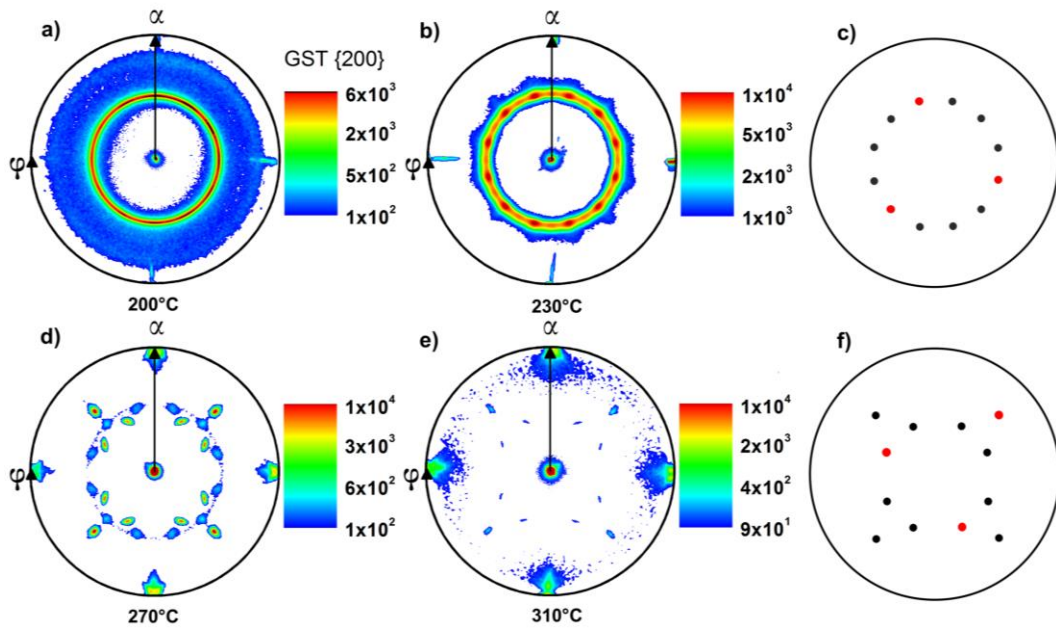


Figure 4-16. Measured pole figures of the GST{200} planes for films deposited at a) 200°C, b) 230°C, d) 270°C and e) 310°C. The modeled pole figures in c) and f) show 4 different (0001) domains separated azimuthally by 90° and 4 different (221) domains separated azimuthally by 90°, respectively. In each of the models one rotational domain is emphasized with red color. Intensity (cps) is shown on a logarithmic scale.

deposited at 270 and 310°C, respectively. This is the temperature regime where the cubic (100) orientation dominates the growth. This is visible in the images as the central pole density maximum at $\alpha=0^\circ$ and the four broad pole density maxima at $\varphi=0, 90, 180,$ and 270° . No evidence of a fiber texture ring can be found. Therefore it can be concluded that the (100) dominated films grow in a cube-on-cube manner. The sample deposited at 270°C, additionally shows the previously described hexagonal pattern. The intensity is, however much weaker. This agrees well with the $2\theta-\omega$ measurements which showed that the hexagonal phase prevails to high temperatures as a minority phase (Figure 4-12). The hexagonal phase is not detectable anymore in the sample deposited at 310°C, which indicates that the epitaxial window for a pure cube-on-cube orientation relationship is very narrow near the desorption maximum. The two pole figures for the (100) orientation also show another interesting crystal orientation which is suggested to be a cubic GST(221) orientation from computer models, see Figure 4-16f. The (221) reflection is forbidden in a FCC structure and therefore it does not appear in $2\theta-\omega$ measurements. However, with pole figure measurements such “hidden” orientations are visible. The (221) orientation contribution consists of 4 rotational domains separated by 90° azimuthally, where one of the rotational domains is marked in red in the figure. The epitaxial relationship as suggested from the model is GST(221), GST[11-4] || KCl(100), KCl[011] and this 45° rotation agrees very well with the observed crystallites in the AFM images (Figure 4-14)^[112]. The presence of this orientation and its possible origin will be discussed in more detail in the following sections.

To relate the GST(111) and (221) orientation to the underlying cubic lattice as discussed above, some simple atomic models are proposed in Figure 4-17. These are just the visualization of the suggested model from the pole figure analysis and should only help the

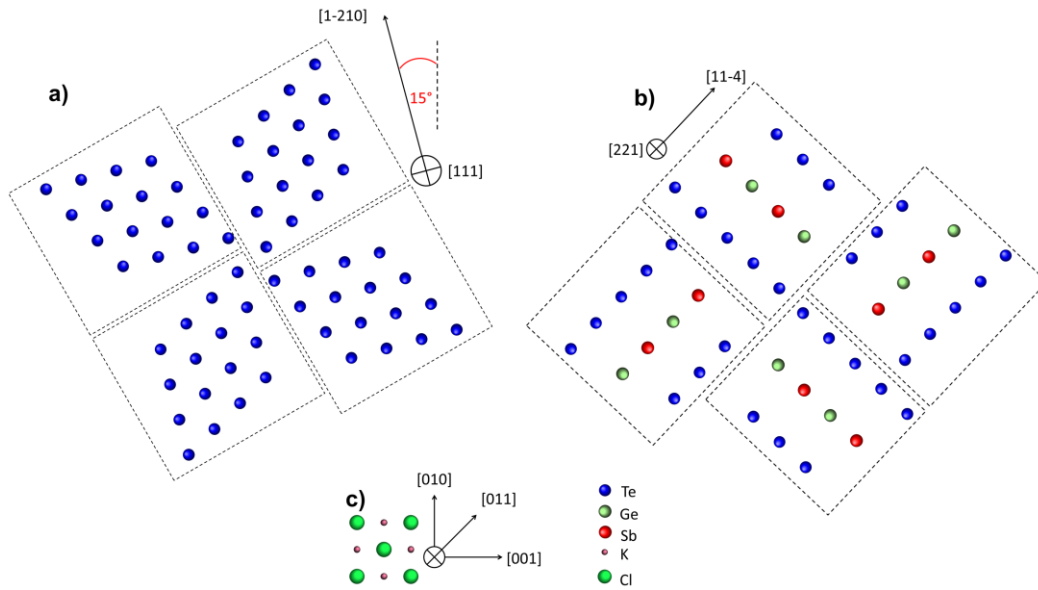


Figure 4-17. Simple atomic models of the 4 different rotational domains of (0001) oriented (a) and (221) oriented GST (b). In c), a KCl(100) crystal face is shown. Each dashed square box indicates a separated rotational domain. In each figure the depth direction only comprises one atomic plane. Characteristic crystallographic directions are indicated for each structure.

reader in an illustrative way. The atomic planes of GST(0001), GST(221) and KCl(100) is displayed in Figure 4-17a, b and c, respectively. Each rotational domain is marked by a dashed outline and all images are up to scale. Whereas the (0001) orientation only shows a number of small angle grain boundaries, the situation is more complex for the (221) orientation. The 45° rotation in Figure 4-17b is clearly visible and correlates well with the crystallite orientation seen from topography measurements. Furthermore, the problem in aligning the cubic (100) symmetry with the two proposed orientations is clear when comparing a) and b) with c).

4.2.2. The effect of deposition rate on the growth of GST on KCl(100)

Before this work, all epitaxial films of GST have been produced with MBE with comparably low growth rates. Since a higher deposition rate could influence the growth process in a significant way, a set of films was synthesized with different growth rates. The rate was varied by the use of different laser pulse frequencies between 1 and 100 Hz. It should be mentioned that the lowest growth rate used here is still almost a factor 10 larger than those typical for MBE^[23]. The deposition temperature was chosen to be 290°C, a temperature where the (100) orientation dominates the growth as known from the previous section, but where desorption of Ge and Te does not yet play an important role. In Figure 4-18, 2θ-ω scans of films deposited with 2.5, 5, 25 and 250 nm/min are presented. The peak at 25.45° belongs to a hexagonal phase and no peak shift can be seen for the different films, i.e. all films possess hexagonal content. As can be seen from the peak position markers (as adopted from Refs. 62 and 73) the measured intensity does not correspond well with any of the two phases. Due to this difficulty in differentiating between the hexagonal phases and due to the fact that it is a minority phase at this temperature, the hexagonal phase is therefore not further discussed. The 2θ-peak at 29.65° matches well

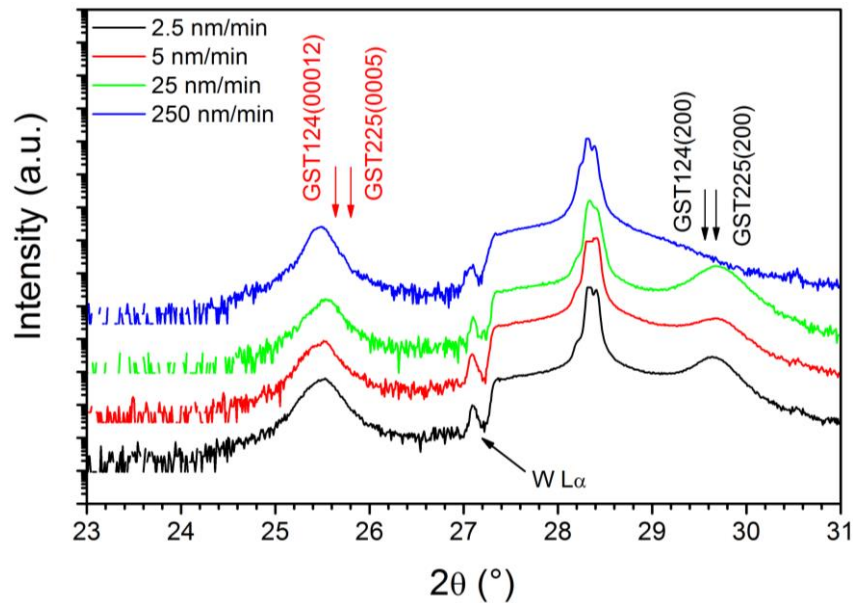


Figure 4-18. 2θ - ω scans for GST films deposited at different deposition rates. Hexagonal phase reflection positions are marked with red and cubic phase ones with black.

with the value of GST225(200). The position of the GST124(200) reflection is also marked for comparison. From EDX measurements (not shown here) it is found that no significant desorption of Ge and Te has taken place for any of the films deposited at this substrate temperature in the series and therefore the cubic GST225 phase is a likely candidate. The (200) peaks are broad with FWHMs of about 0.3 - 0.4° indicating the presence of many small crystallites, grown in a 3D-growth mode. No deposition rate dependent peak shift can be seen for the films. Interestingly, the film deposited with the highest rate shows no peak in this range, but only the hexagonal peak. A natural first assumption to consider would be to think that no cubic orientation has formed in this film. In-plane XRD measurements presented on page 53 will shed more light upon this observation. In any case, it is an indication that deposition at a high rate deteriorates the crystalline quality. The FWHMs of the (200) rocking curves are broad and measure roughly 1.5 - 1.6° , fully comparable with those in the previous section.

The topography of the films was measured with AFM and the result is presented in Figure 4-19. All films show the same fish-bone pattern as already observed in the previous section. The crystallites align according to two main directions separated by 90° azimuthally and with a 45° rotation relative to the substrate edge. The rms value increases slowly from 1 to almost 7 nm with increasing deposition rate. This is logical, since a higher deposition rate reduces the surface diffusion time for the adatoms before the next pulse with new material arrives at the surface. The AFM-images imply, being a surface sensitive technique, that the observed crystallite orientation is a surface phenomenon. The actual depth, however, of this crystal orientation has not yet been successfully proved as with SEM or TEM (due to sample preparation difficulties).

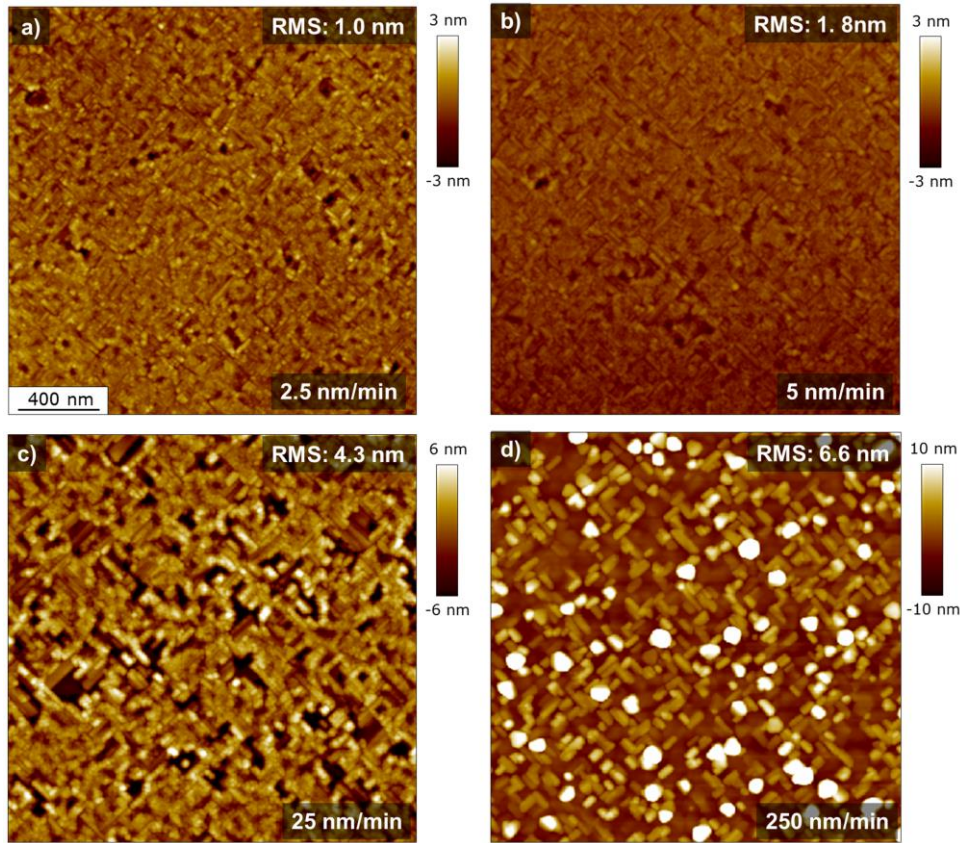


Figure 4-19. AFM images of the topography for GST films on KCl(100) deposited at 290°C with (a) 2.5 nm/min, (b) 5 nm/min, (c) 25 nm/min and (d) 250 nm/min. All films have a nominal thickness of 170 nm. The measured rms value is given in each figure. The scale bar in (a) is representative for all images.

To analyze the in-plane lattice parameter, 2θ - φ measurements were conducted. In Figure 4-20 the obtained results are presented. Two diffraction peaks are found for each film and the angular positions correspond to those of KCl(200) and GST225(200). All samples are characterized by a clear (100) orientation. The sample deposited at the smallest rate shows a peak shift to a higher angle around $2\theta=29.85^\circ$, corresponding to a lattice parameter of 0.598 nm which is smaller than the theoretical value of 0.602 nm. This can be explained considering the linear coefficient of thermal expansion for the two materials. Since KCl has twice the thermal expansion coefficient compared to GST at 290°C ($\sim 43 \cdot 10^{-6} \text{ K}^{-1}$ for KCl^[114] compared to $\sim 17\text{-}24 \cdot 10^{-6} \text{ K}^{-1}$ for GST^[115,116]), the deposited films should experience a compressive stress at room temperature which could explain the shift to higher angles. The film deposited with 25 nm/min shows an opposite behavior where a 2θ value of 29.28° gives rise to a lattice parameter of 0.61 nm, which is roughly 1.3% larger than the standard value of 0.602. Nevertheless, it is within the reported lattice parameter range for GST^[117,118]. The two remaining films are fully relaxed and match the theoretical value well. In Figure 4-21 the corresponding in-plane φ -scans for the GST(200) peaks are visible. The films show in general 4 peaks separated by 90° azimuthally. This is strong evidence of a cube-on-cube epitaxial growth. The φ -scan of the film deposited with 2.5 nm/min show only 3 peaks and a small broad bump were the missing peak would be expected. This is related to difficulties in the sample alignment of the film before measurement and is not an inherent property of the film. The same variation in intensities is

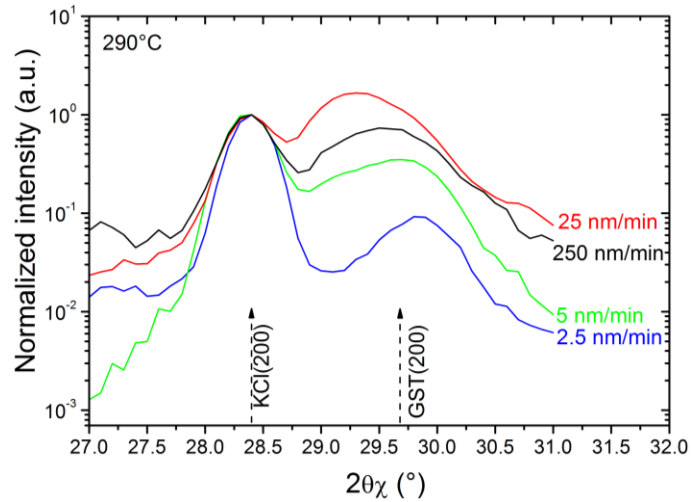


Figure 4-20. In-plane $2\theta\chi$ - ϕ measurements for GST films deposited at 290°C with different deposition rates.

also seen for the other films, where some peaks are more than twice as intense as the next peak. In the case of the 2.5 nm/min deposited films the absolute intensity is just weaker so that the peak disappears in the background. Comparing intensities from in-plane measurements is not as straight-forward, since a number of parameters influence the penetration depth of the x-rays and highest intensity does not automatically result from highest crystalline quality.

This is obvious when comparing the FWHMs of the ϕ -scans for the GST(200) peak. The films show an average in-plane rocking curve FWHM of 2.2° , 3.4° , 3.4° , and 4.8° for the samples deposited with 2.5, 5, 25, and 250 nm/min, respectively. The film deposited at the smallest rate exhibits the smallest twist component. This can be expected since a lower deposition rate gives the adatoms more time to find the energetically most favorable sites at the surface before the material generated by the next laser pulse impinges. Analogous, the film deposited at 250 nm/min displays the broadest rocking curve FWHM, since less time is available for surface diffusion of adatoms.

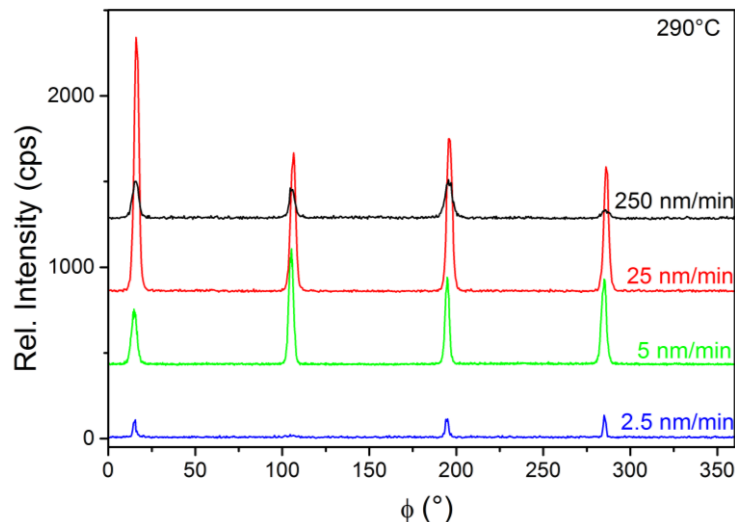


Figure 4-21. In-plane ϕ -scans for GST films deposited at 290°C with different deposition rates.

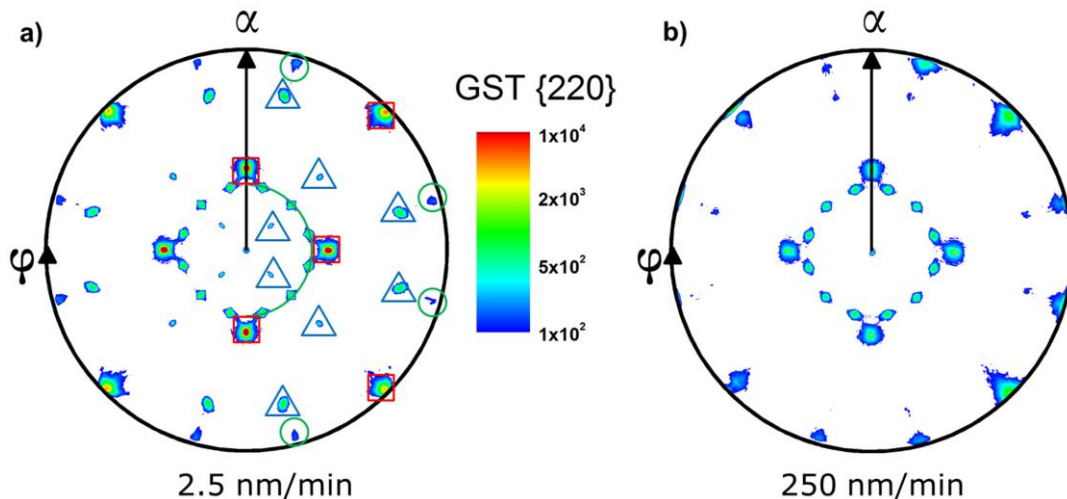


Figure 4-22. Measured pole figures of the GST{220} planes for samples deposited at 290°C with a) 2.5nm/min and b) 250 nm/min. In a), annotations are superimposed that mark the (0001) orientation (green) circles and semicircle, the (221) orientation (blue triangles) and the (100) orientation (red boxes). Intensity (cps) is shown on a logarithmic scale and applies for both images.

Finally, pole figure measurements were carried out for the films. The GST{220} reflection was chosen since the substrate contribution is drastically lowered at this 2θ position but, it is still a relatively strong scattering plane. In Figure 4-22, two pole figure measurements for the films deposited with 2.5 nm/min and 250 nm/min are displayed. In Figure 4-22a, the pole figure is additionally annotated in order to clarify the pole density maxima. The annotations have only been placed in the angular range $0 < \varphi < 180$, since the measurements are symmetric. Red boxes symbolize the cube-on-cube orientation, green circles and the large semicircle represent the hexagonal contribution and the blue triangles mark the (221) contribution. All orientations already described in the previous section are also present in the sample deposited at 2.5 nm/min, i.e. (0001), (100) and (221). The other films in the series show no qualitative differences, but they differ in the measured intensities. This can be seen in Figure 4-22b, which displays the film deposited at 250 nm/min. All major orientations can be accounted for, but the relative intensities have shifted. In fact, the (0001) orientation contributes with pole density maxima of similar intensity as the ones stemming from the (100) orientation. This is in agreement with the 2θ - ω measurements presented in Figure 4-18, where actually no diffracted intensity from the GST(200) can be seen. This once more shows that the GST films prefer to grow with hexagonal symmetry and only with low deposition rate and high temperatures is it possible to force the material into a cube-on-cube growth mode.

4.2.3. The effect of film thickness on the crystallite orientation

The observation of the crystallite orientation in the topography measurements in section 4.2.1 and 4.2.2, implies that the (221) orientation is related to the surface in a distinct way. Therefore, films with different thickness were deposited in order to study the influence of the film thickness on the crystal orientation. The deposition temperature was once more chosen to be 290°C, i.e. (100) dominated growth and no capping layer was deposited in order to minimize topography influences. All other deposition parameters were kept constant in order to obtain comparable results. In this section, five different films are

presented with thicknesses of 8.5, 17, 34, 68 and 170 nm as determined from XRR and SEM. The films were of similar chemical composition as the films deposited at 290°C in Figure 4-11 with no large deviation for any element. In Figure 4-23, 2θ - ω measurements of the films are presented. For the thinnest film, no clear diffraction peaks are visible except those from the substrate. A broad intensity distribution around the Cu $K\beta$ contribution of the substrate peak is present. Due to the thin layer thickness this could indicate the presence of a (0005) peak. This is more obvious for the next two samples with thicknesses of 17 and 34 nm. Clear peak broadening due to the finite thickness can be observed. Additionally, oscillation fringes are apparent for the two films indicating a smooth and homogeneous layer. The two thickest films also show a broad hexagonal (0005) peak similar to those presented in Figure 4-18 for thick films deposited with different deposition rates. The peak positions are again shifted towards lower angles compared with the Matsunaga model^[62] but they coincide well with the experiments presented previously in section 4.2.1 and 4.2.2. For the three thinnest samples, no (200) peak can be detected. However, this does not automatically mean that the films do not contain any (200) orientation as already observed in Figure 4-18 for the film deposited with highest rate. It could just indicate that the scattered intensity from the (200) planes is not high enough to allow discerning it from the substrate signal. For the two thickest films, broad but well discernable (200) peaks can be seen. For the sample with 68 nm thickness a small shift towards lower angles is obvious and in fact the value coincides well with the GST₁₂₄(200) position. However, no large deviations in composition can be detected with EDX that would explain such a phase transformation. The rocking curve measurements (not shown here) are comparable with the ones presented in Figure 4-12b.

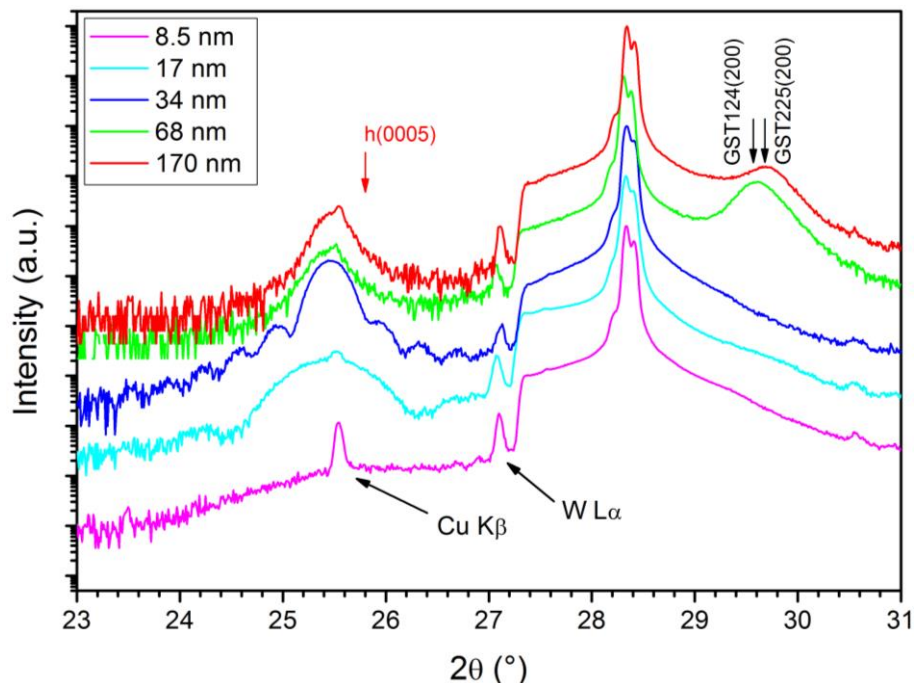


Figure 4-23. 2θ - ω scans for GST films deposited with different film thickness. Hexagonal phase reflection positions are marked with red and cubic phase ones with black.

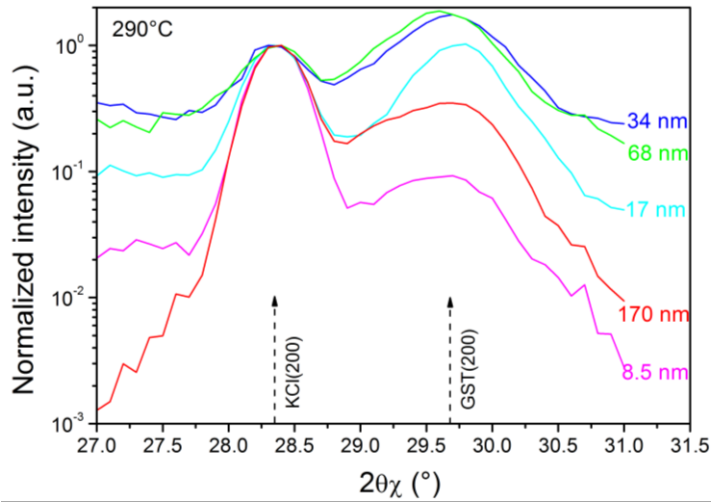


Figure 4-24. In-plane $2\theta\chi$ - φ measurements for GST films deposited at 290°C with different film thickness.

To verify if the films are cubic or not, in-plane XRD measurements were carried out. In-plane measurements are relatively insensitive to thickness induced peak broadening since the scattering planes are the planes perpendicular to the film surface. This is observed notably in Figure 4-24, where diffracted intensity at the GST225(200) peak position is observed for all films in this series. The angular position of the peaks is in all cases in good agreement with the GST225(200) position and no obvious broadening of the peaks is present. As already mentioned in the previous section, the absolute intensity is not a measure of the crystal quality and this is obvious, when the in-plane rocking curves of the GST(200) reflection are regarded. The scans of all films display four individual peaks separated by 90° azimuthally. The average FWHM of each film vary between 2.2 and 3.4° with no systematic ordering. As a comparison an in-plane φ -scan of the KCl(200) is also presented and it directly evidences that the films grow in cube-on-cube manner. The FWHM of the substrate peak is $\sim 1^\circ$ which is significantly lower than the measured FWHMs of the films peaks. This illustrates that the cube-on-cube orientation is not particularly well oriented and the same behavior has been seen for the MBE deposited epitaxial GST films on (100) oriented cubic substrates^[23,110].

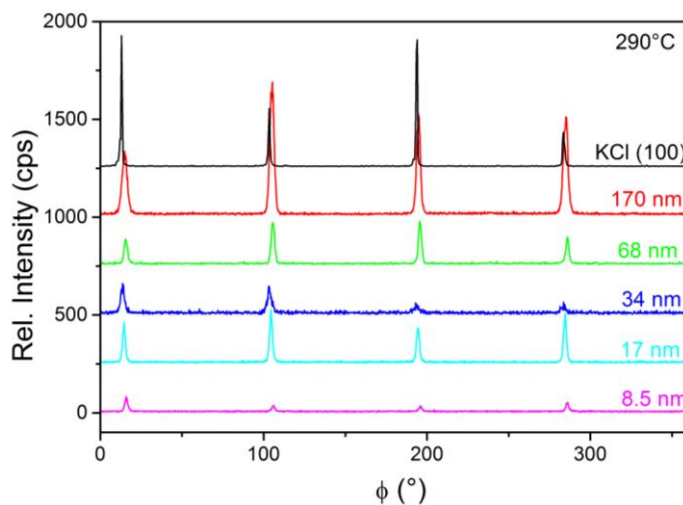


Figure 4-25. In-plane φ -scans for GST films deposited at 290°C with different thickness and a KCl(100) substrate.

From the in-plane measurements, it is now confirmed that the films are epitaxial in a cube-on-cube arrangement. However, other orientations could be present, i.e. (the 221) orientation which does not show up in the in-plane measurements. Therefore, GST{220} pole figure measurements were carried out for all samples in the investigated range. For the 8.5 nm film no other pole density maxima than those of the substrate were found due to the finite thickness. Hence it is not presented here. Pole figures of the other four films are shown in Figure 4-26 with a logarithmic intensity scale in common. The 17 nm and 34 nm thick films are qualitatively the same (Figure 4-26a and b) with twelve pole density maxima distributed in a ring shape at $\alpha=35\pm 1^\circ$. This is correlated to the (0001) orientation (4 domains rotated by 90° azimuthally, see section 4.2.1). Additionally, a cubic (100) orientation at $\alpha=45^\circ$ can be seen for the two films. The intensity is quite weak and cannot be separated from the substrate contribution. The films are characterized, however, by a cube-on-cube (100) orientation as evidenced from the in-plane φ -scans, but the low thickness makes it hard to resolve it in the pole figures. Noticeable is that no other crystallographic orientations can be discerned, i.e. the (221) orientation. This means that the (221) orientation seen previously, is either not present or cannot be measured. The two thicker films are also qualitatively the same compared with each other (Figure 4-26c and d). The (0001) orientation is in both films clearly visible and the (100) orientation is now much stronger present. Also, now the (221) orientation is present. For the 68 nm thick film it is just emerging, but for the 170 nm thick film a distinct pattern is observable. The (221) orientation thus seems to be related to a critical thickness, possibly due to a stress

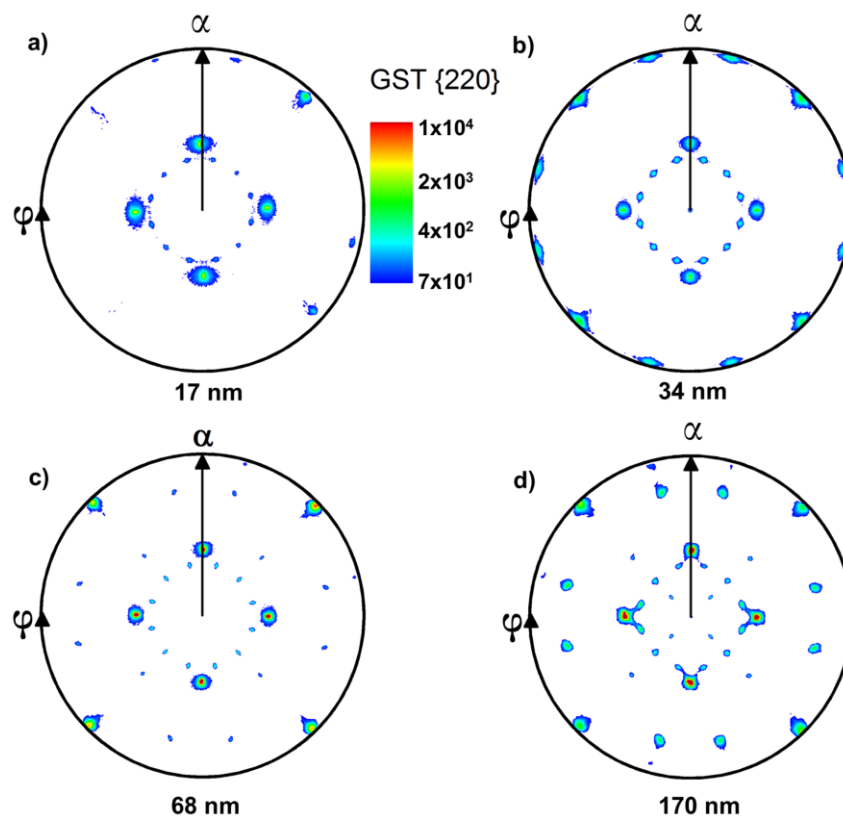


Figure 4-26. Measured pole figures of the GST{220} planes for films deposited at 290°C of thickness a) 17 nm, b) 34 nm, c) 68 nm and d) 170 nm. Intensity (cps) is shown on a logarithmic scale and applies for all images.

relaxation mechanism. Since all the previous studies on the epitaxial growth of GST based films on (100) oriented substrates were conducted in the thickness range 30–60 nm^[21-24,110,111], no literature data is present to confirm these findings.

The topography of the films was measured with AFM and the results are presented in Figure 4-27a, b, c and d for 8.5, 17, 34, and 68 nm thick films, respectively. The 8.5 nm film is decorated with many small crystallites with a diameter between 15-25 nm. The crystallites appear to have a random in-plane orientation and it is not possible to deduce any specific crystallographic directions. From the in-plane measurements, it is known that there must be (100) oriented cube-on-cube crystallites in the film, but it is at this point not likely that the crystallites visible in Figure 4-27a can be ascribed to this orientation. More likely, the (100) orientation is buried underneath and the crystallites visible in the image have nucleated on top of this layer with a random in-plane orientation. The same picture emerges from the 17 nm thick film with the exception that the crystallites are now between 35-45 nm in size. Still no apparent in-plane orientation can be found. Therefore, it can be deduced that the (100) and (111) orientations seen from the pole figure and in-plane measurements must be buried underneath.

For the 34 nm thick film in Figure 4-27c the situation looks different. The crystallites are now starting to align according to the fishbone pattern seen in Figure 4-14c and Figure 4-19 as indicated by the two dashed lines. Interestingly, from the pole figure measurement (Figure 4-26b), only the cube-on-cube (100) and (111) orientation are present and no indications at all of any orientation that is aligned 45° with the substrate (100) planes. However, judging from the crystallite size and number in the AFM image, there is probably not enough material volume present to obtain any measurable scattered x-ray intensity and therefore it is not visible in the pole figure. For the 68 nm thick film (Figure 4-27d), the crystallites cover the complete surface and the fishbone pattern is fully closed as indicated by the two solid white lines. This topography is qualitatively identical with the topography seen for all films that are mainly (100) oriented and thicker than 68 nm. It is also consistent with the pole figure measurement from Figure 4-26c that clearly shows the additional (221) orientation. Therefore, a strong correlation between the evolution of the fishbone pattern and the (221) orientation seen in the pole figures is found. The reason, however, is not yet clear, since the common case to accommodate for substrate lattice misfit and other growth related stress contributions is to introduce misfit dislocations and other defects in the beginning of the growth in the vicinity of the substrate-film interface^[119,120]. In this case, it seems to be a nucleation effect that takes place at the surface of the growing film and therefore should be related to the end stage of growth. Residual stress resulting from differences in thermal expansion (~ 20 compared to $43 \cdot 10^{-6} \text{ K}^{-1}$) could be involved since the films experience a compressive stress which would need to be accommodated in a way. It is possible that the formation of the (221) orientation could act as such a stress relaxation mechanism. The fact that only the (221) orientation is present at high deposition temperatures further hints at the differences in thermal expansion as a plausible explanation.

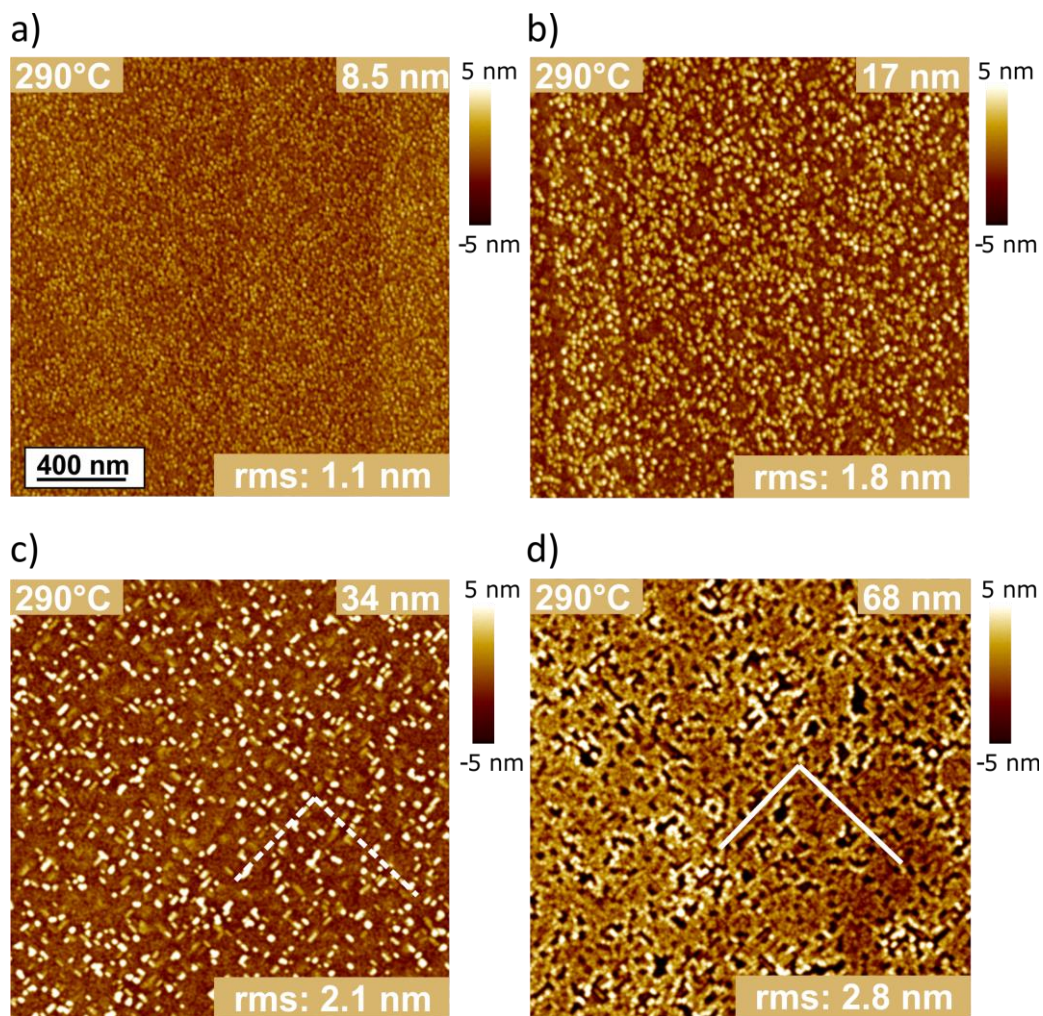


Figure 4-27. AFM images of the surfaces of epitaxial GST films of thickness (a) 8.5 nm, (b) 17 nm, (c) 34 nm and (d) 68 nm. All films were deposited at 290°C with a nominal thickness of 170 nm. The white dashed lines in (c) indicate the onset of a (221) crystallite orientation and the solid white lines in (d) indicate a fully evolved (221) orientation. The measured rms value is given in each figure. The scale bar in (a) is representative for all images.

4.2.4. Summary of the results on the deposition of GST on KCl(100)

In this section the growth of GST on KCl(100) was investigated. Three deposition parameters were investigated: substrate temperature, deposition rate and film thickness. It was found that the temperature has a very strong influence on the crystal growth in the films. At low temperatures ($<140^{\circ}\text{C}$) amorphous films grow which transform into polycrystalline fiber textured (0001) films in the substrate temperature range of $140\text{-}200^{\circ}\text{C}$. Between $200\text{-}270^{\circ}\text{C}$ only hexagonal (0001) textured/epitaxial GST films are found. Above this temperature the cubic (100) orientation dominates the growth. This indicates that PLD-deposited GST films can only be forced to grow in the cubic (100) orientation at high temperatures. In fact, the substrate temperature where only a pure (100) orientation is obtained is very close to the temperature where full desorption of the deposited material takes place. The out-of-plane rocking curves are typically a few tenths of degrees wide for (0001) dominated films and $1.5\text{-}2^{\circ}$ for (100) dominated films. This implies that the pre-

ferred orientation to grow along is the [0001] direction. A previously unknown crystal orientation is furthermore found in the (100) dominated temperature regime, namely the (221) orientation.

An increase of deposition rate weakly deteriorates the crystal quality in the investigated range between 2.5- 250 nm/min for samples deposited in the (100) orientation dominated regime. Nevertheless, the films grow epitaxial at all deposition rates.

Variation of the film thickness from 8.5 nm up to 170 nm in the (100) orientation dominated temperature regime revealed that the (221) orientation is not present at thicknesses below 68 nm. Above that thickness the (221) orientation emerges and at 170 nm the (221) orientation is fully evolved.

4.3. Epitaxial growth of GST on BaF₂(111)

In chapter 4.1.3 it was shown that GST films on KCl(100) prefer to grow in a [0001] direction. This suggests that by using a substrate with hexagonal symmetry, the number of occurring crystallite orientations could be reduced. To investigate if that is the case GST films were deposited on freshly cleaved BaF₂ that was cleaved parallel to the (111) planes. In this chapter the effect of substrate temperature on the growth of GST on BaF₂ as well as on deposition rate and pressure will be discussed.

Table 5. General deposition conditions on the growth of GST on BaF₂(111)

No. of pulses	Frequency (Hz)	Fluence (J/cm ²)	Ar-pressure (mbar)	Pre-heating at substr. temperature (min)	Capping layer LaAlO _x (nm)
4000	10	0.8±0.2	4·10 ⁻⁵	>30	~10-15

4.3.1. The effect of substrate temperature on the growth of GST on BaF₂(111)

A set of films was deposited between RT and 295°C. The used number of pulses and pulse frequency led to a typical average film thickness of 120 nm and a deposition rate of 18nm/min. However, some films were much thinner as a case of multi-usage of the deposition system and the resulting multilayer coating on the laser beam entrance window that blocks some of the irradiation. Above 295°C, significant desorption of material was observed and therefore films were not deposited at higher temperature. The desorption component in the films at high substrate temperatures is mainly that of Ge and Te as evidenced in Figure 4-28a. The composition remains relatively stable over a large temperature range and only at the highest temperature significant loss of Ge and Te can be seen. The overall trend is similar to the one measured for GST films deposited on KCl(100), see Figure 4-11. In Figure 4-28b-d, SEM images of three different films deposited at 85°C, 210°C and 295°C are displayed, respectively. The topography is smooth and no signs of

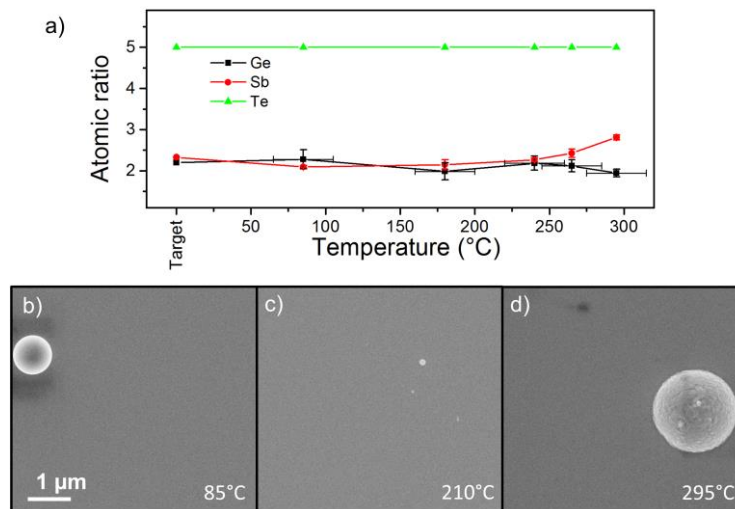


Figure 4-28. Composition as measured by EDX for GST films deposited at different temperatures (a) and SEM images of selected films (b)-(d). The particulates in the images are only there to show that the images are sharp.

delamination have been found. Compared to the films displayed in Figure 4-13, the GST films on BaF₂(111) are almost featureless. Even at higher magnifications (not shown here) no signs of crystallites can be observed.

The crystalline structure of the films was determined by 2 θ - ω scans. The results are displayed for films deposited between 55-295°C in Figure 4-29. The film deposited at 55°C is in the amorphous state, but already the next film deposited at 85°C exhibits diffraction peaks at the angular position marked by the (0005) and (00010) annotation. Already at this temperature, much higher intensities are recorded than for the polycrystalline textured films in section 4.1. It should be noted that this deposition temperature is much below any reported temperature for GST crystallization, irrespective of crystal structure. For instance, the cubic phase crystallizes at ~140°C while the hexagonal phase normally crystallizes around 300°C^[121]. The reduced substrate temperature in the deposition process is ascribed to the energetic particles in the laser ablation plasma plume. Upon raising the temperature the diffraction peaks get more intense, indicating that the degree of crystalline order in the films increases with temperature. At temperatures above 180°C even third order diffraction peaks are visible, illustrating the good crystalline quality of the films. The substrate main peaks are annotated in red, but satellite reflections (from Cu K β related peak and others) are also visible where one of them is marked by a red asterisk. The angular position of the main film peaks are in very good agreement with the model from Matsunaga^[62], with the exception that the c-axis is slightly larger (~1.74 nm compared to 1.724 nm). There exists however, one deviation from this observation and that is the broad peak at ~12.6° for the two films deposited at 125°C and 155°C. The angular position of this peak actually correlates well with the position of the GST124(0006) reflection, which is marked with blue annotations. However, it is not believed that the films are of GeSb₂Te₄ composition, since the substrate temperature was modest in both cases and the EDX data also do not support this. A more likely assumption is that the vacancy layer

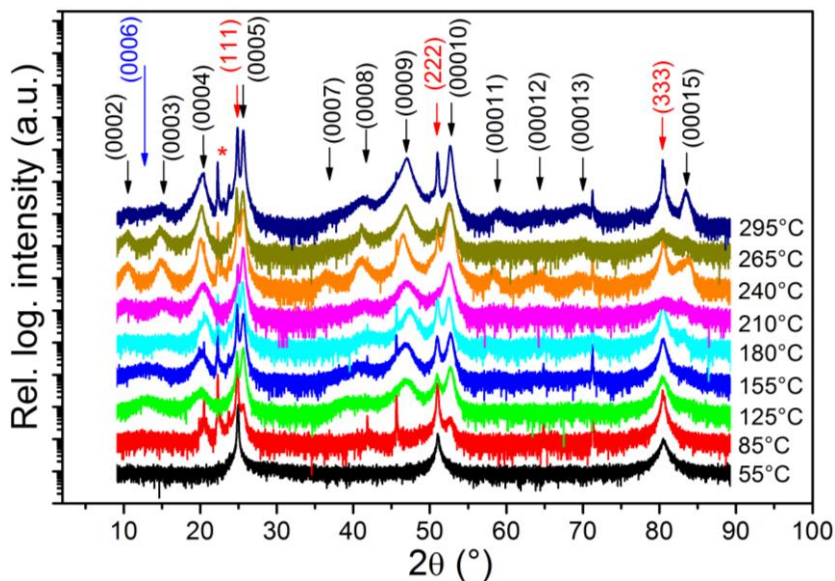


Figure 4-29. 2 θ - ω scans for GST films deposited at different temperatures (a). Hexagonal positions belonging to the GST225 phase are marked with black and hexagonal positions belonging to the GST124 phase are marked with blue. Substrate contributions are annotated in red.

ordering in the films, which is characteristic for the hexagonal phase^[62,64], is not fully developed and therefore contributes to a broad and ill-defined peak. This could also account for the fact that all (000*l*) peaks with $l < 5$ are much broader than the (0005) reflection. Finally, only reflections from crystallographic planes parallel with the hexagonal basal plane are observed. This indicates that the GST growth on BaF₂(111) proceeds with much higher quality than on (100) oriented substrates^[23,108]. In the case of MBE, however, the resulting GST phase is, with few exceptions, reported to be cubic. There are indications though, that also hexagonal films are produced when Si(111) is used as a substrate in MBE growth as can be seen in Refs. 69 and 103.

Extracted data from the 2θ - ω measurements are plotted in Figure 4-30. The black curve symbolizes the development of the FWHM of the (0005) peak for the films deposited at different temperatures. It is evident that the peaks get narrower with increasing temperature. This is expected, since a higher deposition temperature enhances adatom mobility and promotes grain growth. Additionally, no temperature dependent peak shift is observed (blue curve in the figure). At 240°C the (0005) peak is split into two components, one continuing the general trend and one that resides outside as indicated by the dashed line. Similar observations have been made on the epitaxial growth of GST on Si(111) in section 4.4.1 and the peak splitting will be discussed in conjunction with those results.

To get an impression of the crystallite tilt distribution in the films rocking curves of the (0005) peak were measured. The measurements are shown in Figure 4-31. As can be seen all peaks are characterized by a broad peak shape that gradually gets narrower with increasing temperature. The very narrow peak in the middle of the rocking curve is believed to partially originate from the substrate due to the fact that the angular separation in 2θ for BaF₂(111) and GST(111) reflections is only about 0.8°. Therefore, it was cropped for display purposes only. To eliminate the measurement from this contribution, a crystal analyzer on the receiving side in the diffractometer would have to be used. For intensity reasons this is not possible. The two films deposited at the highest substrate temperatures show only one peak and it is not possible anymore to fit this peak with a substrate contribution and film contribution in a sound way. The extracted FWHMs of the (0005) rocking curve are displayed in the inset. A reduction in FWHM is seen with increasing substrate

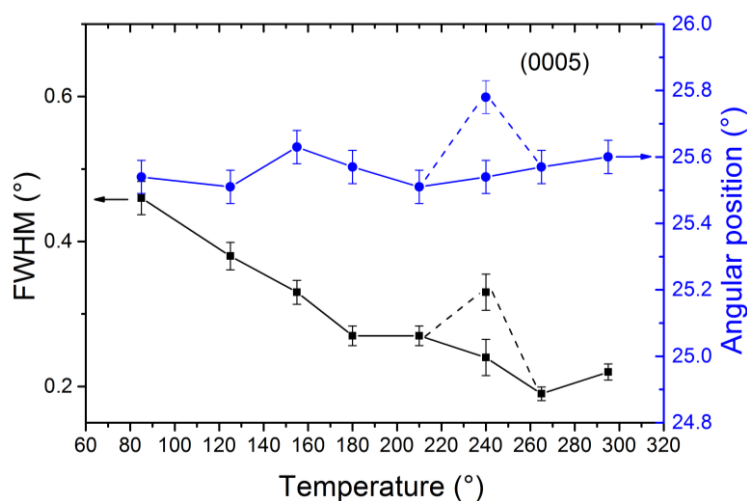


Figure 4-30. FWHM and angular position of the GST(0005) peak.

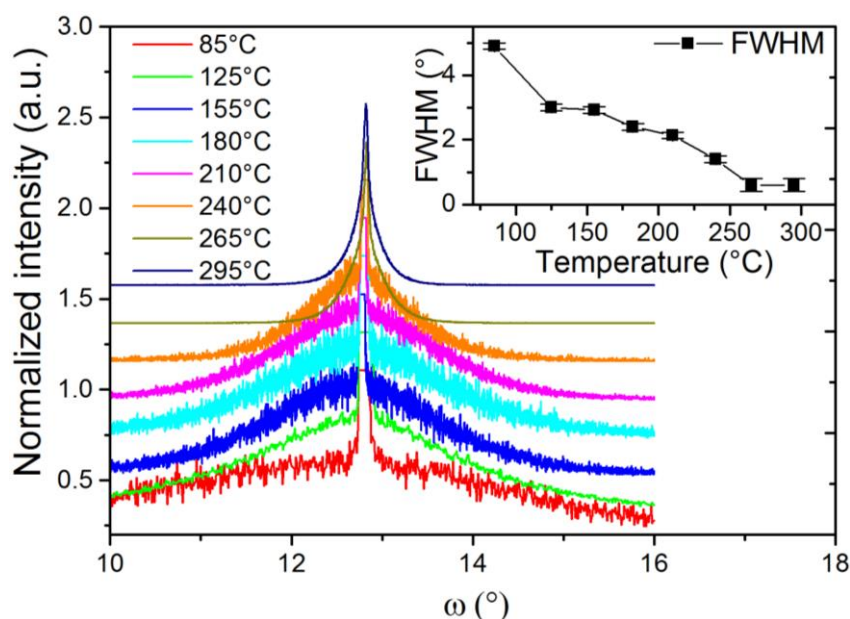


Figure 4-31. ω -scans of GST films deposited at different temperature. The sharp peak in the middle was cropped for clarity, see discussion in text. The inset shows the FWHM of the measured rocking curves.

temperature which is logical due to the enhanced surface diffusion. The absolute values are somewhat surprising though, since they are higher than for the rocking curve from GST(0005) films on KCl(100) substrates at the corresponding temperature as displayed in Figure 4-12b. However, it cannot be ruled out that the narrow peak in the middle only stems from the substrate. Therefore, the rocking curve FWHMs could be smaller than the values actually presented.

This is further substantiated by TEM analysis of selected films as shown in Figure 4-32. Firstly, a cross-section TEM overview of a film deposited at 180°C is depicted in Figure 4-32a. The film is homogenous without any clear grain boundaries. The red circles (not to scale) in Figure 4-32a, indicate where the information in the two Selected Area Diffraction (SAD) patterns is obtained from. The left SAD pattern reveals a hexagonal structure as seen along the [2-1-10] direction. Substrate reflexes appear clearly as bright spots, whereas the GST film induces streaks running almost vertically in the image. Since the FWHM of the (0005) reflections is roughly 0.2° (see Figure 4-29) (which results in an estimated crystallite size of 40-50 nm using the Scherrer equation) and the smallest SAD aperture is 110 nm, more than one crystallite should add intensity to the diffraction pattern. However, the streaks are well aligned along the [111] direction of the substrate, indicating a very small crystallite tilt component. The presence of streaks in reciprocal space suggests that there are two-dimensional features in the film parallel to the electron beam and the fact that they are aligned with the substrate [111] directions means that the two-dimensional objects are also parallel with the substrate surface plane. Furthermore, the streaks are quite diffuse with no clear spot pattern. This is due to two reasons: Firstly, the dynamical contrast range is limited because of the high substrate intensity making it hard to resolve weakly scattered spots. In fact a spot pattern is visible upon closer inspection (top SAD pattern) corresponding well with that of hexagonal GST. The streaks are, however, still present. The amorphous ring pattern in this SAD image comes from the amorphous Pt-

overlayer from the focused ion beam process. Secondly, it is known from 2θ - ω measurements (Figure 4-29) that the crystalline order along the growth direction is not perfect since, the (000l) peaks for $l < 5$ do not match the theoretical positions of the different models^[62,73] in perfect agreement. Such a disorder along the [0001] direction would manifest itself as differences in the vacancy layer stacking sequence, (see section 2.2 for vacancy layer stacking) and accordingly smear the diffraction spots along the [0001] direction and that is exactly what is observed^[122]. This once more suggests that the FWHM from the rocking curve measurements is actually a bit underestimated. In Figure 4-32b, a STEM image of the same sample (deposited at 180°C), viewed along the [2-1-10] direction is presented. One horizontal (111) plane in the substrate is annotated with a dashed white

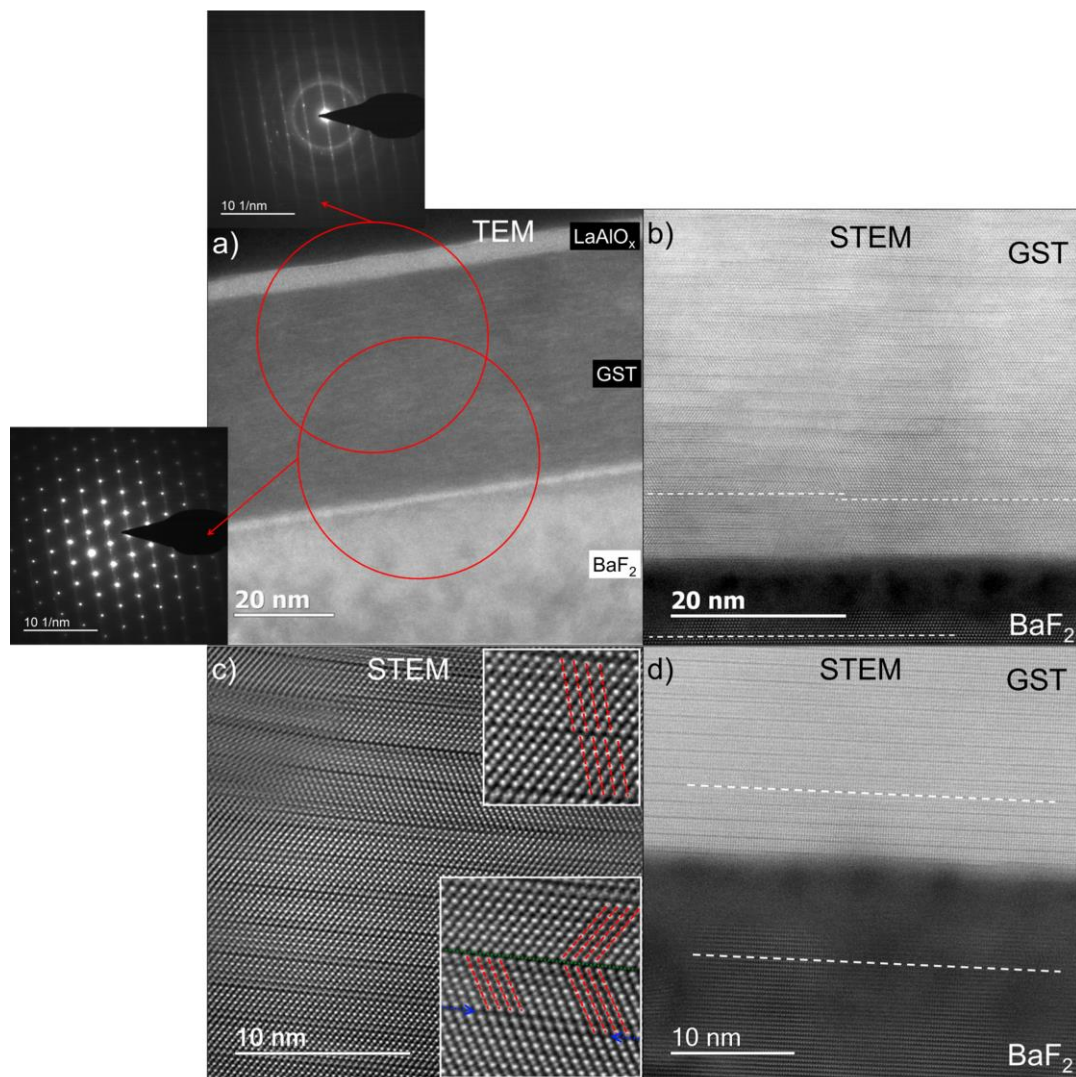


Figure 4-32. Transmission electron microscopy images of selected GST films. In (a) a bright-field TEM image of a film deposited at 180°C is seen. Two corresponding SAD patterns are presented from film regions indicated by the red circles (not to scale with the SAD aperture). In (b) a large STEM image of the same film is shown, where the dashed white lines indicate parallel layers. In (c) a high-resolution HAADF-STEM image of the same film is presented. In the large inset vacancy layers are annotated with blue arrows and a twin boundary with a green dotted line. The small inset shows GST{20-23} planes in red. In (d) a large STEM image of a film deposited at 295°C is shown. The dashed white lines indicate parallel layers.

line in the bottom part of Figure 4-32b. The film on top also shows horizontal planes as indicated by the two white dashed lines. These planes, belonging to the $(000l)$ family are perfectly parallel with the substrate. However, the planes do not propagate parallel over the whole image length as indicated by the offset between the lines. In this middle part of the image a large disordered region is present where the vacancy layer (VL) planes annihilate. This is possibly a crystallite with a slightly different orientation which could explain the broad base peak in the rocking curve measurements. The impression of well oriented (0001) films with a small tilt component but not so highly ordered along the $[0001]$ direction is further substantiated through this image. A HAADF-STEM image of the same film is presented in Figure 4-32c. In this image a black line of missing intensity corresponds to a vacancy layer and the brightest spots to Te atoms. Obviously, the film consists of blocks separated by VLs. Each block consists of 4-6 Te layers, whereas the ideal 225 composition should give a spacing of 5 layers^[62]. Local EDX measurements reveal a composition of 20:24:56 at.% for Ge:Sb:Te, respectively, which could explain the local variations in VL spacing. However, even for synthetically grown bulk GST crystals a deviation from this recurrence pattern is common^[64]. The disorder in the VL stacking is apparent; VLs merge into each other and annihilate just to appear again at another place. At the left part in the image another crystallite with a slightly different orientation is visible which further enhances the impression of a disorder along the growth direction which can account for the peak broadening seen for the $(000l)$ with $l < 5$. Several twin boundaries are also visible in the image and one of them is marked by a green line in the large inset. In the small inset the red dashed lines indicate Te rows that are shifted between each VL. These Te rows correspond well with the $\{20-23\}$ planes in the hexagonal GST225 phase. In Figure 4-32d a film deposited at 295°C. This film was deposited with 1 Hz, i.e. ten times slower than the other films in the series and consequently was subjected to a high temperature longer than for the other films. This is reflected in the local composition that measures 8:34:58 at.% for Ge:Sb:Te, i.e. even less Ge than in the 124 phase. Similar observations have been made for MBE deposited epitaxial films that were heated for a long time^[109]. Nevertheless, it is observed that the temperature has a beneficial effect on the degree of VL ordering. Now the VLs extend over the whole image side without any distortion. This explains why the rocking curve improves with increasing substrate temperature.

The in-plane lattice parameter is in good agreement with the GST225 model as displayed in Figure 4-33. All films show diffracted intensity in the vicinity of the hexagonal $(2-1-10)$ reflections position except the film deposited at 85°C which is shifted more towards the cubic $(20-2)$ reflection position. From φ -scans of the hexagonal $\{10-16\}$ reflections and pole figure analysis, a hexagonal phase in this particular film has been identified (not shown here). To prove the co-existence of the cubic phase, however, turns out to be rather difficult, due to similarities in crystal structure, i.e. all cubic diffraction peaks have corresponding hexagonal peaks nearby. Nevertheless, this could indicate that the films grow in a mixed cubic/hexagonal mode at low temperatures. Differences in thermal expansion coefficient could be another reason for this peak shift, but it is not likely, since the differences are very small between BaF_2 and GST. In fact, the thermal expansion coefficient of both materials are about $20 \cdot 10^{-6} \text{ K}^{-1}$ as described in Refs. 116 and 123.

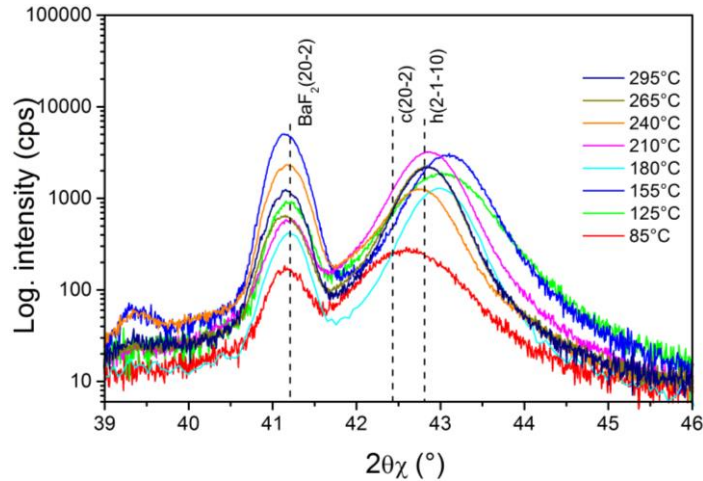


Figure 4-33. In-plane 2θ - ϕ measurements in for GST films deposited at different temperatures.

In-plane ϕ -scans in Figure 4-34 of the GST{2-1-10} peaks for the same set of films evidences the hexagonal symmetry of the films. Every 60° a sharp peak arises. The FWHM evolution of the peaks is presented at the right side of the figure. With increasing substrate temperature the FWHM of the in-plane rocking curve gets narrower. At the highest substrate temperatures the width is roughly 1.2° , i.e. more than twice that of the substrate. However, the substrate peak width is limited by the 0.5° Soller slits used and cannot automatically be used as a quality reference. Instead, by comparing the FWHM of the films deposited on KCl(100) substrates in the previous section (Figure 4-21), it is found that the growth of GST on $\text{BaF}_2(111)$ is substantially improved.

The presence of twins has been confirmed with STEM imaging, but only for one film. To investigate the temperature dependence of the twin formation, pole figures of the hexagonal {10-13} reflections were recorded for all films. Intensity calculations of the diffracted x-rays from the (10-13) planes, as calculated by CaRIne^[75], reveals that there are two sets of {10-13} planes that scatter differently in the hexagonal Matsunaga model^[62]. The two planes are visualized in Figure 4-35a. The dashed red line indicates a weakly scattering

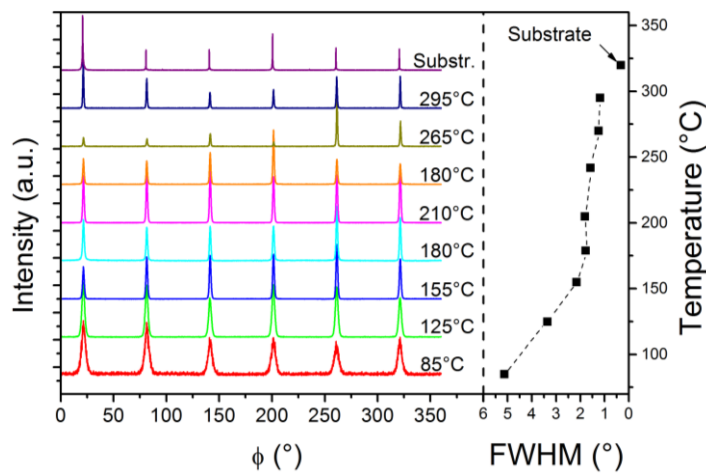


Figure 4-34. In-plane ϕ -scans of the GST{2-1-10} peaks for films deposited at different temperatures (left side) and corresponding FWHM values (right side). The dashed line is only intended as a guide for the eye.

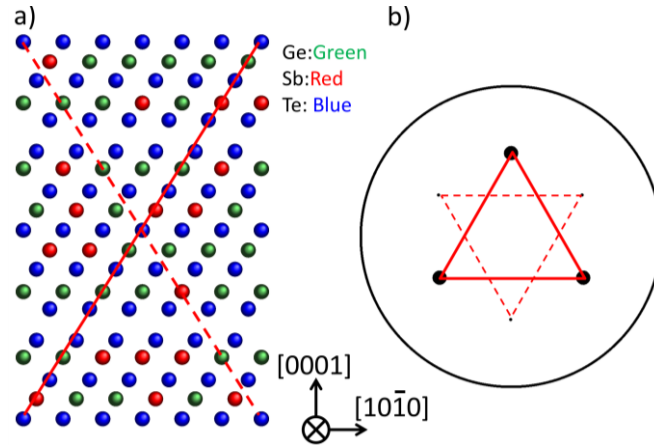


Figure 4-35. Projection of a hexagonal GST225 crystal along $[2-1-10]$ showing the two different types of $\{10-13\}$ planes (a). The corresponding modeled pole figure of the GST $\{10-13\}$ reflections (b). Large dots symbolize high intensity and small dots low intensity.

plane and the red solid line indicates a strongly scattering plane. This is easy to understand when comparing the atomic positions in the planes. Clearly one of the planes contains more atoms than the other and therefore scatters stronger. A measured pole figure of these planes in a perfect hexagonal GST225 single crystal therefore contains three strong pole density maxima and three much weaker ones as depicted in Figure 4-35b. With that in mind, the measured pole figures of the GST films on $\text{BaF}_2(111)$ can be considered. In Figure 4-36a-h, the results of the pole figure measurements for the deposited films in this experimental series are depicted. Already the first film (deposited at 85°C) shows six, i.e. two times three, broad but well-separated pole density maxima. This confirms that epitaxial growth of GST on $\text{BaF}_2(111)$ is possible already at such low temperatures. The six pole density maxima are separated by 60° in β and are of equal intensity meaning that two rotational domains (RD) exist in parity, rotated by 180° with respect to each other. One of the RDs is aligned with the substrate with the orientation relationship $\text{GST}[-12-10] \parallel \text{BaF}_2[1-10]$ and the other with $\text{GST}[1-210] \parallel \text{BaF}_2[1-10]$ ^[124]. This is typical for all films deposited in the temperature range $85-210^\circ\text{C}$. The pole density maxima additionally get narrower and the peak intensity increases with increasing substrate temperature. Above this temperature, the RD oriented as $\text{GST}[1-210] \parallel \text{BaF}_2[1-10]$ starts to dominate the growth as displayed in Figure 4-36f, which is in good agreement with group theory predictions on epitaxial rotational domains^[113]. A further substrate temperature increase improves the spatial distribution of the peaks, i.e. crystalline quality, but does not otherwise reveal any new information. Interestingly, the pole density maxima are not especially round in shape, but the intensity is distributed like in an arrow shape. This indicates that the twist and tilt components in the films prefer to align along certain directions. To further elucidate this observation, high resolution reciprocal space maps are needed which for intensity reasons were not possible to obtain. For the films deposited at the two highest temperatures the intensity ratio between the strong RD and the other is about 10-50 which is slightly less than proposed from the intensity calculations in CaRIne. Therefore, the films consist of either a very dominating RD or perhaps even a single domain (compare with the pole figures on p. 73). The presence of twin domains in GST films is not unique for the PLD method but has also been observed in the deposition of

GST films with MBE on (111) oriented substrates^[24,69]. In fact, the twin ratio in the MBE deposited films can be as low as 1:1^[69]. Hence it is concluded that PLD deposited epitaxial GST films on BaF₂(111) substrates are of high crystalline quality, fully comparable with or even better aligned than MBE deposited ones.

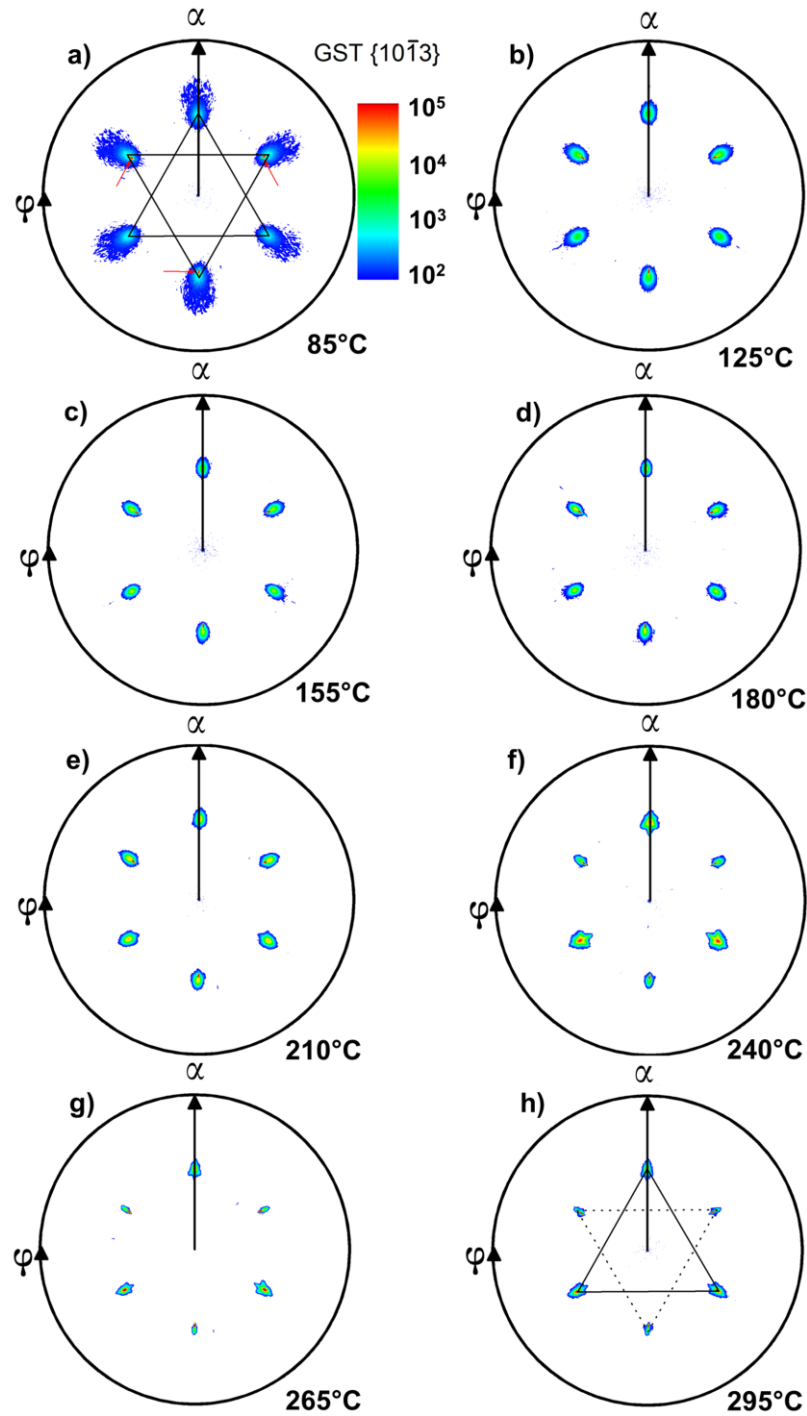


Figure 4-36. Measured pole figures of the GST{10-13} reflection for films deposited at a) 85°C, b) 125°C, c) 155°C, d) 180°C, e) 210°C, f) 240°C, g) 270°C and h) 295°C. The red arrows in a) indicate substrate contributions and the triangles indicate rotational domains. Intensity (cps) is shown on a logarithmic scale and applies for all pole figures.

4.3.2. The effects of deposition rate and pressure on the growth of GST on BaF₂(111)

In section 4.2.2, it was shown that the growth of GST on KCl(100) remained epitaxial even though the deposition rate was increased by a factor 100. To verify if the same behavior is found on (111) oriented substrates, films were deposited with different pulse frequencies in the range from 1 to 100 Hz, resulting in deposition rates between ~2-180 nm/min. Additionally, one film was deposited with a substantially higher Ar-flow (100 sccm, instead of 1 sccm) which resulted in a background pressure of $5 \cdot 10^{-3}$ mbar. A higher background pressure could influence the growth in two ways: reduction of the average particle energy in the PLD plasma due to scattering events and reduction of desorption at higher temperatures. The substrate temperature was chosen to be 265°C, such that a good balance between stoichiometry and crystal quality was obtained.

In Figure 4-37, the 2θ - ω measurements of the films are presented. For the two films deposited with 100 and 10 Hz (black and red curve), a diffraction pattern corresponding to that of the hexagonal GST225 phase was found. All diffraction peaks are in good agreement with the black arrow pattern marked in the image. The peak positions are shifted slightly compared to the Matsunaga model^[62], but are in good agreement with all previously measured films (see for instance Figure 4-12). Based on the angular position of the (0005) peak a c-axis between 1.74 and 1.75 nm is obtained. Only (000 l) reflections are visible, which indicates at least a textured growth. The green curve stems from the film deposited with 1 Hz and now a different diffraction pattern can be seen. This is especially visible for diffraction peaks below 20° in 2θ . Instead of three peaks at roughly 5, 10 and 15°, two peaks appear at 6.3 and 12.6°. This is in good agreement with the hexagonal GST124 phase as indicated by the blue arrows in Figure 4-37. A phase transition from the 225 to the 124 phase seems to be initiated by a reduction in deposition rate. However, the

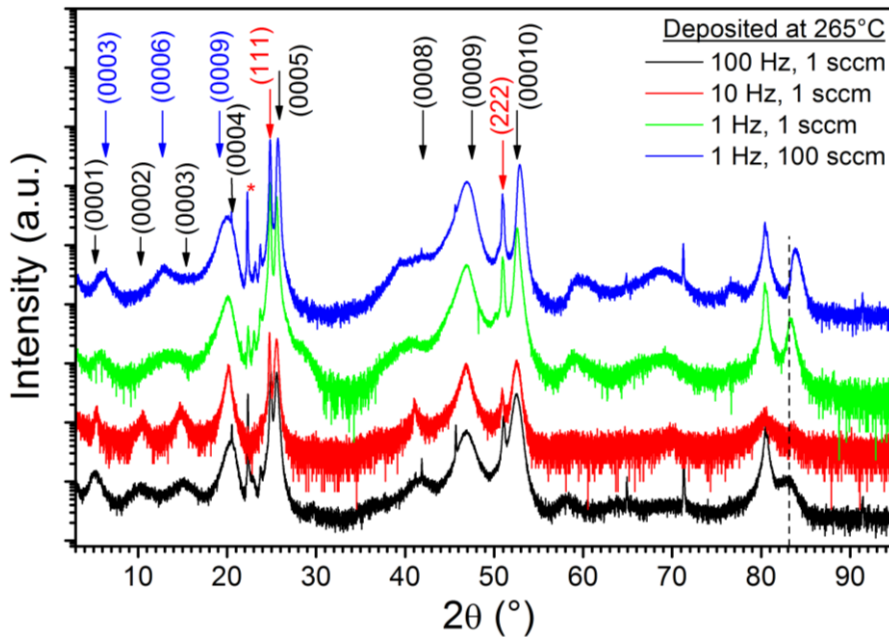


Figure 4-37. 2θ - ω scans for GST films under deposition with varying parameters. Hexagonal positions belonging to the GST225 phase are marked with black and hexagonal positions belonging to the GST124 phase are marked with blue. Substrate contributions are annotated in red.

real cause of the phase transition is probably a temperature effect, since the film spends longer time at the deposition temperature. Perumal et al.^[109] have indeed shown that the GeTe desorption is not constant at high deposition temperatures when deposition time exceeds ~ 20 min. This is explained by the fact that the thermocouple does not directly measure the substrate surface temperature, since a non-contact geometry was employed. In the experiments here, the deposition geometry is analogue, with the thermocouple situated 5 mm below the actual substrate surface and therefore similar effects can be expected. An attempt to balance this time-dependent desorption was made with the introduction of more Ar in the chamber during deposition. A higher background pressure could help to reduce the desorption rate of the film constituents, since more desorbed species could be reflected back to surface. In Figure 4-37, the blue curve represents the film deposited at higher background pressure. As can be seen, it coincides well with the green curve, i.e. a GST124 phase. Hence, it can be concluded that the investigated background pressure is not high enough to affect desorption. In the vacuum system used, higher pressures than that cannot be realized. Furthermore, the blue curve shows sharper peaks compared to the green curve. It could indicate that the high background pressure used is beneficial in reducing the kinetic energy of the most energetic particles in the plasma (which could have kinetic energies of more than hundred eV, see Ref. 125). These high energetic particles are not particularly beneficial for the growth and it is positive if one could reduce their energy.

The transition from the hexagonal 225 phase to the 124 phase was confirmed with EDX measurements presented in Figure 4-38. A significant reduction of the Ge and Te content can be seen in the two films deposited with 1 Hz. The films deposited at 100 and 10 Hz suffer only weakly from Ge and Te loss compared to the target. It implies that in order to reach the optimum deposition conditions, a sufficiently high, but not too high substrate temperature and a sufficiently low, but not too low deposition rate is required.

In-plane XRD profiles show a clear (2-1-10) peak for all films corresponding well with the angular position of the GST225 phase as displayed in Figure 4-39. This is surprising, since the two films deposited with 1 Hz were confirmed to be GST124. The in-plane peaks from these two films differ significantly from the GST124 position^[73]. This illustrates the complexity in determining the crystalline phase of these GST compounds using only one technique. Often, it is the combined impression from all measurements (out-of-plane XRD, in-plane XRD, pole figure analysis and TEM) that gives evidence about the actual

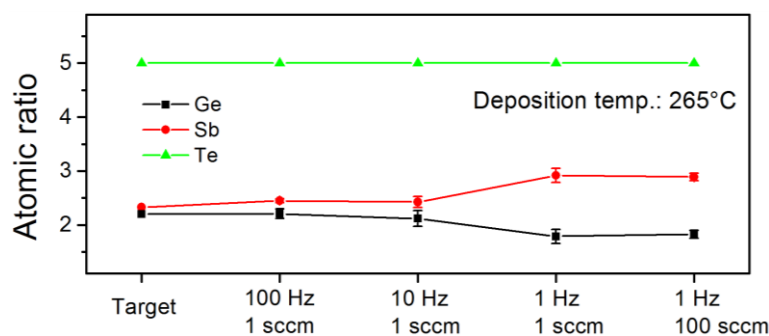


Figure 4-38. Chemical composition of GST films deposited under different experimental conditions as measured by EDX.

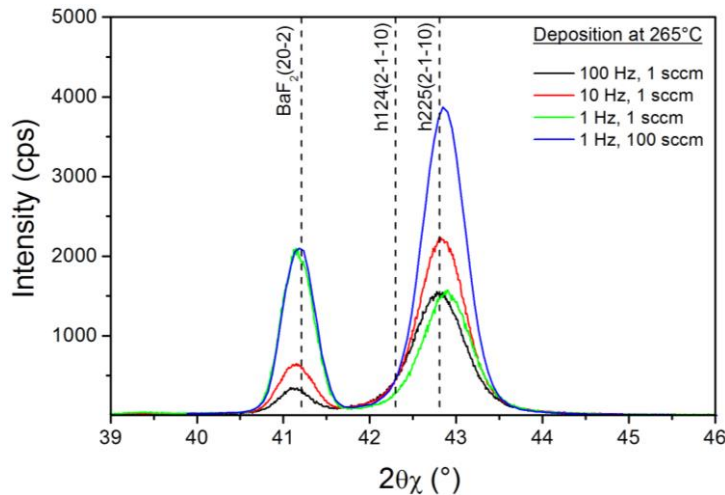


Figure 4-39. In-plane $2\theta\chi$ - ϕ measurements for GST films deposited under different experimental conditions.

phase. Furthermore, it also indicates that the structural models used as references are more useful for comparing the diffraction pattern appearance and not the actual peak positions, since the lattice parameters of these GST compounds probably are sensitive to the exact chemical composition in the films.

In-plane ϕ -scans of the four films are presented in Figure 4-40. All films show a six-fold in-plane symmetry, indicative of an epitaxial film. Not surprisingly, the films deposited at the highest rate (100 Hz) show the broadest FWHM. However, the difference compared to the rest of the films is not that large as in the case of GST on KCl(100), see Figure 4-21. Upon further reducing the deposition rate, the FWHM decreases, showing that the crystallite twist component in the films is reduced down to about 1° , fully comparable with the FWHMs displayed in Figure 4-34. The film deposited at higher background pressure also measures an in-plane rocking curve FWHM in this range.

Finally, measured pole figures of the $\{10-1\}$ planes are presented in Figure 4-41, where l equals 3 and 7 for the GST225 and GST124 phase, respectively. Except for intensity

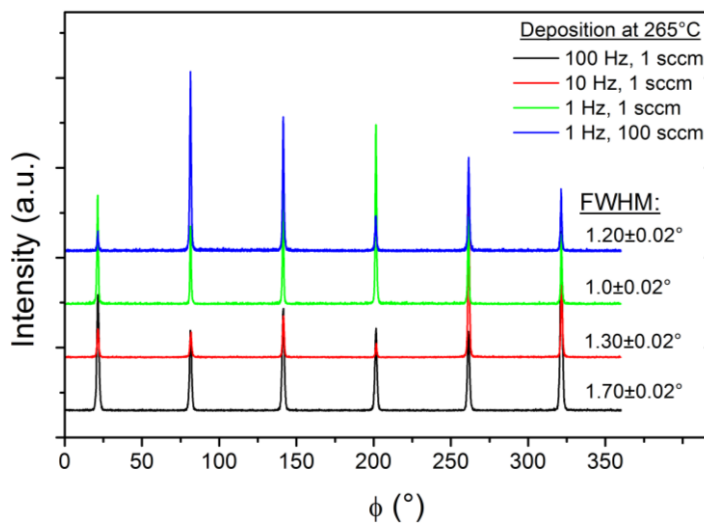


Figure 4-40. In-plane ϕ -scans of the GST $\{2-1-10\}$ reflection for films deposited under different experimental conditions.

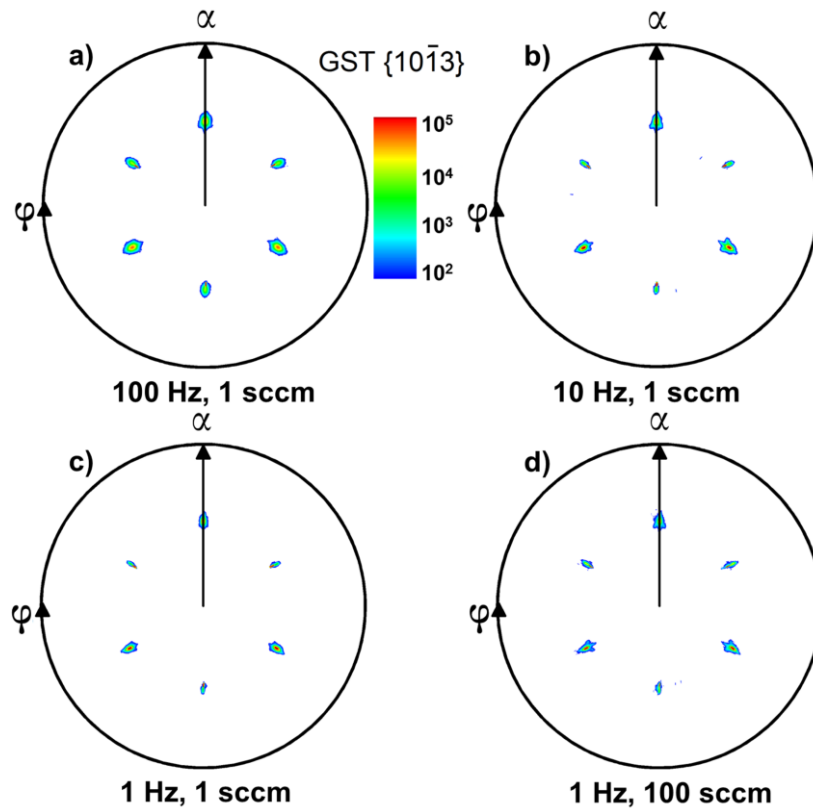


Figure 4-41. Measured pole figures of the GST{10-13} reflections for films deposited under different experimental conditions. Intensity (cps) is shown on a logarithmic scale and applies for all pole figures.

differences, all pole figures are qualitatively the same. This is especially noticeable in Figure 4-36a-c, for the films deposited with different deposition rates but same Ar-flow. The pole density maxima are continuously getting narrower with decreasing deposition rate. The dominating rotational domain is the one oriented as GST[1-210] || BaF₂[1-10]. In Figure 4-41c and d, the intensity ratio is about 100 between the strong and weak maxima. For the same reasons as already mentioned in section 4.3.1, it cannot really be determined, whether there is one single RD or just one largely dominating RD present in the films.

4.3.3. Hints of cubic GST

Until now, all the investigations on the epitaxial growth of GST on crystalline substrates were conducted by heating the substrate to a certain temperature followed by deposition of the film. In parallel with those investigations, some films were deposited at room temperature for further heat treatment in an annealing oven, analogue to the films in Figure 4-6. On top of all films a thin capping layer of LaAlO_x was deposited (10-15 nm). The films were confirmed to be amorphous in the as-deposited state by XRD and were then subjected to a 30 min heat treatment with 10 min heating ramp to the desired temperature. In Figure 4-42, a 2θ-ω scan overview of four samples is presented. The angular range spans over 3 diffraction orders. The black curve represents a film that was annealed at 150°C. No evidence of crystalline content can be seen. This is in agreement with the polycrystalline films in Figure 4-6, where no crystalline content is found below 165°C. At 180°C (red curve), however, a clear diffraction peak is present. This is especially visible at the GST(222) marker in the figure. Upon a further annealing temperature increase the

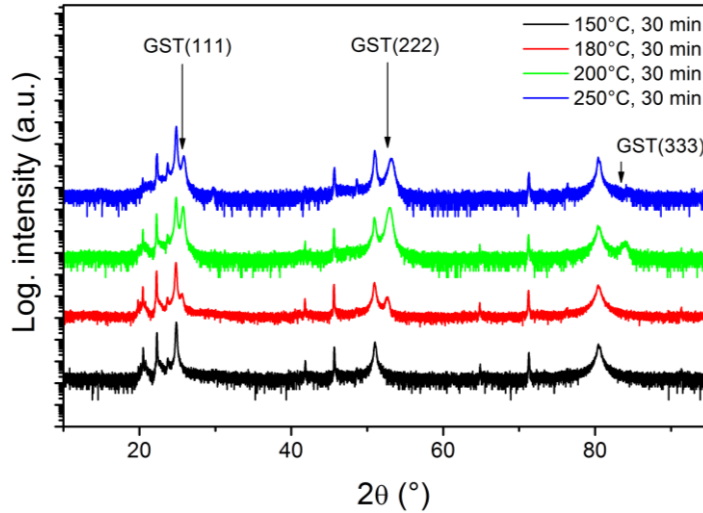


Figure 4-42. Wide 2θ - ω scans for GST films annealed at different temperatures. Cubic phase reflection positions of GST225 are marked with black. All other peaks stem from the substrate.

peak gains in intensity and now even the third diffraction order is clearly discernable. Noticeable is that no diffraction peaks below $2\theta \approx 25^\circ$ can be seen, except those of the substrate. This means that a cubic GST phase has been obtained with the (111) planes aligned with the $\text{BaF}_2(111)$ planes. At even higher annealing temperatures the GST(hkl) peaks remain but lose in intensity.

A closer inspection of the GST(111) peak is presented in Figure 4-43. The diffraction peaks inside the dashed box all stem from the substrate. The black dashed line indicates the position of cubic GST225 as proposed by Matsunaga^[62]. The film annealed at 180°C coincides well with that position, but with increasing annealing temperature the (111) peak shifts to higher diffraction angles. This cannot be explained by a phase transition to the cubic GST124 phase since that would shift the peaks in the other direction (GST124 has a larger unit cell)^[73]. Moreover, the films were deposited at room temperature so there should be no residual stress in the films arising from a thermal lattice misfit during deposition. The capping layers also prevent any desorption from the films in the annealing oven, ruling out compositional change as an explanation for the peak shift. However, since the polycrystalline films presented in Figure 4-6 also in general show a larger 2θ value for the (111) planes compared to the Matsunaga model^[62], it could just reflect the fact that the film annealed at 250°C has begun to transform to a polycrystalline film. Indeed, at the highest annealing temperature a weak sign of a GST(200) reflection can be found, indicating that this temperature promotes polycrystalline crystallization instead of epitaxial (that the films are really epitaxial will be shown by φ -scans on page 77). This could also be the reason why the diffraction intensity is reduced between 200°C and 250°C . It also demonstrates that there is a very limited temperature range where annealing induced-epitaxy is found. Interestingly, results from other groups show an opposite behavior. Bragaglia et al.^[103] investigated the crystallization behavior upon annealing of MBE-deposited amorphous films. Already at a temperature of 135°C , first hints of a hexagonal phase are revealed and at an annealing temperature of 230°C a fully hexagonal pattern can be seen. The authors did, however, not use a capping layer so that a compositional drift from the 225 to 124 composition occurred simultaneously. This is probably the driving force for

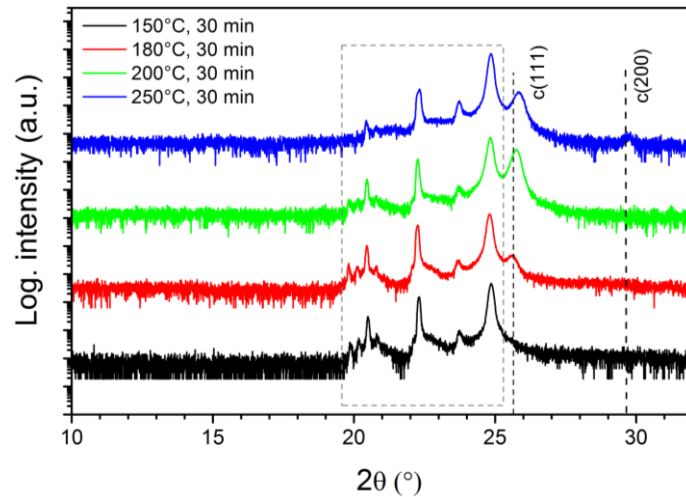


Figure 4-43. Detailed 2θ - ω scans around the GST(111) reflection for films annealed at different temperatures. Cubic positions of GST225 are marked with black. The peaks inside the dashed grey box stem from the substrate.

the formation of the hexagonal phase in their case and could account for the discrepancy between their results and those presented in the present study.

The lateral lattice parameter was determined by in-plane $2\theta\chi$ - φ measurements as presented in Figure 4-44. A GST peak is observed for all films fairly close to the position of the cubic GST(20-2) reflection. This is especially noticeable for the film annealed at 250°C, i.e. the more polycrystalline film. Combining the in-plane lattice parameter (in agreement with the Matsunaga model) with the 2θ -value of the (111) peak (not in agreement with the Matsunaga model, [111] slightly compressed), the resulting structure is not perfectly cubic but compressed along the [111] direction, i.e. a rhombohedral distortion along this direction is present in the films. This is known for IV-VI crystals (for instance GeTe) as a Peierls distortion^[50] and has experimentally also been observed for GST by extended x-ray absorption fine structure measurements as shown by Kolobov et al.^[34] For the two films annealed at 180°C and 200°C, the in-plane lattice parameter is expanded, which implies that the films are not fully relaxed, but a small substrate induced lattice strain is present.

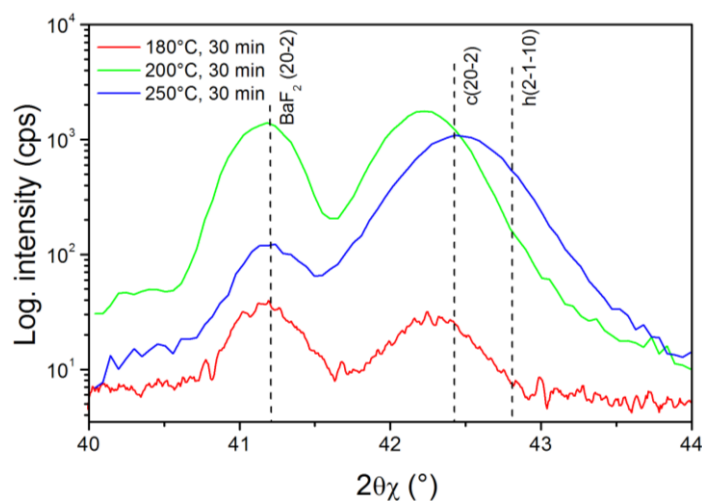


Figure 4-44. In-plane $2\theta\chi$ - φ measurements for GST films annealed at different temperatures.

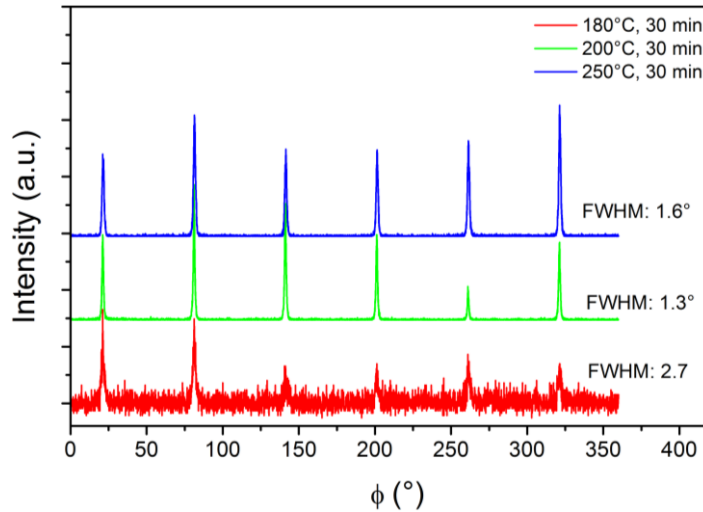


Figure 4-45. In-plane φ -scans for GST films annealed at different temperatures.

In-plane φ -scans of the $\{20\cdot 2\}$ planes show a six-fold in-plane symmetry for all films as presented in Figure 4-45. This is already a good indication that the films are epitaxial and not only possess a $[111]$ fiber texture. The FWHM of the in-plane rocking curve is quite narrow as displayed in the figure. The film annealed at 200°C actually shows a comparable FWHM with those of the epitaxial films presented in Figure 4-34, section 4.3.1, indicating similar crystalline quality.

This is further illustrated in Figure 4-46, where traditional φ -scans of the $\{200\}$ planes are shown. For comparison an epitaxial hexagonal film deposited at 265°C is also displayed. For this film the hexagonal $\{10\cdot 13\}$ planes were scanned, i.e. the hexagonal analogue planes to the cubic $\{200\}$. Beginning with the film annealed at 180°C , only six weak peaks can be seen (red curve) plus three overlapping very narrow peaks at $\varphi=100, 220$ and 240° . The narrow peaks stem from the substrate and are also present in the blue curve on top of the strongest peaks. For the films annealed at 200°C (green) and the reference film (black) the substrate contribution completely vanishes in the strongest peaks and cannot be discernable anymore. The diffracted intensity of the film annealed at 200°C is not even a factor 5 smaller than the hexagonal epitaxial reference film, indicating that the two films are of similar crystalline quality. The film annealed at 250°C has a factor 10 lower intensity and the peaks are significantly broader, evidencing the detrimental effects of too high annealing temperature. The fact that six peaks are visible indicates that a 180° twin domain is present in the films, since a cubic single crystal should only diffract the $\{200\}$ planes three times for a (111) oriented sample. The presence of twins in (111) oriented cubic GST epitaxial layers on (111) substrate planes has been confirmed by Perumal^[69]. In their case an almost 1:1 ratio between the two rotational twin domains was found, whereas the ratios found here are significantly higher. This is displayed in Table 6 as the intensity ratio between the strongest peaks and the weakest peaks in each film in Figure 4-46. At an annealing temperature of 180°C , the ratio is about one indicating that the twin orientations exist in parity. At 200°C , the ratio is roughly twelve, very close to that of the reference film (roughly eleven), indicating a strongly dominating rotational domain orientation. At 250°C , the ratio is once more reduced, a process related to the formation of more

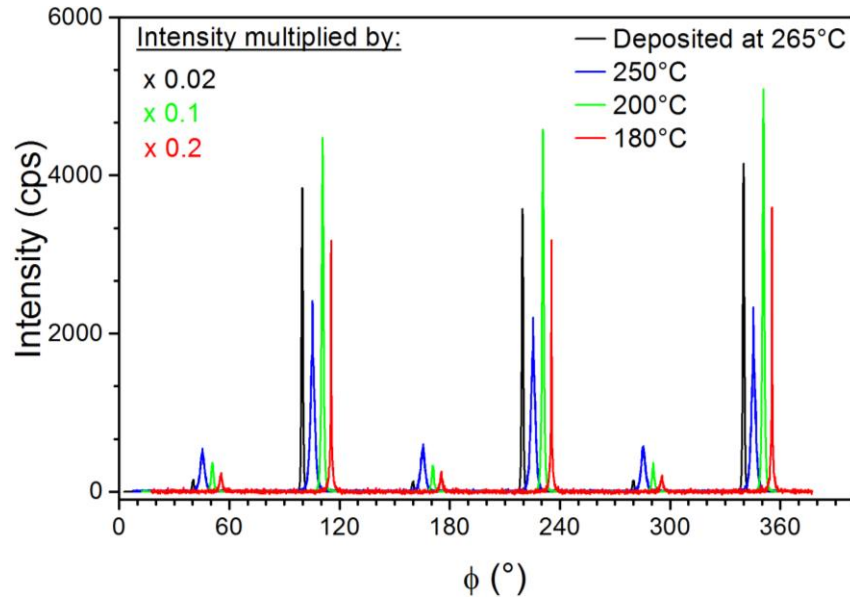


Figure 4-46. GST{200} φ -scans for films annealed at different temperatures. The black curve is an epitaxial reference film. The black curve is displayed at the correct φ -position, whereas all subsequent films are shifted by 5° in φ for display purposes. No offset in the y-direction is present. The intensity for the reference film (deposited at 265°C), the film annealed at 200°C and the films annealed at 250°C has been divided by 50, 10 and 5, respectively, so that all films can be presented on the same y-scale.

polycrystalline content in the film. Considering these results it is shown that the annealed films crystallize in an epitaxial way with a cubic GST structure.

Finally, to prove that the films are indeed cubic, φ -scans of the hexagonal {10-16} planes were recorded. The {10-16} planes are only present in the hexagonal structure and the closest cubic planes with similar tilt angle is the $\text{BaF}_2\{220\}$ which lies more than 1.3° away in 2θ . The results are presented in Figure 4-47 for the three films annealed at 180°C , 200°C and 250°C . Additionally, two reference films are plotted in the same diagram, one being a high quality hexagonal film and one being a low quality hexagonal film. The three annealed films show all very similar patterns with three peaks at $\varphi \approx 75, 195$ and 315° . These peaks stem from the substrate, i.e. $\text{BaF}_2\{220\}$. In comparison, the two confirmed hexagonal films show a completely different pattern. Now six peaks are present, whereby every second peak is much stronger. The film deposited at 265°C especially shows high intensities. In fact, it has been reduced by a factor of ten and it can still not be fitted in the graph. Compared with Figure 4-46, where the annealed film at 200°C and the same reference film show similar intensities, it now differ orders of magnitude. This shows in an unambiguous way that the films grow with a cubic structure.

Table 6. Intensity ratio between the strongest and weakest {200} peaks

	180°C	200°C	250°C	Deposited at 265°C
$I_{\text{strong}}/I_{\text{weak}}$	~1	~12	~4	~11

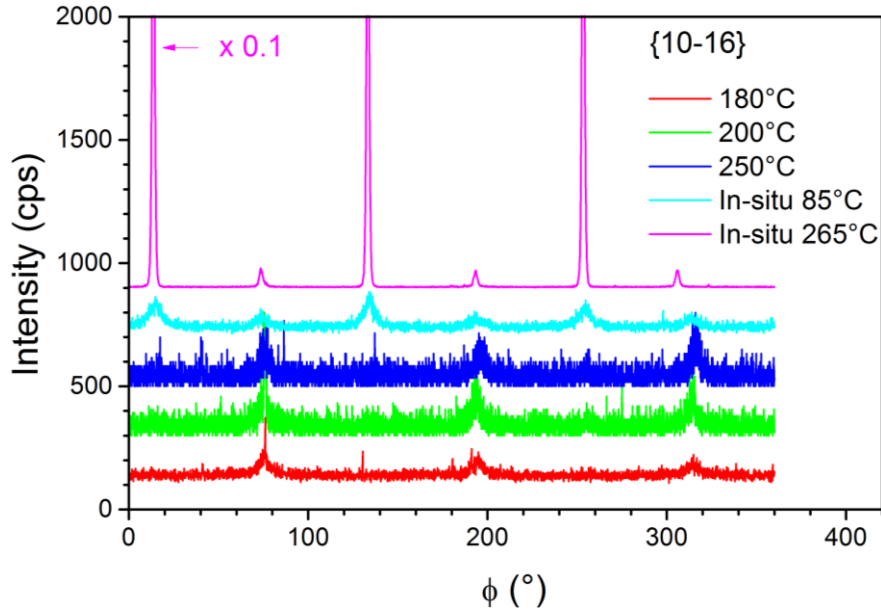


Figure 4-47. GST {10-16} scans for films annealed at different temperatures. The cyan and purple curves are from hexagonal epitaxial reference films. The intensity of the purple curve has been divided by ten.

4.3.4. Summary of the results on the deposition of GST on BaF₂(111)

In this section the growth of GST films on (111) oriented BaF₂ substrates was investigated. Mainly, the effect of substrate temperature was investigated. The growth is characterized by one out-of-plane (0001) orientation. This is different to the case of KCl(100) substrates where three out-of-plane orientations were present in the films. The films grow epitaxially already at a substrate temperature as low as 85°C with no observable polycrystalline growth. The in-plane orientation is characterized by two rotational twin domains at substrate temperatures below 210°C. The high symmetry directions in the GST film and substrate are aligned, i.e. GST[-12-10] || BaF₂[1-10] and GST[1-210] || BaF₂[1-10]. Above 210°C the latter orientation dominates the growth.

Using a higher deposition rate deteriorates the crystal quality weakly, whereas a low deposition rate combined with a high substrate temperature promotes Ge and Te desorption and a transition to the GST124 phase. A high background pressure ($4 \cdot 10^{-3}$ mbar) during deposition does not prevent this desorption from taking place.

Amorphous films deposited at room temperature on BaF₂(111) which were subsequently annealed *ex situ* possess a cubic crystal structure without no traces of the hexagonal phase. At an annealing temperature of 200°C the highest crystalline quality was obtained.

4.4. Epitaxial growth of GST on Si(111)

In this section the growth of GST films on Si(111) will be presented. Si is a standard material in the semiconductor industry and the possibility to deposit epitaxial GST films on this material with a high deposition rate could be of great interest. Even though there is a large lattice mismatch between Si and GST (-10.8%), high quality GST epitaxial layers have already been shown to be possible with MBE^[24,69]. However, the growth rates in these cases are typically very low (0.1-0.3 nm/min). Here, two experimental series were investigated. The first one without a thermal pre-treatment of the substrates, meaning that the substrates were pre-cleaned as described in section 3.2.1 and then only pre-heated at the desired substrate temperature. This will be referred to as a non-thermal pre-treatment. In the second experimental series the substrates were thermally pre-treated, also described in section 3.2.1, meaning that the substrates were pre-cleaned and then subjected to a high temperature for 10 minutes before cool down to the desired deposition temperature. This will be referred to as a thermal pre-treatment. The parameters in common for these investigations are presented in the following table.

Table 7. General deposition conditions on the growth of GST on Si(111)

No. of pulses	Frequency (Hz)	Nominal deposition rate (nm/min)	Fluence (J/cm ²)	Ar-pressure (mbar)
7200	2	~2	0.8±0.2	4·10 ⁻⁵

4.4.1. The growth of GST on non-thermally pre-treated Si(111)

A set of films were deposited at different substrate temperatures spanning the range between 110°C to 295°C. Each substrate had been pre-cleaned as described in section 3.2.1 and was subsequently directly pre-heated at the desired substrate temperature for at least 30 minutes in order to reach a relatively stable surface temperature. In Figure 4-48a-d, SEM images at high magnification of films deposited at different temperatures are presented. As can be seen, the films look relatively smooth. Occasionally, some hints of crystallites can be seen (in Figure 4-48a and c) which seem to align according to a hexagonal pattern. This is especially visible in Figure 4-48c. The overall impression is that the topography is similar but a little more rough than the GST films on BaF₂(111).

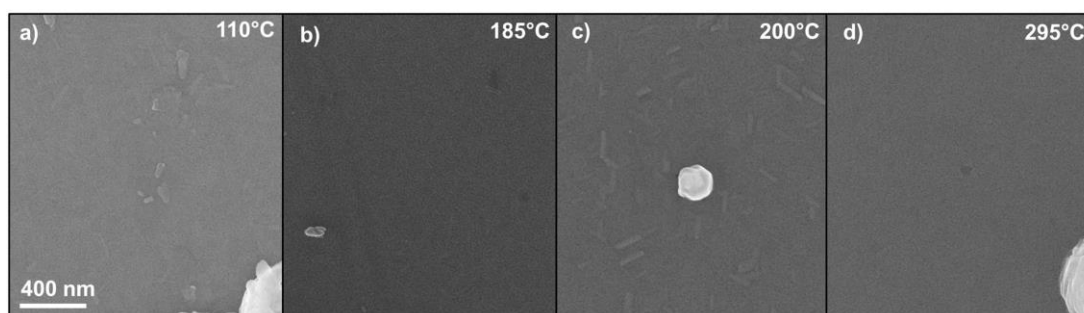


Figure 4-48. SEM images of GST films deposited on non-thermally pre-heated Si(111) at different temperatures.

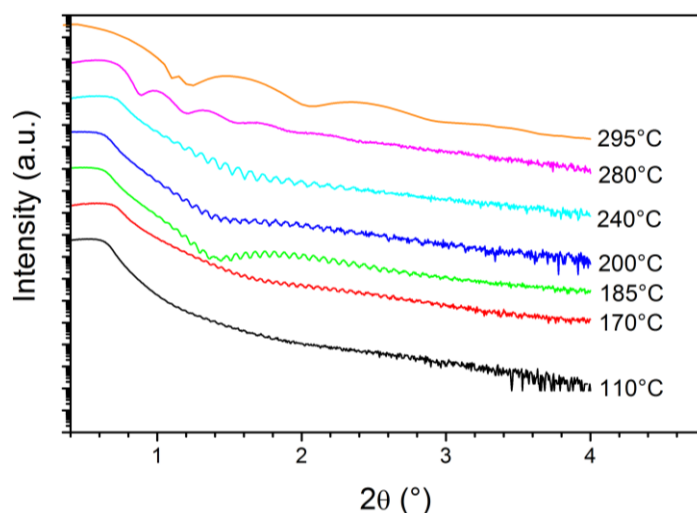


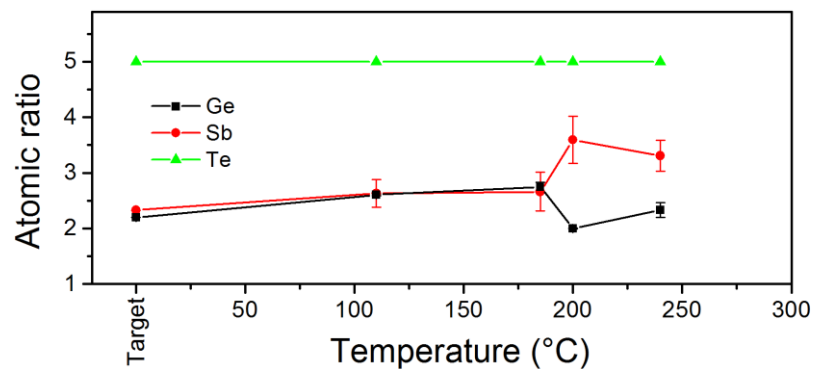
Figure 4-49. XRR measurements of GST films on non-thermally pre-heated Si(111) deposited at different substrate temperatures.

To determine the roughness more quantitatively, XRR measurements were conducted for all films in this series. The resulting curves can be found in Figure 4-49. For the film deposited at 110°C, the oscillation fringes are barely visible indicating a rough surface. The film thickness measures ~ 150 nm. Surprisingly, the surface roughness and interfacial roughness is high, around 2-3 nm. At this temperature this is an unexpected result, but could be related to the fact that oscillations are barely visible and therefore the error in fitting the curve could be larger. By increasing the substrate temperature, the thickness is reduced monotonically up to 240°C. In this temperature range an average film thickness of 100 nm can be estimated so that the average deposition rate amounts to ~ 1.7 nm/min. At the two highest substrate temperatures the thickness drops radically as seen by the wide oscillating periods. The density of the films varies between 6.1–6.3 g/cm³ with no apparent temperature dependence. This is in good agreement with high-quality bulk GST^[126] and perfect single crystals^[65] considering the accuracy in the fitting method (± 0.1 g/cm³) and the fact that it is not bulk material but thin films. The extracted data from the XRR measurements are presented in Table 8. The presence of a surface oxide layer can be detected in all films. A large thickness spread of this layer among the films can be noticed in the first data column. However, the variation in oxide layer thickness is not related to the deposition temperature, but only reflects how long the films were exposed to air before they got measured (compare Figure 4-4). The fitted roughness values (surface and interface) scatter largely between 1-2 nm without any obvious correlation to the substrate temperature. The absolute values tend to be larger than for polycrystalline films (see Figure 4-5). Interestingly, rms values as high as 5.8 nm are normal for MBE deposited GST films on Si(111) as presented by Perumal^[69] and compared to that, the measured rms values here are even slightly lower. Furthermore, the epitaxial GST films prepared by MBE consist of large trigonal shaped crystallites protruding from the surface, whereas this is only observed occasionally in this work, see Figure 4-48a and c. Hence it can be concluded that the films show a relatively smooth topography without any substrate temperature dependent roughness increase.

Table 8. Extracted data from the XRR measurements in Figure 4-49.

Temperature (°C)	Thickness GST (nm)	Thickness Oxide (nm)	rms interface (nm)	rms surface (nm)
110	148	0.1	2	3.3
170	143	1.8	1.1	1.7
185	118	3.5	1.2	1.8
200	117	3.3	1.5	1.8
240	89	2.3	1.3	2.2
280	19	0.9	1.8	1.1
295	8.4	0.8	1.0	2.8

Since the thickness reduction is quite dramatic for the films upon raising the substrate temperature, one could expect that there could be large differences in composition between the films. Therefore, EDX spectra were recorded for the films. The result is presented in Figure 4-50. Noticeable are the larger error bars in the Sb group compared to previous measurements on KCl and BaF₂. This is due to the fact that in order to evaluate Ge properly (Ge K α \approx 10 keV), an acceleration voltage higher than 20 kV is needed. In using such a high voltage, a very intense signal from the Si substrate is simultaneously acquired. The signal is in fact so strong that also the double energy pulse peak of Si K α partly overlaps with the Sb L series which is used for the evaluation. Nevertheless, the trend already observed for GST deposition on KCl and BaF₂ substrate is visible here, too. With increasing substrate temperature, a small loss of Te is evident and at higher temperatures desorption of mainly Ge and Te can be seen. The measurements could only be conducted for films deposited at or below 240°C, since at higher temperatures the film thickness was too low to obtain any reliable signal. A sound assumption, though, is that desorption of Ge and Te continues. Although the general trend is similar as for GST deposition on KCl and BaF₂ substrates, the absolute temperature for the heavy desorption onset is quite different and about 50-80 degrees lower for Si. One can think of two reasons for this behavior. Firstly, there could be a chemical effect. The GST films may not be so strongly bonded to the Si substrate compared to the halogen containing ones. Alternatively, the calibrated temperature in section 3.2.1 is not valid for this deposition series. Of the two reasons, the latter is the most probable one. This is motivated by the fact that the

**Figure 4-50.** Composition of GST films on non-thermally pre-heated Si(111) deposited at different substrate temperatures as measured by EDX.

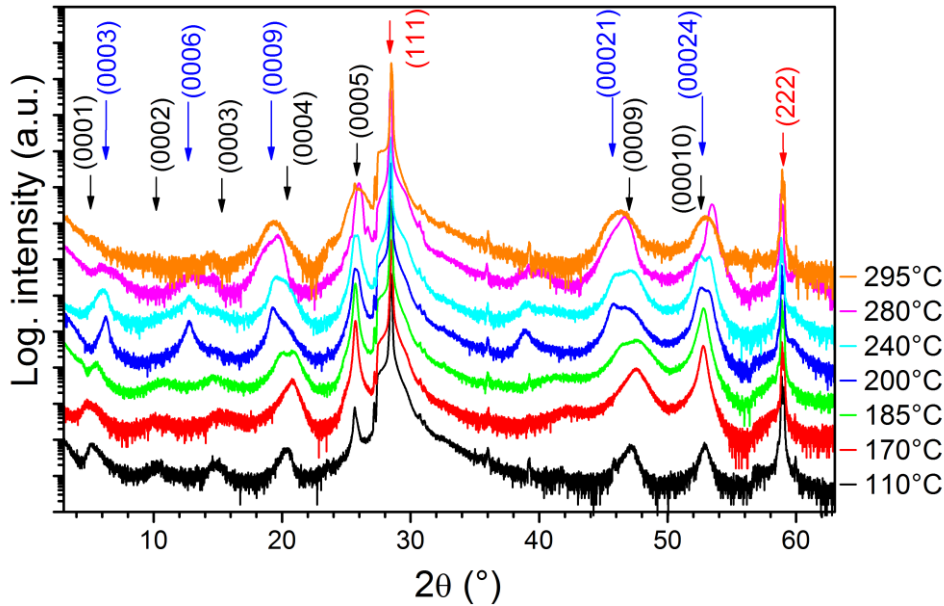


Figure 4-51. 2θ - ω scans for films deposited at different substrate temperatures on Si(111). Hexagonal phase reflection positions of the GST225 and GST124 are marked with black and blue, respectively. Substrate contributions are annotated in red.

films were deposited with 2 Hz and 7200 pulses, i.e. one hour total deposition time. Add to that the 30 min pre-heating and the total time at the deposition temperature sums up to 90 minutes. As discussed already, Perumal et al.^[109] could show an increase in Ge and Te desorption even though the heating temperature and the thermocouple readings were constant. This shows once more the complexity in depositing stoichiometric GST films.

The loss of Ge and Te is further visualized in the 2θ - ω scans in Figure 4-51. Firstly, all films are hexagonal based upon the presence of diffraction peaks below $2\theta=25^\circ$. Secondly, only $(000l)$ reflections are visible indicating a single growth direction. The three films deposited at the lowest temperature show a diffraction pattern corresponding to the GST225 composition as annotated by the black arrows. In fact, already for the film deposited at 185°C (green curve) the onset of a peak splitting is observed for the (0004) peak. The exact position deviates slightly from the Matsunaga^[62] model but are comparable with the GST films on $\text{BaF}_2(111)$. Above 185°C , the GST124 composition dominates the growth as seen from the good agreement with the blue annotations. The films are probably not phase pure since there are double peaks present at the (0004) , (0009) and (00010) angular position all the way up to a substrate temperature of 280°C . At the two highest substrate temperatures a single (00024) peak is observed, indicating a full transformation to GST124. It is worth mentioning again that the film thickness is only 19 and 8 nm for these two films and the fact that they are still measurable indicates a very high degree of crystalline ordering in the films.

The FWHM and angular position of the (0005) diffraction peak is displayed in Figure 4-52. A small increase of the FWHM can be seen (black curve), which indicates smaller crystallites as the temperature is increased. This is unexpected but interesting, since a higher temperature in general promotes grain growth. Possibly, this has to do with the significantly decreasing film thickness. This is especially noticeable for the two data points

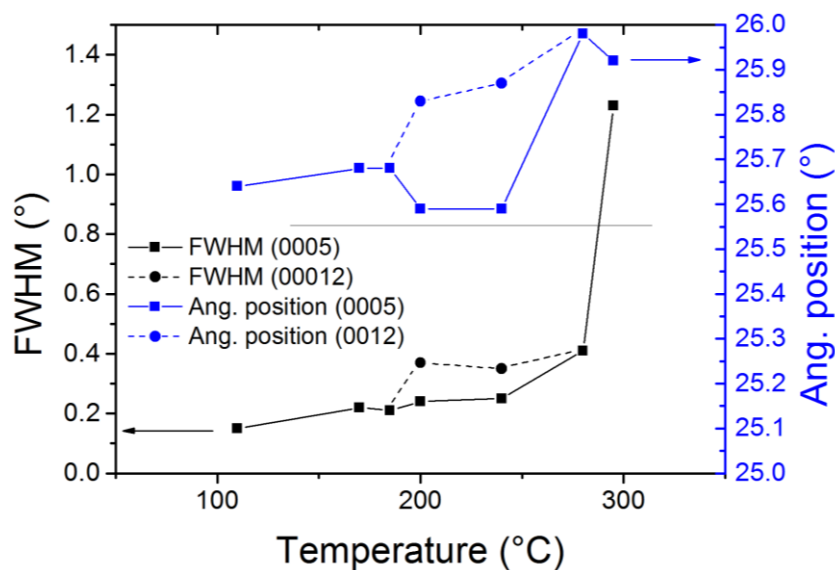


Figure 4-52. FWHM and angular position of the GST(0005) peak for GST films deposited at different substrate temperatures on non-thermally pre-treated Si(111).

at 280°C and 295°C which show a much larger FWHM. This makes sense considering that the film thickness is only 19 and 8 nm, respectively. Also the observed peak splitting is visualized in the diagram, where the two data points connected by dashed lines symbolize data measured from the observed GST124(00012) peak. As recalled, the same behavior was found for the deposition of GST on BaF₂(111) in Figure 4-30. The large increase in diffraction angle for the GST124(00012) reflection seems to stop at a 2θ value of about 25.9°. This is roughly 0.3° higher than the theoretical value (25.64°) and it indicates a compression of the films of about 1%. A substrate induced strain does not make sense, since that would compress the films in the in-plane direction and hence, due to the Poisson ratio, an elongation in the out-of-plane lattice parameter would result. More probably, it just reflects the actual chemical composition in the films which is not that of a perfect stoichiometric GST124 phase.

The out-of-plane rocking curves for the (0005) (or (00012)) peak show two contributions, one extremely narrow and one broad peak as displayed in Figure 4-53a. The broad peak looks similar as in the case of GST on BaF₂(111), see Figure 4-31, confirming a small angular distribution along the growth axis. In that case the narrow peak in the middle of the rocking-curve could not be separated from the substrate contribution due to the small angular separation in 2θ for the GST(0005) and BaF₂(111) peaks. The narrow peaks in the center of the rocking curves in Figure 4-53a do however stem from the films. That statement is based upon the fact that the Si(111) reflection lies more than 2.8° away in 2θ and a 0.15 mm Ni-filter was used to reduce the Cu K _{β} intensity which could further influence the measurement. Additionally, selected films were measured on a high-resolution x-ray diffractometer with a parallel Cu K _{α} 1 x-ray beam. The same pattern was obtained with that machine only with reduced intensity. This is displayed in Figure 4-53b (red curves). Also, the corresponding two 2θ - ω measurements are presented (black curves) to show that the intensity matches 1:1 between the measurements. The substrate temperature dependent FWHM evolution of the films is shown in the inset of Figure 4-53a. As can be seen two curves are shown, where the black squares represent the broad base peak and the red

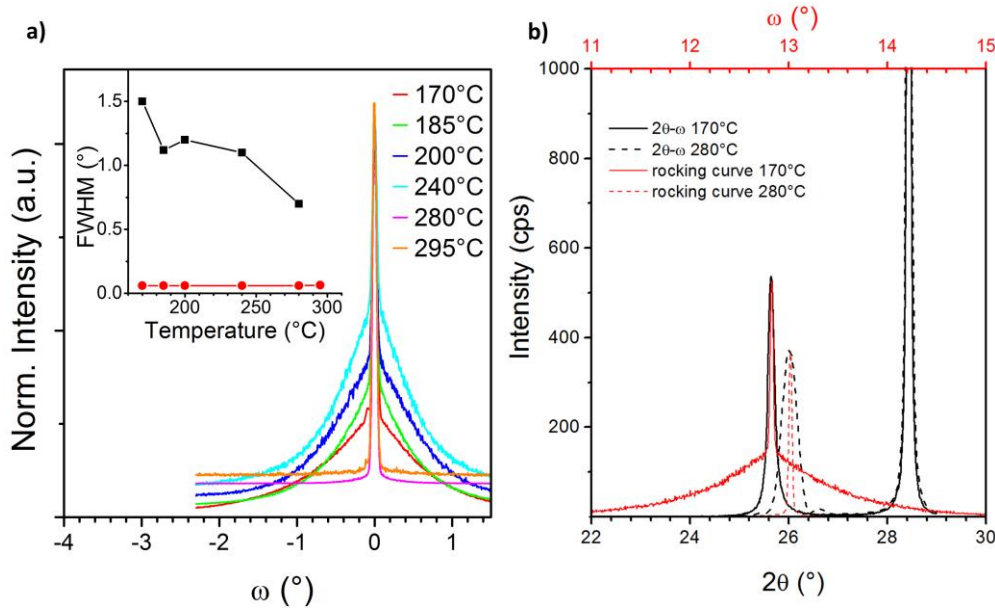


Figure 4-53. Rocking curve measurements (ω -scans) of the GST(0005) peak for GST films on non-thermally pre-treated Si(111) deposited at different substrate temperature (a). In (b), 2θ - ω scans and the corresponding ω -scans of selected GST films measured on a high-resolution diffractometer.

circles represent the narrow peak. The FWHM is getting narrower with increasing temperature for the broad peak, while the narrow peak seems to be completely independent on substrate temperature. The FWHM of this peak measures roughly 0.04° , a very low value compared to the deposition of GST on KCl(100) or BaF₂(111). However, one could suspect that the values obtained for the rocking curve FWHM on BaF₂(111) are smaller than those actually reported.

Pole figure measurements of the GST{10-1} peaks reveal the epitaxial nature of the films. Depending on the actual phase l is either 3 or 7 for GST225 or GST124, respectively. However, the measurements were conducted at the same angular position since the two reflections only differ by 0.4° and this is fully within the acceptance window for 2θ during the measurements. In Figure 4-54a, the film deposited at 170 $^{\circ}$ C is presented. Six, i.e. two times three pole density maxima are present. The six pole density maxima are uniform in intensity and therefore indicate two rotational twin domains of equal quantity and quality as indicated by the two equally intense triangles overlaid in the figure. A polycrystalline part also exists in the film as evidenced from the ring intensity pattern between the pole density maxima. Additionally, three substrate-related pole density maxima are encircled in red at higher α angles. These substrate contributions come from the small Cu K $_{\beta}$ fraction that is still present in the x-ray beam and can be neglected. For the films deposited at 280 $^{\circ}$ C, the polycrystalline ring pattern has disappeared. It could be argued that the polycrystalline part is not to be seen due to the low thickness of this particular film, but the situation looks very similar for all other films in the investigated range, i.e. above 170 $^{\circ}$ C the films are exclusively epitaxial. This is evidenced from the six pole density maxima evenly distributed at $\alpha \approx 58^{\circ}$. The pole density maxima have a more symmetric spatial distribution than for the films deposited on BaF₂(111), i.e. the crystallite twist and tilt distribution is more according to a normal distribution. Furthermore, the intensity is not equal among the pole density maxima, i.e. one rotational twin dominates. However, the

effect is not as pronounced as in the case of GST deposition on $\text{BaF}_2(111)$, where intensity ratios of more than 10:1 were observed between the strongest orientation and the weakest, see Table 6. In this case the ratio is around 3:1. Nevertheless, this ratio is still a little bit higher than the 1:1 ratio of MBE deposited epitaxial GST films on $\text{Si}(111)$ ^[69], showing that the PLD-process is suitable as a high quality film deposition method.

In Figure 4-54c and d, two in-plane Reciprocal Space Maps (ipRSM) are shown of the same two films. An ipRSM offers a good overview of the different in-plane orientations in the sample, but is in this case not intended as a high resolution measurement. The axes in the image are aligned along the high symmetry directions of the underlying Si substrate, i.e. $\text{Si}[2-20]$ and $\text{Si}[22-4]$, and intensity is plotted on a logarithmic scale. The Si substrate reflections are annotated in red. The GST peaks are all annotated according to the hexagonal GST225 phase. The polycrystalline pattern in Figure 4-54c is readily observable with

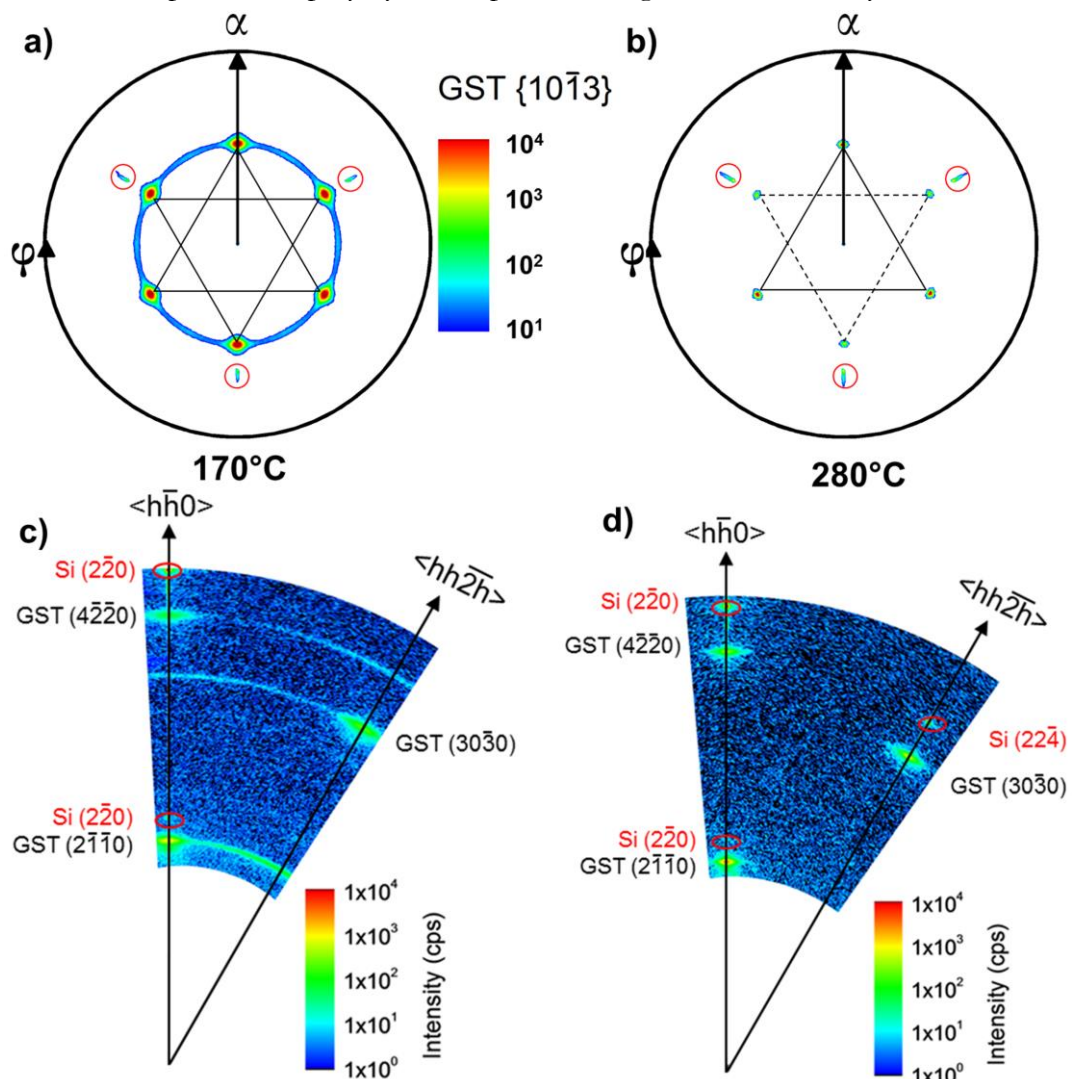


Figure 4-54. Pole figure measurements (a and b) of the GST{10-13} planes of GST films on non-thermally pre-treated $\text{Si}(111)$. In a), the film was deposited at 170°C and in b) 280°C. Substrate contributions are annotated with red circles and major (minor) crystallite orientations are marked with the solid (dashed) triangles. Intensity is depicted on an in common logarithmic scale.

In-plane reciprocal space maps for the same two films (c and d). Substrate reflections are marked in red. Intensity is depicted on a logarithmic scale.

no other unsuspected orientations showing up. In Figure 4-54d, the polycrystalline pattern is gone and only sharp reflections can be seen. For both films the reflections are aligned along the Si substrate directions evidencing the epitaxial nature of the film. The epitaxial relationship for the strongest rotational twin domain is determined to be $\text{GST}[2-1-10] \parallel \text{BaF}_2[1-10]$, i.e. same as in the deposition of GST on $\text{BaF}_2(111)$.

To analyze the in-plane lattice parameter more in detail, in-plane $2\theta\chi$ - φ measurements along the Si[h-h0] direction were conducted. The result is presented in Figure 4-55. All films show diffracted peak intensity maxima in between the positions of the two hexagonal phases GST225 and GST124. The peak of the film deposited at 170°C is more shifted towards the GST225 peak position and this is expected, since it also showed a GST225 diffraction pattern in the out-of-plane measurements (Figure 4-51). The same argument can be used to explain that the other films in the experimental series originate peaks shifted more towards the GST124 phase. The blue and cyan curves in the graph are noteworthy, since they belong to the films deposited at the highest temperature, i.e. lowest thickness. This shows once again that in-plane diffraction measurements are an effective additional tool for structure clarification, especially for thin layers.

The corresponding in-plane φ -scans of the $\{2-1-10\}$ peak are presented in the left part of Figure 4-56. All films show the expected six-fold in-plane symmetry. For the film deposited at 170°C, the polycrystalline contribution can be seen as the raised intensity between the sharp peaks. The FWHM of the sharp peaks is displayed in the right part of Figure 4-56. The overall trend implies a reduction of the FWHM with increasing substrate temperature, i.e. the crystallite twist is reduced. The absolute values of the FWHM are comparable with the ones for GST on $\text{BaF}_2(111)$ in Figure 4-34, i.e. in between 1.2 to 1.5° for the highest substrate temperatures. Hence, it can be concluded that non-thermally pre-treated Si(111) is suitable as a substrate for the epitaxial growth of GST. This is of course

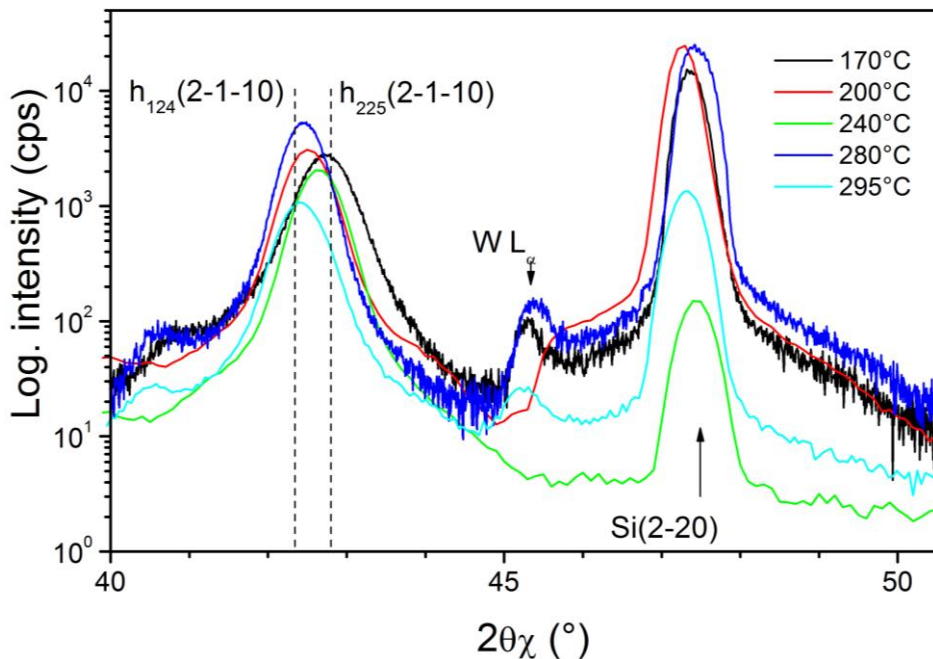


Figure 4-55. In-plane $2\theta\chi$ - φ measurements of GST films deposited at different substrate temperatures on non-thermally pre-treated Si(111).

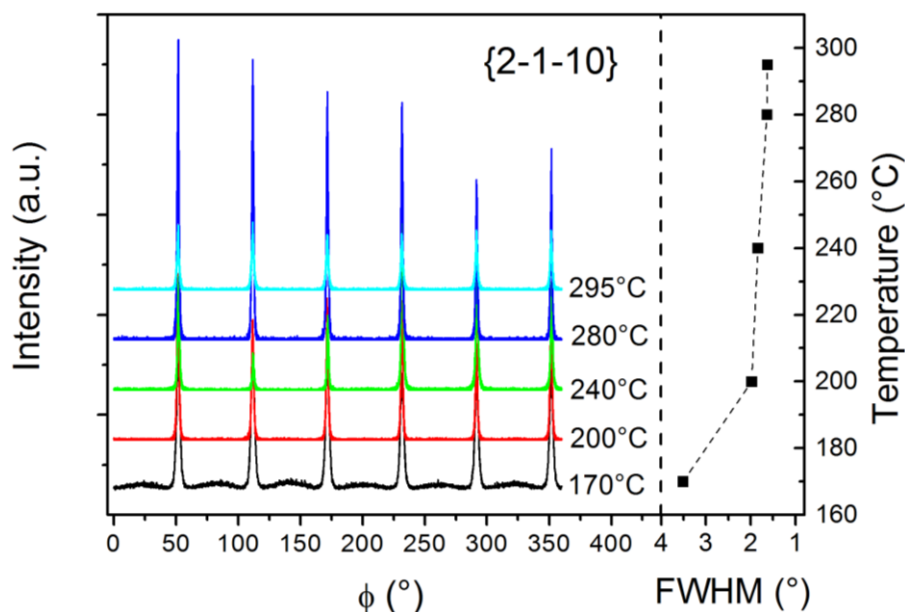


Figure 4-56. In-plane ϕ -scans of the GST{2-1-10} reflection for GST films deposited at different substrate temperatures on non-thermally pre-treated Si(111).

also good for a potential industrial application where a time-consuming and therefore costly heat-treatment prior to deposition is unwanted.

4.4.2. The growth of GST on thermally pre-treated Si(111)

In this section the effect of a thermal heat-treatment of the Si substrates will be discussed briefly. The Si(111) substrates were pre-cleaned in the same way as the ones in the previous section, but now the substrates were rapidly heated up to 1050°C with the aim to induce a Si 7x7 surface reconstruction which is suitable for epitaxial growth. Details about the heat treatment can be found in section 3.2.1.

In Figure 4-57, SEM images of three films deposited at different substrate temperatures are depicted. A large difference in topography is obvious compared to the films that were not thermally pre-treated. In fact, the topography is not comparable with anything previously described in this work. Large crystallites of trigonal symmetry are visible in every one of three images. The crystallite size ranges from 100 up to 600 nm. This is especially visible in Figure 4-57c, where large flat crystallites cover the whole image. A comparison with topography investigations of MBE deposited GST films on Si(111) shows very similar structures^[69] and also with hexagonal GST films deposited with MOCVD^[56,127]. This is the first indication that the heat-treatment has affected the substrate surface and hence also the subsequent growth of GST. EDX measurements show no large deviation, however, from the already observed general trend. This is also expected, since the desorption behavior is mainly governed by the substrate temperature during deposition and the heat treatment does not have any influence on that. As displayed in Figure 4-58, Ge and Te seem to desorb at higher substrate temperatures with a strong desorption onset around 200°C, comparable with Figure 4-50.

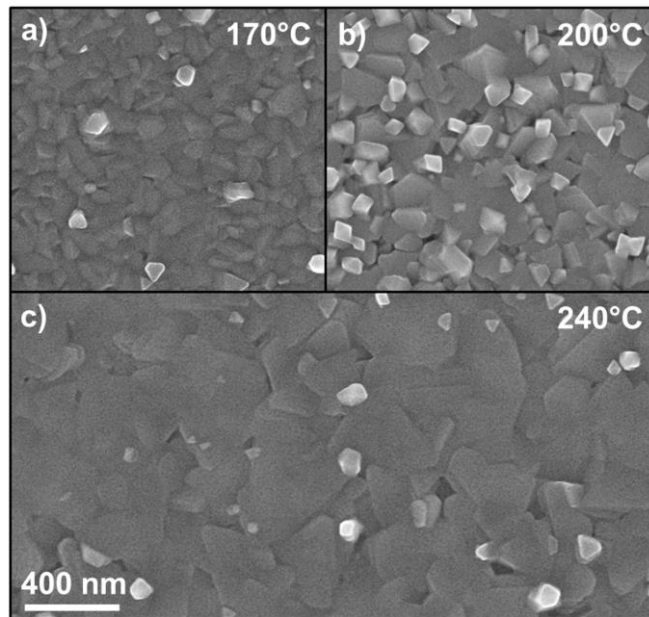


Figure 4-57. SEM images of GST films deposited on thermally pre-heated Si(111) at different temperatures.

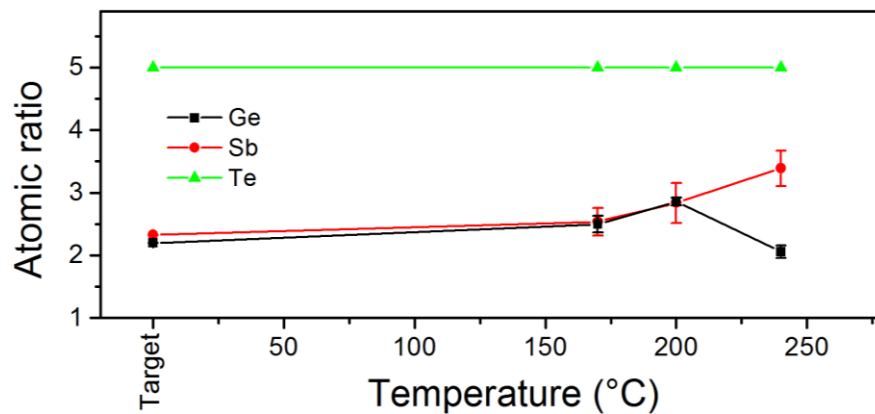


Figure 4-58. Composition of GST films on thermally pre-heated Si(111) deposited at different substrate temperatures as measured by EDX.

In Figure 4-59, three 2θ - ω scans are presented for thermally pre-treated films deposited at 170, 200 and 240°C. A first feature to note is that the diffracted intensities from the GST peaks are much lower than those from the films deposited at similar temperatures without thermal heat-treatment. In fact, in order to resolve any diffracted intensity from the film deposited at 170°C, an intentional misalignment of the Si substrate was needed in order to suppress the substrate intensity. All films were measured without a Ni-filter in order to gain intensity. Hence, the corresponding Cu $K\beta$ contribution is situated on the left flank of the GST(0005) reflection. The film deposited at 170°C (black curve) is hexagonal, as evidenced from the peak in the near of the (0004) reflection marker. Still, there is no possibility to determine if it is the GST225 or GST124 phase, due to the lack of diffraction peaks at low angular positions. The most probably phase, however, is the GST225 phase since no preferential loss of Ge has taken place as measured by EDX. The next film in the series (red curve) can really be identified as GST225 phase, although the (0001), (0002) and (0003) peaks are very weak. The last film, deposited at 240°C seems to have

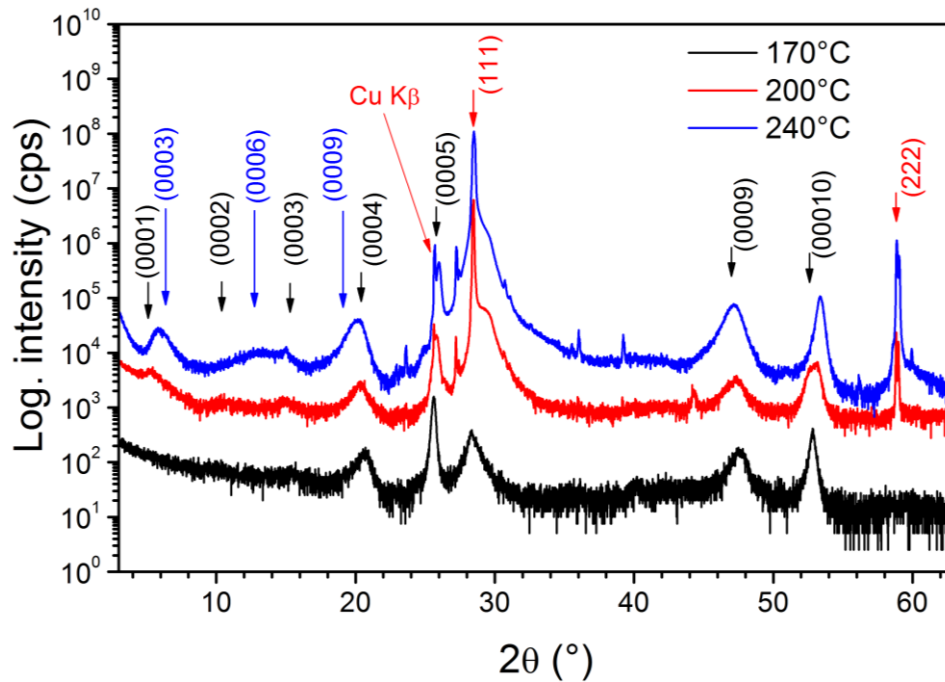


Figure 4-59. 2θ - ω scans for films deposited at different substrate temperatures on thermally pre-treated Si(111). Hexagonal phase reflection positions of the GST225 and GST124 are marked with black and blue, respectively. Substrate contributions are annotated in red. The red and blue curves have been multiplied with 10 and 100, respectively.

transitioned to the GST124 phase by judging from the match with the blue arrows in the image. This is not surprising, since the EDX measurements showed a loss of Ge and Te for this film. The overall impression is that the crystalline quality is inferior compared to the GST films on Si(111) without an extra thermal pre-treatment.

This impression is further supported by a φ -scan of the GST{10-13} planes in the film deposited at 240°C. The result can be viewed in Figure 4-60. As a comparison, the scans of two films without any extra thermal pre-treatment are presented alongside. The scans are presented without intensity offset so that the comparison gets easier. The film on the substrate exposed to a thermal pre-treatment (blue curve) shows a six-fold symmetry, i.e. two times three contributions from epitaxial rotational twin domains. However, the intensity is weak and significant elevated background intensity is present, which is an indication of an additional polycrystalline part in the film. This is to be compared with the black curve which represents the films which was deposited at a lower temperature (170°C) but without an extra thermal pre-treatment of the substrate. Recalling the previous deposition series (section 4.3.1), this was one of the films with the lowest crystalline quality. Now, compared with the film deposited on a thermally pre-treated substrate, it stands out as a film with high quality crystalline content. This is already enough evidence to state that the thermal heat-treatment, applied in the way presented in this thesis, is detrimental for the films. However, a comparison with the film deposited at 280°C without thermal pre-treatment of the substrate is also given. The diffracted intensity for this film was reduced by a factor 5 in order to be displayed on the same axis. This clearly demonstrates the large difference in crystal quality between the two films. This is further substantiated when comparing the thickness of the films being 19 nm for the film deposited on a non-

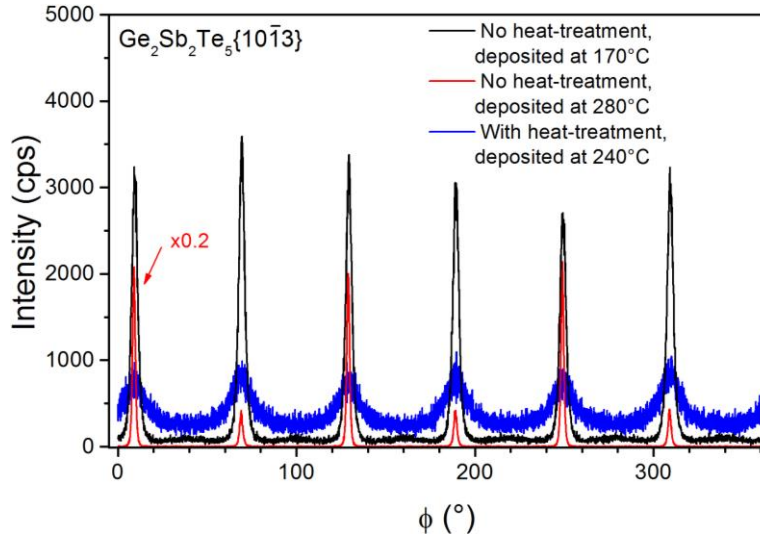


Figure 4-60. GST{10-13} φ -scans for films deposited at different substrate temperatures on Si(111). The blue curve represents a GST film deposited at a thermally pre-treated substrate whereas black and red curves were deposited at non-thermally pre-treated substrates. The intensity of the red curve has been divided by 5.

thermally pre-treated substrate compared to roughly 100 nm for the film deposited on the thermally pre-treated substrate. With the results of these experiments in mind, it is safe to say that the thermal pre-treatment of the Si substrates is not beneficial for the growth of GST on Si(111).

The exact underlying mechanism, though, is still unclear. However, the most probable cause is a degradation of the Si substrate surface due to a reduction of the vacuum quality. In fact, during the heating ramp, the background pressure increased up to $1 \cdot 10^{-5}$ mbar, i.e. three orders of magnitude higher than the standard background pressure. This outgassing could contribute to a degradation of the surface, in form of an oxide layer or some other form of contamination layer. *In-situ* based methods like reflection high energy electron diffraction that monitors the initial substrate quality as well as giving insight to the subsequent growth could be a helpful tool to at least partly overcome the problems that thermal treatment causes.

4.4.3. Summary of the results on the deposition of GST films on Si(111)

In this section, the epitaxial growth of GST on Si(111) substrates was investigated. Two different types of substrate pre-treatment were used: non-thermal pre-treatment and thermal pre-treatment. For the non-thermally treated substrates high quality epitaxial films were obtained. A strong substrate temperature dependence on the crystal quality was found. At low substrate temperatures the out-of-plane rocking curves can be fitted with two peaks: one broad base peak of around $0.5\text{-}1.5^\circ$ width and a very sharp peak of around 0.05° width. At high temperatures the broad background peak vanishes and only the narrow peak remains. Simultaneously, the chemical composition also changes and a phase transition from GST225 to GST124 can be observed. The epitaxial relationship is defined by GST(0001), GST[2-1-10] || BaF₂(111), BaF₂[1-10].

For the thermally pre-treated substrates, a severe deterioration in crystal quality of the deposited films was observed. The films were characterized by large crystallites protruding from the surface, resulting in a rough topography. The films were nevertheless epitaxial with the same orientational relationships as the films on non-treated substrates, although of inferior quality.

Chapter 5

Summary and outlook

Phase change materials of Ge-Sb-Te (GST) alloys are thought to revolutionize the non-volatile memory market in the future with an optimal combination of write speed and data retention^[10]. Especially, ordered thin films of GST have been shown to possess remarkable phase change characteristics^[20]. Even more highly ordered films in form of epitaxial layers have since then been shown to undergo epitaxial re-crystallization when being switched between the amorphous and the crystalline state. The epitaxial layers have, until now, only been deposited with molecular beam epitaxy, a slow and costly deposition method.

Therefore, an attempt was made in this thesis to investigate the possibilities of using Pulsed Laser Deposition (PLD) in producing epitaxial GST films. Before this study was initiated, only scarce reports of PLD in combination with GST films had been published^[26-29] and never in the form of epitaxial layers. Furthermore, no systematic investigations had been presented and a complete picture was missing. Hence, a more systematic study of common, yet important, deposition parameters was undertaken in this work. The main experimental parameters investigated were substrate temperature, laser pulse frequency which controls the deposition rate and Ar background pressure. The investigations were conducted on Si(100) with the native oxide still present for amorphous and polycrystalline films, whereas for epitaxial films crystalline substrate surfaces were used, i.e. KCl(100), BaF₂(111) and Si(111). The gained results and insights are summarized as follows:

Polycrystalline growth

In section 4.1, initial investigations on the polycrystalline growth of GST on Si(100) substrates with PLD were presented. The GST films were confirmed to be amorphous in the as-deposited state and showed the expected crystallization temperatures for the two crystalline phases ($\sim 150^\circ\text{C}$ and $\sim 250^\circ\text{C}$). The target stoichiometry is transferred well to the films with an almost ideal GST225 composition. Atomic resolution HAADF-STEM images made possible the direct observation of the cubic and hexagonal phases in an unprecedented way^[93]. Depositing the films at elevated substrate temperatures ($> 130^\circ\text{C}$) resulted in crystalline films with a clear fiber texture. The crystalline phase is either cubic or hexagonal at temperatures below 150°C , whereas the hexagonal phase forms at temperatures above 150°C . The preferred growth orientation is such that the hexagonal close-packed planes are parallel with the substrate surface, i.e. GST(111) or GST(0001) oriented for cubic or hexagonal, respectively.

Epitaxial growth of GST on KCl(100)

In section 4.2, the growth of GST on KCl(100) substrates was investigated^[112]. Three deposition parameters were investigated: substrate temperature, deposition rate and film thickness. It was found that the temperature has a very strong influence on the crystal growth in the films. At low temperatures (<140°C) amorphous films grow which transform into polycrystalline fiber textured hexagonal GST(0001) films in the substrate temperature range of 140-200°C. Between 200-270°C only hexagonal (0001) textured/epitaxial films are obtained. Above this temperature the cubic (100) orientation dominates the growth and the films are epitaxial. This indicates that PLD-deposited GST films can only be forced to grow in the cubic (100) orientation at high temperatures. The out-of-plane rocking curves are typically a few tenths of degrees wide for (0001) dominated films and 1.5-2° for (100) dominated films. This shows that the GST[0001] direction is the preferred growth orientation. Furthermore, a previously unknown crystal orientation was found in the GST(100) dominated temperature regime, namely the GST(221) orientation.

An increase of deposition rate weakly deteriorates the crystalline quality in the investigated range between 2.5- 250 nm/min for samples deposited in the GST(100) orientation dominated regime. Nevertheless, the films grow epitaxial at all deposition rates.

Variation of the film thickness from 8.5 nm up to 170 nm in the GST(100) orientation dominated temperature regime revealed that the GST(221) orientation is not present at thicknesses below 68 nm. Above that thickness the GST(221) orientation emerges and at 170 nm the GST(221) orientation is fully evolved.

Epitaxial growth of GST on BaF₂(111)

In section 4.3 the growth of GST films on (111) oriented BaF₂ substrates was examined^[124]. Mainly, the effect of substrate temperature was studied. The growth is characterized by one hexagonal out-of-plane GST(0001) orientation. This is different to the case of KCl(100) substrates where three out-of-plane orientations were present in the films. The films grow epitaxially already at a substrate temperature as low as 85°C with no observable polycrystalline growth. The in-plane orientation is characterized by two rotational twin domains at substrate temperatures below 210°C. The high symmetry directions in the GST film and the substrate are aligned, i.e. GST[-12-10] || BaF₂[1-10] and GST[1-210] || BaF₂[1-10]. Above 210°C the latter orientation dominates the growth.

Using a higher deposition rate deteriorates the crystal quality weakly, whereas a low deposition rate combined with a high substrate temperature promotes Ge and Te desorption and a transition to the GST124 phase. A high Ar background pressure ($4 \cdot 10^{-3}$ mbar) during deposition does not prevent this desorption from taking place.

Amorphous films deposited at room temperature on BaF₂(111) which were subsequently annealed *ex situ* possess a cubic crystal structure without no traces of the hexagonal phase. The annealed films crystallize in an epitaxial manner. An annealing temperature of 200°C resulted in the highest crystalline quality.

Epitaxial growth of GST on Si(111)

In section 4.4, the epitaxial growth of GST on Si(111) substrates was investigated. Two different types of substrate pre-treatment were used: non-thermal pre-treatment and thermal pre-treatment. For the non-thermally treated substrates high quality epitaxial films were obtained. A strong substrate temperature dependence on the crystal quality was found. At low substrate temperatures the out-of-plane rocking curves can be fitted with two peaks: one broad base peak of around $0.5\text{-}1.5^\circ$ width and a very sharp peak of around 0.05° width. At high temperatures the broad background peak vanishes and only the narrow peak remains. Simultaneously, the chemical composition also changes and a phase transition from GST225 to GST124 can be observed, i.e. loss of Ge and Te. The epitaxial relationship is defined by GST(0001), GST[2-1-10] || BaF₂(111), BaF₂[1-10].

For the thermally pre-treated substrates, a notable deterioration in crystal quality of the deposited films was seen. The films were characterized by large crystallites protruding from the surface, resulting in a rough topography. The films were nevertheless epitaxial with the same orientational relationships as the films on non-treated substrates, although of inferior quality.

Outlook

The results demonstrate that the epitaxial growth of GST films using PLD is possible with relative small effort and ease. There still exist some unanswered questions, however, that could be addressed in the future:

- To improve the substrate conditioning and subsequent growth and to gain deeper insights about the exact growth mechanism, future experiments should be accompanied by *in situ* diagnostic methods like reflection high energy electron diffraction.
- The epitaxial GST films presented in this thesis have not been subjected to neither optical nor electrical switching tests. For any possible phase change application, the switching characteristics are important to understand. An optical static test unit is currently under development.
- The findings of an epitaxial cubic phase upon subsequent annealing of as-deposited amorphous GST films on BaF₂(111) is highly interesting. Here, more thorough investigations are needed to clarify, why it is possible to obtain cubic GST by annealing, but not during *in situ* heating of the films during deposition.
- Although many parameters were systematically investigated in this thesis, a unique parameter for PLD was left constant: the laser fluence. A variation of laser fluence and hence the kinetic energy of the species in the laser plume could drastically change the growth. Further investigations in this area should be coupled with a plasma probe to better understand the effect of the kinetic energy of the plasma species on the film growth.

Bibliography

- ¹ R. A. Hein, J. W. Gibson, R. Mazelsky, R. C. Miller, and J. K. Hulm, *Superconductivity in Germanium Telluride*, Phys. Rev. Lett. **12**, 320 (1964).
- ² J. K. Hulm, C. K. Jones, D. W. Deis, H. A. Fairbank, and P. A. Lawless, *Superconducting Interactions in Tin Telluride*, Phys. Rev **169**, 388 (1968).
- ³ J. S. Lee, A. Richardella, D. W. Rench, R. D. Fraleigh, T. C. Flanagan, J. A. Borchers, J. Tao, and N. Samarth, *Ferromagnetism and spin-dependent transport in n-type Mn-doped bismuth telluride thin films*, Phys. Rev. B **89**, 174425 (2014).
- ⁴ F. Kadlec, C. Kadlec, P. Kužel, and J. Petzelt, *Study of the ferroelectric phase transition in germanium telluride using time-domain terahertz spectroscopy*, Phys. Rev. B **84**, 205209 (2011).
- ⁵ T. Schröder, M. N. Schneider, T. Rosenthal, P. Urban, F. Fahrnbauer, C. Stiewe, C. Gold, E.-W. Scheidt, W. Scherer, and O. Oeckler, *Thermoelectric properties of metastable Ge/Sb/Te and Ge/Bi/Te compounds*, AIP Conf. Proc. **1449**, 159 (2012).
- ⁶ E.-R. Sittner, K. S. Siegert, P. Jost, C. Schlockermann, F. R. L. Lange, and M. Wuttig, *(GeTe)_x-(Sb₂Te₃)_{1-x} phase-change thin films as potential thermoelectric materials*, Phys. Status Solidi A **210**, 147 (2013).
- ⁷ H. Zhang, C.-X. Liu, X.-L. Qi, X. Dai, Z. Fang, and S.-C. Zhang, *Topological insulators in Bi₂Se₃, Bi₂Te₃, and Sb₂Te₃ with a single Dirac cone on the surface*, Nat. Phys. **5**, 438 (2009).
- ⁸ M. Wuttig, *Phase change materials: Chalcogenides with remarkable properties due to an unconventional bonding mechanism*, Phys. Status Solidi B **249**, 1843 (2012).
- ⁹ D. Lencer, M. Salinga, B. Grabowski, T. Hickel, J. Neugebauer, and M. Wuttig, *A map for phase-change materials*, Nat. Mater. **7**, 972 (2008).
- ¹⁰ S. Raoux, F. Xiong, M. Wuttig, and E. Pop, *Phase change materials and phase change memory*, MRS Bull. **39**, 703 (2014).
- ¹¹ P. Hosseini, C. D. Wright, and H. Bhaskaran, *An optoelectronic framework enabled by low-dimensional phase-change films*, Nature **511**, 206 (2014).
- ¹² S. R. Ovshinsky, *Reversible Electrical Switching Phenomena in Disordered Structures*, Phys. Rev. Lett. **21**, 1450 (1968).
- ¹³ N. Yamada, *Origin, secret, and application of the ideal phase-change material GeSbTe*, Phys. Status Solidi B **249**, 1837 (2012).
- ¹⁴ S. Raoux, G. W. Burr, M. J. Breitwisch, C. T. Rettner, Y. C. Chen, R. M. Shelby, M. Salinga, D. Krebs, S. H. Chen, H. L. Lung, and C. H. Lam, *Phase-change random access memory: A scalable technology*, IBM J. Res. Dev. **52**, 465 (2008).
- ¹⁵ R. E. Simpson, M. Krbal, P. Fons, A. V. Kolobov, J. Tominaga, T. Uruga, and H. Tanida, *Toward the Ultimate Limit of Phase Change in Ge₂Sb₂Te₅*, Nano Lett. **10**, 414 (2010).
- ¹⁶ T. Siegrist, P. Merkelbach, and M. Wuttig, *Phase Change Materials: Challenges on the Path to a Universal Storage Device*, Annu. Rev. Condens. Matter Phys. **3**, 215 (2012).
- ¹⁷ M. Wuttig and S. Raoux, *The Science and Technology of Phase Change Materials*, Z. Anorg. Allg. Chem. **638**, 2455 (2012).

- 18 F. Xiong, A. D. Liao, D. Estrada, and E. Pop, *Low-Power Switching of Phase-*
19 *Change Materials with Carbon Nanotube Electrodes*, *Science* **332**, 568 (2011).
- 20 Timeline of phase change memories on Wikipedia
21 http://en.wikipedia.org/wiki/Phase-change_memory, accessed at: 29.10.2014
- 22 R. E. Simpson, P. Fons, A. V. Kolobov, T. Fukaya, M. Krbal, T. Yagi, and J.
23 Tominaga, *Interfacial phase-change memory*, *Nat. Nano* **6**, 501 (2011).
- 24 R. Shayduk and W. Braun, *Epitaxial films for Ge-Sb-Te phase change memory*, *J.*
25 *Cryst. Growth* **311**, 2215 (2009).
- 26 R. Shayduk, F. Katmis, W. Braun, and H. Riechert, *Epitaxial growth and structure*
27 *of Ge-Sb-Te phase change materials on GaSb*, *J. Vac. Sci. Tech. B* **28**, C3E1 (2010).
- 28 F. Katmis, R. Calarco, K. Perumal, P. Rodenbach, A. Giussani, M. Hanke, A.
29 Proessdorf, A. Trampert, F. Grosse, R. Shayduk, R. Champion, W. Braun, and
30 H. Riechert, *Insight into the Growth and Control of Single-Crystal Layers of Ge-Sb-Te*
31 *Phase-Change Material*, *Cryst. Growth Des.* **11**, 4606 (2011).
- 32 P. Rodenbach, R. Calarco, K. Perumal, F. Katmis, M. Hanke, A. Proessdorf,
33 W. Braun, A. Giussani, A. Trampert, H. Riechert, P. Fons, and A. V. Kolobov,
34 *Epitaxial phase-change materials*, *Phys. Status Solidi (RRL)* **6**, 415 (2012).
- 35 P. Rodenbach, A. Giussani, K. Perumal, M. Hanke, M. Dubslaff, H. Riechert,
36 R. Calarco, M. Burghammer, A. V. Kolobov, and P. Fons, *Recrystallization of an*
37 *amorphized epitaxial phase-change alloy: A phoenix arising from the ashes*, *Appl. Phys.*
38 *Lett.* **101**, 3 (2012).
- 39 P. Němec, A. Moreac, V. Nazabal, M. Pavlišta, J. Prikryl, and M. Frumar, *Ge-*
40 *Sb-Te thin films deposited by pulsed laser: An ellipsometry and Raman scattering*
41 *spectroscopy study*, *J. Appl. Phys.* **106**, 103509 (2009).
- 42 P. Němec, J. Prikryl, V. Nazabal, and M. Frumar, *Optical characteristics of pulsed*
43 *laser deposited Ge-Sb-Te thin films studied by spectroscopic ellipsometry*, *J. Appl. Phys*
44 **109**, 073520 (2011).
- 45 D. Z. Hu, F. M. Pan, X. M. Lu, and J. S. Zhu, *Influence of laser energy on the*
46 *crystallization of Ge₂Sb₂Te₅ thin film prepared by pulsed laser deposition*, *Phys. Status*
47 *Solidi A* **208**, 2749 (2011).
- 48 M. Popescu, A. Velea, F. Sava, A. Lőrinczi, A. Tomescu, C. Simion, E. Matei,
49 G. Socol, I. N. Mihailescu, A. Andonie, and I. Stamatina, *Structure and properties of*
50 *silver doped SnSe₂ and Ge₂Sb₂Te₅ thin films prepared by pulsed laser deposition*, *Phys.*
51 *Status Solidi A* **207**, 516 (2010).
- 52 S. R. Ovshinsky, US Patent No.: 3336486 A, 1967
- 53 N. Yamada, E. Ohno, N. Akahira, K. Nishiuchi, K. Nagata, and M. Takao,
54 *High Speed Overwritable Phase Change Optical Disk Material*, *Jpn. J. Appl. Phys.* **26**,
55 61 (1987).
- 56 C. Kittel, *Introduction to Solid State Physics*, (John Wiley & Sons, Inc, New York,
57 2005).
- 58 J. Y. Raty, V. Godlevsky, P. Ghosez, C. Bichara, J. P. Gaspard, and J. R.
59 Chelikowsky, *Evidence of a Reentrant Peierls Distortion in Liquid GeTe*, *Phys. Rev.*
60 *Lett.* **85**, 1950 (2000).
- 61 A. V. Kolobov, P. Fons, A. I. Frenkel, A. L. Ankudinov, J. Tominaga, and T.
62 Uruga, *Understanding the phase-change mechanism of rewritable optical media*, *Nat.*
63 *Mater.* **3**, 703 (2004).
- 64 B. Huang and J. Robertson, *Bonding origin of optical contrast in phase-change memory*
65 *materials*, *Phys. Rev. B* **81**, 081204 (2010).

- 36 D. Lencer, M. Salinga, and M. Wuttig, *Design Rules for Phase-Change Materials in*
37 *Data Storage Applications*, Adv. Mater. **23**, 2030 (2011).
- 38 M. Wuttig and N. Yamada, *Phase-change materials for rewriteable data storage*, Nat.
39 Mater. **6**, 824 (2007).
- 40 K. Shportko, S. Kremers, M. Woda, D. Lencer, J. Robertson, and M. Wuttig,
41 *Resonant bonding in crystalline phase-change materials*, Nat. Mater. **7**, 653 (2008).
- 42 M. Wuttig, *Phase change materials: The importance of resonance bonding*, Phys. Status
43 Solidi B **246**, 1820 (2009).
- 44 D. Adler, H. K. Henisch, and S. N. Mott, *The mechanism of threshold switching in*
45 *amorphous alloys*, Rev. Mod. Phys. **50**, 209 (1978).
- 46 P. Zalden, C. Bichara, J. van Eijk, C. Braun, W. Bensch, and M. Wuttig, *Atomic*
47 *structure of amorphous and crystallized $Ge_{15}Sb_{85}$* , J. Appl. Phys. **107** (2010).
- 48 S. Raoux, A. K. König, H.-Y. Cheng, D. Garbin, R. W. Cheek, J. L. Jordan-
49 Sweet, and M. Wuttig, *Phase transitions in Ga-Sb phase change alloys*, Phys. Status
50 Solid. B **249**, 1999 (2012).
- 51 N. K. Abrikosov and G. Danilova-Dobryakova, *An investigation of the structural*
52 *diagram of Sb_2Te_3 - $GeTe$* , Izv. Akad. Nauk. SSSR Neorg. Mater. **1**, 204 (1965).
- 53 I. Petrov, R. Imamov, and Z. Pinsker, *Electronographic determination of the structures*
54 *of $Ge_2Sb_2Te_3$ and $GeSb_4Te_7$* , Sov. Phys. Cryst. **13**, 339-344 (1968), Sov. Phys. Cryst.
55 **13**, 339 (1968).
- 56 N. Yamada, E. Ohno, K. Nishiuchi, N. Akahira, and M. Takao, *Rapid-phase*
transitions of $GeTe$ - Sb_2Te_3 pseudobinary amorphous thin films for an optical disk memory,
J. Appl. Phys. **69**, 2849 (1991).
- V. I. Kosyakov, V. A. Shestakov, L. E. Shelimova, F. A. Kuznetsov, and V. S.
Zemskov, *Topological characterization of the Ge-Sb-Te phase diagram*, Inorg. Mater.
36, 1004 (2000).
- T. Nonaka, G. Ohbayashi, Y. Toriumi, Y. Mori, and H. Hashimoto, *Crystal*
structure of $GeTe$ and $Ge_2Sb_2Te_5$ meta-stable phase, Thin Solid Films **370**, 258 (2000).
- J. Goldak, C. S. Barrett, D. Innes, and W. Youdelis, *Structure of Alpha $GeTe$* , J.
Chem. Phys. **44**, 3323 (1966).
- L. Baldé, B. Legendre, and A. Balkhi, *Etude du diagramme d'équilibre entre phases du*
système ternaire germanium-étain-tellure, J. Alloy. Compd. **216**, 285 (1995).
- J. P. Gaspard, A. Pellegatti, F. Marinelli, and C. Bichara, *Peierls instabilities in*
covalent structures I. Electronic structure, cohesion and the $Z = 8 - N$ rule, Philos. Mag.
B **77**, 727 (1998).
- D. Lencer, Ph.D. Thesis, RWTH Aachen University, 2010.
- T. L. Anderson and H. B. Krause, *Refinement of the Sb_2Te_3 and Sb_2Te_2Se structures*
and their relationship to nonstoichiometric $Sb_2Te_{3-y}Se_y$ compounds, Acta. Crystallogr. B
30, 1307 (1974).
- Y. Ma, G. Liu, P. Zhu, H. Wang, X. Wang, Q. Cui, J. Liu, and Y. Ma,
Determinations of the high-pressure crystal structures of Sb_2Te_3 , J. Phys.: Condens.
Matter **24**, 475403 (2012).
- A. V. Kolobov and J. Tominaga, *Chalcogenides: Metastability and Phase Change*
Phenomena, (Springer Verlag, Berlin, Heidelberg, 2012).
- S. Raoux and M. Wuttig, *Phase Change Materials: Science and Applications*,
(Springer, New York, 2010).
- A. Abrutis, V. Plausinaitiene, M. Skapas, C. Wiemer, O. Salicio, M. Longo, A.
Pirovano, J. Siegel, W. Gawelda, S. Rushworth, and C. Giesen, *Chemical vapor*

- deposition of chalcogenide materials for phase-change memories, *Microelectron. Eng.* **85**, 2338 (2008).
- 57 I. Friedrich, V. Weidenhof, W. Njoroge, P. Franz, and M. Wuttig, *Structural transformations of $Ge_2Sb_2Te_5$ films studied by electrical resistance measurements*, *J. Appl. Phys.* **87**, 4130 (2000).
- 58 B. J. Kooi, W. M. G. Groot, and J. T. M. De Hosson, *In situ transmission electron microscopy study of the crystallization of $Ge_2Sb_2Te_5$* , *J. Appl. Phys.* **95**, 924 (2004).
- 59 H. Lu, E. Thelander, J. W. Gerlach, D. Hirsch, U. Decker, and B. Rauschenbach, *$Ge_2Sb_2Te_5$ phase-change films on polyimide substrates by pulsed laser deposition*, *Appl. Phys. Lett* **101** (2012).
- 60 H. Lu, E. Thelander, J. W. Gerlach, U. Decker, B. Zhu, and B. Rauschenbach, *Single Pulse Laser-Induced Phase Transitions of PLD-Deposited $Ge_2Sb_2Te_5$ Films*, **23**, 3621 (2013).
- 61 E. Morales-Sánchez, E. Prokhorov, J. González-Hernández, and A. Mendoza-Galván, *Structural, electric and kinetic parameters of ternary alloys of $GeSbTe$* , *Thin Solid Films* **471**, 243 (2005).
- 62 T. Matsunaga, N. Yamada, and Y. Kubota, *Structures of stable and metastable $Ge_2Sb_2Te_5$, an intermetallic compound in $GeTe-Sb_2Te_3$ pseudobinary systems*, *Acta Crystallogr. B* **60**, 685 (2004).
- 63 C. Donyau, J. Tzuan-Reng, H. Der-Ray, C. Yung-Yuan, and L. Chung-Ping, *Kinetic Crystallization Behavior of Phase-Change Medium*, *Jpn. J. Appl. Phys.* **38**, 1649 (1999).
- 64 B. J. Kooi and J. T. M. De Hosson, *Electron diffraction and high-resolution transmission electron microscopy of the high temperature crystal structures of $Ge_xSb_2Te_{3+x}$ ($x=1,2,3$) phase change material*, *J. Appl. Phys.* **92**, 3584 (2002).
- 65 P. Urban, M. N. Schneider, L. Erra, S. Welzmler, F. Fahrnbauer, and O. Oeckler, *Temperature dependent resonant X-ray diffraction of single-crystalline $Ge_2Sb_2Te_5$* , **15**, 4823 (2013).
- 66 J. L. F. Da Silva, A. Walsh, and H. Lee, *Insights into the structure of the stable and metastable $(GeTe)_m(Sb_2Te_3)_n$ compounds*, *Phys. Rev. B* **78**, 224111 (2008).
- 67 Z. Sun, J. Zhou, and R. Ahuja, *Structure of Phase Change Materials for Data Storage*, *Phys. Rev. Lett.* **96**, 055507 (2006).
- 68 Z. Sun, S. Kyrsta, D. Music, R. Ahuja, and J. M. Schneider, *Structure of the $Ge-Sb-Te$ phase-change materials studied by theory and experiment*, *Solid State Commun.* **143**, 240 (2007).
- 69 K. Perumal, Ph.D. Thesis, Humboldt-Universität zu Berlin, 2013.
- 70 P. Zalden, Ph.D Thesis, RWTH Aachen University, 2012.
- 71 T. Matsunaga, H. Morita, R. Kojima, N. Yamada, K. Kifune, Y. Kubota, Y. Tabata, J.-J. Kim, M. Kobata, E. Ikenaga, and K. Kobayashi, *Structural characteristics of $GeTe$ -rich $GeTe-Sb_2Te_3$ pseudobinary metastable crystals*, *J. Appl. Phys.* **103**, 093511 (2008).
- 72 O. G. Karpinsky, L. E. Shelimova, M. A. Kretova, and J. P. Fleurial, *An X-ray study of the mixed-layered compounds of $(GeTe)_n(Sb_2Te_3)_m$ homologous series*, *J. Alloys Compd.* **268**, 112 (1998).
- 73 T. Matsunaga and N. Yamada, *Structural investigation of $GeSb_2Te_4$: A high-speed phase-change material*, *Phys. Rev. B* **69**, 104111 (2004).
- 74 K. Kifune, Y. Kubota, T. Matsunaga, and N. Yamada, *Extremely long period-stacking structure in the $Sb-Te$ binary system*, *Acta Crystallogr. B* **61**, 492 (2005).

- 75 CaRIne Crystallography Divergent S.A.,
76 <http://carine.crystallography.pagespro-orange.fr>
- 77 T. H. Maiman, *Stimulated Optical Radiation in Ruby*, Nature **187**, 493 (1960).
78 H. M. Smith and A. F. Turner, *Vacuum Deposited Thin Films Using a Ruby Laser*,
79 Appl. Opt. **4**, 147 (1965).
- 80 D. Dijkkamp, T. Venkatesan, X. D. Wu, S. A. Shaheen, N. Jisrawi, Y. H. Min-
81 Lee, W. L. McLean, and M. Croft, *Preparation of Y-Ba-Cu oxide superconductor thin
82 films using pulsed laser evaporation from high T_c bulk material*, Appl. Phys. Lett. **51**,
83 619 (1987).
- 84 D. B. Chrisey and G. K. Hubler, *Pulsed Laser Deposition of Thin Films*, (Wiley,
85 New York, 1994).
- 86 T. Tsafack, E. Piccinini, B.-S. Lee, E. Pop, and M. Rudan, *Electronic, optical and
87 thermal properties of the hexagonal and rocksalt-like $Ge_2Sb_2Te_5$ chalcogenide from first-
88 principle calculations*, J. Appl. Phys. **110**, 063716 (2011).
- 89 R. Eason, *Pulsed Laser Deposition of Thin Films: Applications-Led Growth of
90 Functional Materials*, (Wiley, New Jersey, 2007).
- 91 Kern. W and P. D, *Cleaning Solutions Based on Hydrogen Peroxide for Use in Silicon
92 Semiconductor Technology*, RCA Rev. **31** (1970).
- 93 G. Binnig, H. Rohrer, C. Gerber, and E. Weibel, *7×7 Reconstruction on Si(111)
94 Resolved in Real Space*, Phys. Rev. Lett. **50**, 120 (1983).
- 95 L. Spiess, G. Teichert, R. Schwarzer, H. Behnken, and C. Genzel, *Moderne
Röntgenbeugung: Röntgendiffraktometrie für Materialwissenschaftler, Physiker und
Chemiker*, (Vieweg + Teubner, Wiesbaden, 2009).
- W. C. Marra, P. Eisenberger, and A. Y. Cho, *X-ray total-external-reflection–Bragg
diffraction: A structural study of the GaAs–Al interface*, J. Appl. Phys. **50**, 6927
(1979).
- G. H. Vineyard, *Grazing-incidence diffraction and the distorted-wave approximation for
the study of surfaces*, Phys. Rev. B **26**, 4146 (1982).
- S. Kobayashi, *X-ray thin-film techniques IV. In-plane XRD measurements*, The
Rigaku Journal **26**, 3 (2010).
- RayfleX, Rich. Seifert & Co, now General Electrics Measurement and Control,
[http://www.ge-mcs.com/de/radiography-x-ray/analytical-x-ray-xrd/1050-
siweb-pl425.html](http://www.ge-mcs.com/de/radiography-x-ray/analytical-x-ray-xrd/1050-siweb-pl425.html)
- J. O'Connor, B. A. Sexton, and R. S. C. Smart, *Surface Analysis Methods in
Materials Science*, (Springer-Verlag Berlin, Heidelberg, 1992).
- H. Rose, *Outline of a spherically corrected semi-aplanatic medium-voltage transmission
electron microscope*, Optik **85**, 19 (1990).
- M. Haider, H. Rose, S. Uhlemann, E. Schwan, B. Kabius, and K. Urban, *A
spherical-aberration-corrected 200 keV transmission electron microscope*, Ultramicroscopy
75, 53 (1998).
- D. B. Williams and C. B. Carter, *Transmission Electron Microscopy: A Textbook for
Materials Science*, (Springer, New York, 2009).
- U. Ross, A. Lotnyk, E. Thelander, and B. Rauschenbach, *Direct imaging of crystal
structure and defects in metastable $Ge_2Sb_2Te_5$ by quantitative aberration-corrected scanning
transmission electron microscopy*, Appl. Phys. Lett **104**, 121904 (2014).
- M. Naito, M. Ishimaru, Y. Hirotsu, and M. Takashima, *Local structure analysis of
Ge-Sb-Te phase change materials using high-resolution electron microscopy and nanobeam
diffraction*, J. Appl. Phys. **95**, 8130 (2004).
- 95 Quantax ESPRIT, Bruker Nano GmbH, <http://www.bruker.com>

- 96 P. Eaton and P. West, in *Atomic Force Microscopy* on p. 116. (Oxford University Press, New York, 2010).
- 97 J. Houška, E. M. Peña-Méndez, J. Kolář, J. Přikryl, M. Pavlišta, M. Frumar, T. Wágner, and J. Havel, *Laser desorption time-of-flight mass spectrometry of atomic switch memory $Ge_2Sb_2Te_5$ bulk materials and its thin films*, Rapid Commun. Mass Spectrom. **28**, 699 (2014).
- 98 P. Němec, V. Nazabal, A. Moreac, J. Gutwirth, L. Beneš, and M. Frumar, *Amorphous and crystallized Ge–Sb–Te thin films deposited by pulsed laser: Local structure using Raman scattering spectroscopy*, Mater. Chem. Phys. **136**, 935 (2012).
- 99 V. Weidenhof, I. Friedrich, S. Ziegler, and M. Wuttig, *Atomic force microscopy study of laser induced phase transitions in $Ge_2Sb_2Te_5$* , J. Appl. Phys. **86**, 5879 (1999).
- 100 W. K. Njoroge, H.-W. Wöltgens, and M. Wuttig, *Density changes upon crystallization of $Ge_2Sb_{2.04}Te_{4.74}$ films*, J. Vac. Sci. Technol. A **20**, 230 (2002).
- 101 H. Xi, Q. Liu, Y. Tian, Y. Wang, S. Guo, and M. Chu, *$Ge_2Sb_{1.5}Bi_{0.5}Te_5$ thin film as inorganic photoresist*, Opt. Mater. Express **2**, 461 (2012).
- 102 C. Deng, Y. Geng, and Y. Wu, *Selective wet etching of $Ge_2Sb_2Te_5$ phase-change thin films in thermal lithography with tetramethylammonium*, Appl. Phys. A **104**, 1091 (2011).
- 103 V. Bragaglia, B. Jenichen, A. Giussani, K. Perumal, H. Riechert, and R. Calarco, *Structural change upon annealing of amorphous GeSbTe grown on Si(111)*, J. Appl. Phys. **116**, 054913 (2014).
- 104 A. V. Kolobov, M. Krbal, P. Fons, J. Tominaga, and T. Uruga, *Distortion-triggered loss of long-range order in solids with bonding energy hierarchy*, Nat. Chem. **3**, 311 (2011).
- 105 M. Winkler, X. Liu, J. D. König, L. Kirste, H. Böttner, W. Bensch, and L. Kienle, *Sputtered p-Type Sb_2Te_3 / $(Bi,Sb)_2Te_3$ Soft Superlattices Created by Nanoalloying*, J. Electron. Mater. **41**, 1322 (2012).
- 106 Z. Aabdin, N. Peranio, M. Winkler, D. Bessas, J. König, R. P. Hermann, H. Böttner, and O. Eibl, *Sb_2Te_3 and Bi_2Te_3 Thin Films Grown by Room-Temperature MBE*, J. Electron. Mater. **41**, 1493 (2012).
- 107 J. Stoemenos and R. Vincent, *Twining faults in epitaxial films of germanium telluride and $GeTe-SnTe$ alloys*, Phys. Status Solidi A **11**, 545 (1972).
- 108 A. Giussani, K. Perumal, M. Hanke, P. Rodenbach, H. Riechert, and R. Calarco, *On the epitaxy of germanium telluride thin films on silicon substrates*, Phys. Status Solidi B **249**, 1939 (2012).
- 109 K. Perumal, W. Braun, H. Riechert, and R. Calarco, *Growth control of epitaxial $GeTe-Sb_2Te_3$ films using a line-of-sight quadrupole mass spectrometer*, J. Cryst. Growth **396**, 50 (2014).
- 110 W. Braun, R. Shayduk, T. Flissikowski, M. Ramsteiner, H. T. Grahn, H. Riechert, P. Fons, and A. Kolobov, *Epitaxy of Ge-Sb-Te phase-change memory alloys*, Appl. Phys. Lett. **94**, 3 (2009).
- 111 R. Shayduk, Ph.D. Thesis, Humboldt-Universität zu Berlin, 2010.
- 112 E. Thelander, J. W. Gerlach, U. Ross, F. Frost, and B. Rauschenbach, *Epitaxial growth of Ge-Sb-Te films on KCl by high deposition rate pulsed laser deposition*, J. Appl. Phys. **115**, 213504 (2014).
- 113 M. Grundmann, *Formation of epitaxial domains: Unified theory and survey of experimental results*, Phys. Status Solidi B **248**, 805 (2011).
- 114 P. D. Pathak and N. G. Vasavada, *Thermal expansion of NaCl, KCl and CsBr by X-ray diffraction and the law of corresponding states*, Acta Crystallogr. A **26**, 655 (1970).

- 115 I.-M. Park, J.-K. Jung, S.-O. Ryu, K.-J. Choi, B.-G. Yu, Y.-B. Park, S. M. Han,
and Y.-C. Joo, *Thermomechanical properties and mechanical stresses of Ge₂Sb₂Te₅ films in
phase-change random access memory*, Thin Solid Films **517**, 848 (2008).
- 116 J. Kalb, F. Spaepen, T. P. Leervad Pedersen, and M. Wuttig, *Viscosity and elastic
constants of thin films of amorphous Te alloys used for optical data storage*, J. Appl. Phys.
94, 4908 (2003).
- 117 G. E. Ghezzi, R. Morel, A. Brenac, N. Boudet, M. Audier, F. Fillot, S.
Maitrejean, and F. Hippert, *Crystallization of Ge₂Sb₂Te₅ nanometric phase change
material clusters made by gas-phase condensation*, Appl.Phys.Lett. **101** (2012).
- 118 M.-J. Shin, D.-J. Choi, M.-J. Kang, and S.-Y. Choi, *Chemical Bonding
Characteristics of Ge₂Sb₂Te₅ for Thin Films*, J.Korean. Phys. Soc. **44**, 10 (2004).
- 119 I. Markov and S. Stoyanov, *Mechanisms of epitaxial growth*, Contemp. Phys. **28**,
267 (1987).
- 120 J. Narayan, *Recent progress in thin film epitaxy across the misfit scale* Acta Mater. **61**,
2703 (2013).
- 121 S. Raoux, W. Welnic, and D. Ielmini, *Phase Change Materials and Their Application
to Nonvolatile Memories*, Chem. Rev. **110**, 240 (2010).
- 122 U. Ross, Ph.D, *in preparation* Thesis, Universität Kiel.
- 123 H. Neumann, G. Kommichau, W. Schmitz, and B. Schumann, *Thermal
expansion of BaF₂ from 296 to 1173 K*, J. Mater. Sci. Lett. **5**, 1131 (1986).
- 124 E. Thelander, J. W. Gerlach, U. Ross, A. Lotnyk, and B. Rauschenbach, *Low
temperature epitaxy of Ge-Sb-Te films on BaF₂(111) by pulsed laser deposition*, In Press
at Appl. Phys. Lett. (2014).
- 125 D. B. Chrisey and G. K. Hubler, in *Pulsed Laser Deposition of Thin Films* on p.
346. Vol. 1, (John Wiley & Sons, Inc, New York, 1994).
- 126 Data sheet from Umicore thin film products
http://www.thinfilmproducts.umicore.com/Products/TechnicalData/show_datenblatt_gesbte.pdf, accessed at: 25.09.2014
- 127 R.-Y. Kim, H.-G. Kim, and S.-G. Yoon, *Structural properties of Ge₂Sb₂Te₅ thin films
by metal organic chemical vapor deposition for phase change memory applications*, Appl.
Phys. Lett. **89**, 102107 (2006).

Acknowledgements

The last words in this doctoral thesis should be dedicated to the people that made the work possible. It has indeed been a collaborative effort and the persons listed below are gratefully acknowledged. For those people who are not mentioned, I do apologize most sincerely. For sure it was not done on purpose.

My deep gratitude is directed towards Prof. Dr. Bernd Rauschenbach who initiated and supported this work throughout the entire course. I always felt that the door was open for discussion of both small and big matters and for that I am most grateful. Also, your positive view on my parental leave deserves a mention here.

Dr. Jürgen W. Gerlach I would like to thank sincerely. Without your willingness to help me, may it be with vacuum technology, analysis methods, discussion about results or the introduction in to the beautiful world of x-ray diffraction, this work would definitely not have looked the way it does. I also very much enjoyed all Kino-visits which amounted to a few throughout the years. Thank You!

Ulrich Ross is responsible for the beautiful TEM-images in this thesis, for which I am most grateful. For you, no TEM-lamellae can be thin enough and the time you investigated in each sample is visible in the image quality. I also value the discussion about GST-related stuff with you, which was truly beneficial in my case. Of course, also Agnes Mill and Dr. Andriy Lotnyk should be mentioned in this context since they are a crucial part of the TEM-group.

The PLD-lab group members (Isom Hilmi, Dr. Lu and Phillip Schumacher) are also acknowledged but special thanks goes out to Xinxing Sun (Sunny). Your positive attitude and big smile truly makes up for your nickname.

Many more colleagues at IOM have contributed to the work presented in this thesis. Dr. Frank Frost is greatly acknowledged for conducting AFM-measurements and Dietmar Hirsch for the tips and tricks regarding SEM/EDX. Ingrid Herold and Toni Liebeskind aided in the sample cleaning and preparation and Petra Hertel deserves thanks for helping out with substrate dicing and for providing adequate sample boxes for the massive amount of samples piling up. Christoph Grüner helped out with the annealing experiments and always made sure that I felt welcome in his lab. For that and much more I want to say thank you to all.

Also, the mechanical workshop and administration deserves to be thanked, since they really helped the work progress smoothly and the lunch round for providing a stimulating atmosphere. Mirko Naumann and Susanne Selle provided a fun and relaxed environment in and outside the office and for that I am very glad.

I am very grateful to the “BuildMoNa” graduate school for all support throughout the work and for arranging all the different scientific training possibilities. Especially Christina

Acknowledgements

Kny should be mentioned for her excellent flexible childcare which made everyday life a little bit easier to manage.

Last but not least, I would like to express my deep gratitude to my family, both old and new. To my mom, dad and sister, for always providing a firm, but stimulating and loving atmosphere. Without your guidance in my life this would thesis would probably not have taken place. The same goes for my life partner Sandra, without whom this work would have been impossible. Thank you for putting up with me during stressful moments and managing the two boys at home. This is as much your effort as mine!

Curriculum Vitae

Person

Name: M.Sc. Erik Thelander

Date of Birth: 17th of June, 1983

Place of Birth: Österhaninge, Sweden

Nationality: Swedish

Academic Education

Leibniz-Institut für Oberflächenmodifizierung e.V. and Fakultät für Physik und Geowissenschaften der Universität Leipzig 2009-Today

- Doctoral candidate and member of the graduate school “BuildMoNa”
- Title of the thesis: *Epitaxial Ge-Te-Sb Thin Films by Pulsed Laser Deposition*
- Supervisor: Prof. Dr. Dr. h.c. Bernd Rauschenbach

Uppsala University 2003-2008

- Master’s degree (M.Sc.) in chemical engineering
- Title of the thesis: *Magnetron Sputtering of New Contact Materials*
- Supervisor: Prof. Ulf Jansson

Upper Secondary School 1991-2002

- Swedish high school exam

Compulsory School 1990-1999

List of publications

The content of this thesis has been published or is in press in the following peer-reviewed journals:

1. E. Thelander, J. W. Gerlach, U. Ross, F. Frost, and B. Rauschenbach, *Epitaxial growth of Ge-Sb-Te films on KCl by high deposition rate pulsed laser deposition*, J. Appl. Phys. **115**, 213504 (2014).
2. E. Thelander, J. W. Gerlach, U. Ross, A. Lotnyk, and B. Rauschenbach, *Low temperature epitaxy of Ge-Sb-Te films on BaF₂(111) by pulsed laser deposition*, Submitted In Press at Appl. Phys. Lett. (2014).
3. U. Ross, A. Lotnyk, E. Thelander, and B. Rauschenbach, *Direct imaging of crystal structure and defects in metastable Ge₂Sb₂Te₅ by quantitative aberration-corrected scanning transmission electron microscopy*, Appl. Phys. Lett **104**, 121904 (2014).

Other publications (peer-reviewed and non-peer-reviewed):

1. X. Sun, E. Thelander, P. Lorenz, J. W. Gerlach, U. Decker, and B. Rauschenbach, *Nanosecond laser-induced phase transitions in pulsed laser deposition-deposited GeTe films*, **116**, 133501 (2014).
2. M. Ehrhardt, P. Lorenz, A. Lotnyk, H. Romanus, E. Thelander, and K. Zimmer, *Pattern transfer of sub-micrometre-scaled structures into solid copper by laser embossing*, Phys. Procedia **56**, 944 (2014).
3. U. Ross, A. Lotnyk, E. Thelander, B. Rauschenbach, *Quantitative structural and chemical investigation of amorphous and metastable crystalline phase-change alloy thin films by Cs-corrected STEM*, Paper Nr. ISBN 978-80-260-6721-4, IMC 18 Proceedings, Prague, Czech Republic (2014)
4. H. Lu, E. Thelander, J. W. Gerlach, U. Decker, B. Zhu, and B. Rauschenbach, *Single pulse laser-induced phase transitions of PLD-deposited Ge₂Sb₂Te₅ films*, **23**, 3621 (2013).
5. U. Ross, A. Lotnyk, E. Thelander, B. Rauschenbach, *Characterization of laser-deposited Ge-Sb-Te thin films by Cs corrected STEM*, MC 2013 Proceedings (URN number: urn:nbn:de:bvb:355-epub-287343), Regensburg (2013).
6. H. Lu, E. Thelander, J. W. Gerlach, D. Hirsch, U. Decker, and B. Rauschenbach, *Ge₂Sb₂Te₅ phase-change films on polyimide substrates by pulsed laser deposition*, Appl. Phys. Lett. **101**, 031905 (2012).

7. E. Thelander and B. Rauschenbach, *Influence of burst pulses on the film topography in picosecond pulsed laser deposition of LaAlO_3* , J. Physics: Conference Series **356**, 012015 (2012).

Conference contributions (talks):

1. E. Thelander, J.W. Gerlach, B. Rauschenbach, *Pole figure and in-plane measurements on epitaxial $\text{Ge}_2\text{Sb}_2\text{Te}_5$ (GST) thin films*, 3rd European Rigaku SmartLab™ Workshop; Karlsruhe (2014).
2. X. Sun, E. Thelander, H. Lu, J.W. Gerlach, B. Rauschenbach, *Ultraviolet laser-induced phase transitions of PLD-deposited GeTe films*, Annual Conference of the Graduate School BuildMoNa, Leipzig (2014)
3. U. Ross, A. Lotnyk, E. Thelander, B. Rauschenbach, *Atomic resolution investigation of defect structures in textured metastable $\text{Ge}_2\text{Sb}_2\text{Te}_5$ by aberration corrected high resolution STEM*, DPG Spring Meeting, Dresden (2014)
4. U. Ross, A. Lotnyk, E. Thelander, B. Rauschenbach, *Quantitative structural and chemical investigation of amorphous and metastable crystalline phase-change alloy thin films by Cs-corrected STEM*, 18th International Microscopy Congress (IMC 2014), Prague (2014)
5. M. Ehrhardt, P. Lorenz, A. Lotnyk, H. Romanus, E. Thelander, K. Zimmer, *Pattern transfer of sub-micrometre-scaled structures into solid copper by laser embossing*, LANE 2014, 8th International Conference on Photonic Technologies, Fürth (2014)
6. E. Thelander, B. Rauschenbach, *Pulsed laser deposition of LaAlO_3* , Seventeenth International Summer School on Vacuum, Electron, and Ion Technologies, Bulgaria (2011)
7. E. Thelander, B. Rauschenbach, *Picosecond pulse laser deposition of lanthanum aluminate*, 3rd BuildMoNa Workshop, Lutherstadt-Wittenberg (2010)

Conference contributions (posters):

1. E. Thelander, J.W. Gerlach, U. Ross, B. Rauschenbach, *Epitaxial growth of pulsed laser deposited $\text{Ge}_2\text{Sb}_2\text{Te}_5$ thin films*, DPG-spring meeting, Dresden (2014)
2. X. Sun, E. Thelander, H. Lu, J.W. Gerlach, B. Rauschenbach, *Laser-induced phase transitions of PLD-deposited GeTe films*, DPG Spring Meeting, Dresden (2014)
3. E. Thelander, U. Ross, X. Sun, A. Lotnyk, H. Lu and B. Rauschenbach, *Pulsed laser deposition of $\text{Ge}_2\text{Sb}_2\text{Te}_5$ thin films for phase change data storage applications*, Conference on Laser Ablation, Ischia (2013)

4. E. Thelander, H. Lu, U. Ross and B. Rauschenbach, *Phase transitions in GST-films using single nanosecond UV pulses*, DPG Spring Meeting, Regensburg (2013)
5. E. Thelander, H. Lu and B. Rauschenbach *Laser-induced phase transitions in PLD-deposited Ge₂Sb₂Te₅-films*, Annual Conference of the Graduate School BuildMoNa, Leipzig (2013)
6. M. Sarmanova, E. Thelander, A. Jakob, J. W. Gerlach, S.G. Mayr, B. Rauschenbach, *Measurements of elastic properties of surfaces with nanometer resolution*, DPG Spring Meeting, Regensburg (2013)
7. X. Sun, E. Thelander, H. Lu, J. W. Gerlach, U. Decker, D. Hirsch, B. Rauschenbach, *Structural investigation of pulsed laser deposited phase-change films*, 18th International Summer School on Vacuum, Electron and Ion Technologies (VEIT 2013), Sozopol (2013)
8. U. Ross, A. Lotnyk, E. Thelander, B. Rauschenbach, *Quantitative investigation of laser-deposited Ge₂Sb₂Te₅ phase change films by Cs-corrected STEM*, Microscopy Conference MC 2013, Regensburg (2013)
9. U. Ross, A. Lotnyk, E. Thelander, B. Rauschenbach, *Quantitative investigation of laser-deposited Ge₂Sb₂Te₅ by aberration-corrected STEM/EELS*, DPG Spring Meeting, Regensburg (2013)
10. E. Thelander, B. Rauschenbach, *Picosecond pulse laser deposition of lanthanum aluminate*, DPG Spring Meeting, Dresden (2011)
11. E. Thelander, B. Rauschenbach, *Pulsed laser deposition system for synthesis of nanostructures*, 3rd BuildMoNa Symposium, Leipzig (2010)

Selbstständigkeitserklärung

Hiermit versichere ich, dass die vorliegende Arbeit ohne unzulässige Hilfe und ohne Benutzung anderer als der angegebenen Hilfsmittel angefertigt, und dass die aus fremden Quellen direkt oder indirekt übernommenen Gedanken in der Arbeit als solche kenntlich gemacht wurden.

Ich versichere, dass alle Personen, von denen ich bei der Auswahl und Auswertung des Materials sowie bei der Herstellung des Manuskripts Unterstützungsleistungen erhalten habe, in der Danksagung der vorliegenden Arbeit aufgeführt sind.

Ich versichere, dass außer den in der Danksagung genannten, weitere Personen bei der geistigen Herstellung der vorliegenden Arbeit nicht beteiligt waren, und insbesondere von mir oder in meinem Auftrag weder unmittelbar noch mittelbar geldwerte Leistungen für Arbeiten erhalten haben, die im Zusammenhang mit dem Inhalt der vorliegenden Dissertation stehen. Außerdem versichere ich, keinen Promotionsberater in Anspruch genommen zu haben.

Ich versichere weiterhin, dass die vorliegende Arbeit weder im Inland noch im Ausland in gleicher oder in ähnlicher Form einer anderen Prüfungsbehörde zum Zwecke einer Promotion oder eines anderen Prüfungsverfahrens vorgelegt und in ihrer Gesamtheit noch nicht veröffentlicht wurde.

Ich versichere außerdem, dass keine früheren erfolglosen Promotionsversuche stattgefunden haben.

Leipzig, 25. November 2014



Erik Thelander